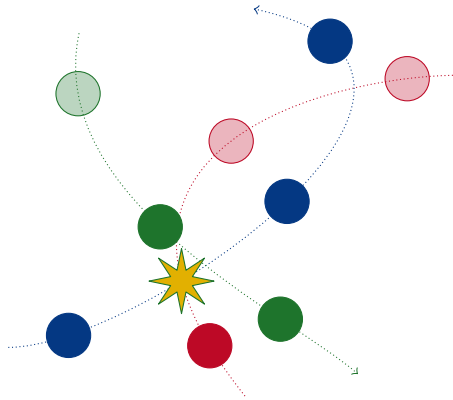# PARTICLE COLLISIONS IN TURBULENT FLOWS

Thèse en vue de l'obtention du grade de
Docteur de l'Université de Lyon
délivré par l'École Normale Supérieure de Lyon

Discipline : Physique

Laboratoire de Physique
École Doctorale de Physique et Astrophysique

Présentée et soutenue publiquement le 13 décembre 2013 par
M. Michel Vosskuhle

Directeur de thèse : M. Alain Pumir
Co-encadrant de thèse : M. Emmanuel Lévêque

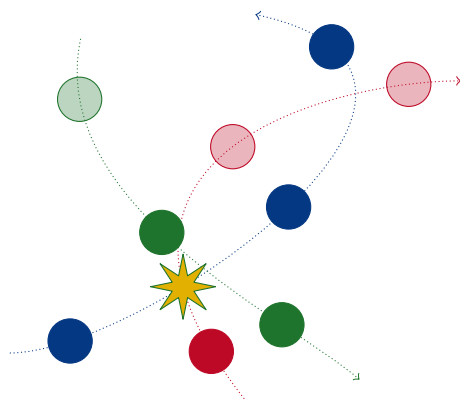Après l'avis de : M. Michel Lance et M. Bernhard Mehlig

Devant la commission d'examen formée de :

M. Jérémie Bec	Observatoire de la Côte d'Azur	(Membre)
M. Michel Lance	École Centrale de Lyon	(Rapporteur)
M. Emmanuel Lévêque	École Centrale de Lyon	(Co-encadrant)
M. Bernhard Mehlig	Göteborgs universitet	(Rapporteur)
M. Alain Pumir	École Normale Supérieure de Lyon	(Directeur)
M. Mike Reeks	Newcastle University	(Membre)
M. Michael Wilkinson	The Open University	(Membre)

MICHEL VOSSKUHLE

PARTICLE COLLISIONS IN TURBULENT FLOWS

PARTICLE COLLISIONS IN TURBULENT FLOWS

Thèse en vue de l'obtention du grade de
Docteur de l'Université de Lyon
délivré par l'École Normale Supérieure de Lyon

Discipline : Physique

Laboratoire de Physique
École Doctorale de Physique et Astrophysique

Présentée et soutenue publiquement le 13 décembre 2013 par
M. Michel Vosskuhle

Directeur de thèse : M. Alain Pumir
Co-encadrant de thèse : M. Emmanuel Lévêque

Après l'avis de : M. Michel Lance et M. Bernhard Mehlig

Devant la commission d'examen formée de :

M. Jérémie Bec	Observatoire de la Côte d'Azur	(Membre)
M. Michel Lance	École Centrale de Lyon	(Rapporteur)
M. Emmanuel Lévêque	École Centrale de Lyon	(Co-encadrant)
M. Bernhard Mehlig	Göteborgs universitet	(Rapporteur)
M. Alain Pumir	École Normale Supérieure de Lyon	(Directeur)
M. Mike Reeks	Newcastle University	(Membre)
M. Michael Wilkinson	The Open University	(Membre)

To my grandma who always
wanted a doctor in
the family.

ABSTRACT

This thesis is devoted to the mechanisms leading to strong collision rates of inertial particles in turbulent suspensions. Our work is based on simulating the motion of particles, using both direct numerical simulations of the Navier–Stokes equations, and a simpler model (kinematic simulations). This subject is important for many applications, in industrial as well as natural (astrophysical, geophysical) contexts. We revisit the ghost collision approximation (GCA), widely used to determine the rate of collisions in numerical simulations, which consists in counting how many times the centers of two particles come within a given distance. Theoretical arguments suggested that this approximation leads to an overestimate of the real collision rate. This work provides not only a quantitative description of this overestimate, but also a detailed understanding of the error made using the GCA. We find that a given particle pair may undergo multiple collisions with a relatively high probability. This is related to the observation that in turbulent flows, particle pairs may stay close for a very long time. We have provided a full quantitative characterization of the time spent together by pairs of particles. A second class of results obtained in this thesis concerns a quantitative understanding of the very strong collision rates often observed. We demonstrate that when the particle inertia is not very small, the "sling/caustics" effect, i.e., the ejection of particles from energetic vortices in the flow, is responsible for the high collision rates. The preferential concentration of particles in some regions of space plays in comparison a weaker role.

KEYWORDS   turbulence, inertial particles, turbulent suspensions, collisions, computational fluid dynamics, multiphase flow

RESUMÉ

Cette thèse est consacrée au mécanisme conduisant à des taux de collisions importants dans les suspensions turbulentes de particules inertielles. Le travail a été effectué en suivant numériquement des particules, par simulations directes des équations de Navier–Stokes, et également par étude de modèles simplifiés. Les applications de ce domaine sont nombreuses aussi bien dans un contexte industriel que naturel (astrophysique, géophysique). L'approximation des collisions fantômes (ACF), souvent utilisée pour déterminer les taux de collision numériquement, consiste à compter dans une simulation, le nombre de fois que la distance entre les centres de deux particules devient plus faible qu'une distance seuil. Plusieurs arguments théoriques suggéreraient que cette approximation conduit à une surestimation du taux de

collision. Cette thèse fournit non seulement une estimation quantitative de cette surestimation, mais également une compréhension détaillée des mécanismes des erreurs faites par l'ACF. Nous trouvons qu'une paire de particules peut subir des collisions répétées avec une grande probabilité. Ceci est relié à l'observation que, dans un écoulement turbulent, certaines paires de particules peuvent rester proches pendant très longtemps. Une deuxième classe de résultats obtenus dans cette thèse a permis une compréhension quantitative des très forts taux de collisions souvent observés. Nous montrons que lorsque l'inertie des particules n'est pas très petite, l'effet « fronde/caustiques », à savoir, l'éjection de particules par des tourbillons intenses, est responsable du taux de collision élevé. En comparaison, la concentration préférentielle de particules dans certaines régions de l'espace joue un rôle mineur.

MOTS-CLEFS   turbulence, particules inertielles, suspensions turbulentes, collisions, simulations numériques d'écoulements turbulents, écoulements multi-phasiques

PUBLICATIONS

Some of the ideas and figures presented in this thesis have been published before in the following papers:

Voßkuhle M, Pumir A, Lévêque E (2011). "Estimating the Collision Rate of Inertial Particles in a Turbulent Flow: Limitations of the 'Ghost Collision' Approximation." In: *J. Phys.: Conf. Ser.* 318, p. 052024. DOI: 10.1088/1742-6596/318/5/052024.

Voßkuhle M, Pumir A, Lévêque E, Wilkinson M (2013b). "Prevalence of the sling effect for enhancing collision rates in turbulent suspensions." In: *ArXiv e-prints* (July 2013). arXiv: 1307.6853 [physics.flu-dyn].

Voßkuhle M, Lévêque E, Wilkinson M, Pumir A (2013a). "Multiple collisions in turbulent flows." In: *ArXiv e-prints* (Oct. 2013). Accepted for publication in Phys. Rev. E. arXiv: 1310.1521 [physics.flu-dyn].

*The Stone Age did not come to an end
because we had a lack of stones […]*

Ahmed Zaki Yamani (أحمد زكي يماني)
Saudi Arabian Minister of Oil 1962–1986

ACKNOWLEDGMENTS

I thank my supervisor Alain Pumir.

I thank my co-supervisor Emmanuel Lévêque and our collaborator Michael Wilkinson.

I thank the committee members Jérémie Bec, Michel Lance, Bernhard Mehlig, and Mike Reeks.

I thank the Centre Blaise Pascal, the Pôle Scientifique de Modélisation Numérique, and the physics lab at the ENS Lyon.

I thank all developers of FLOSS.

I thank all colleagues from the ENS.

I thank all former colleagues and mentors.

I thank all friends I have made in Lyon.

I thank my parents, family, friends and everyone who supported me.

I thank Wubi $x = \left(\sin(t)\cos(t)\ln|t|, \sqrt{|t|}\cos(t) \right)$, $|t| \geq 1$.

CONTENTS

ACRONYMS

DNS   Direct numerical simulation

GCA   Ghost collision approximation (Section 3.2.6)

GIP   Generalized inverse property (Appendix B)

KS   Kinematic simulation (Chapter 8)

PDF   Probability density function

R1   Replacement approach replacing one particle
            (Section 6.5.1)

R2   Replacement approach replacing both particles
            (Section 6.5.1)

RDF   Radial distribution function (Section 3.2.4)

RNG   Random number generator

RRV   Radial relative velocity (Section 3.2.4)

NOTATION

It has been attempted to keep the meaning of symbols consistent throughout the whole document. Here is a list of the most important definitions used in this text.

a particle radius

$\mathbf{A}, A_{ij}$ velocity gradient tensor

$\mathbf{B}, B_{ij}$ matrix defined in Equation (B.3)

c_g parameter in Equation (5.2)

c_w fit parameter similar to c_g but for $\langle |w_r| \rangle$

C constant

Co   Courant number, Section 5.1

d dimensionality

$\mathcal{D}_2$ correlation dimension, Section 5.3.1

$E(k, t)$ energy spectrum

$\mathcal{E}_c$ collision efficiency, Section 3.2.7

$f(a)$ droplet size distribution, Section 3.1.1

F	cumulative probability density function
$g(\boldsymbol{r})$	radial distribution function, Equation (3.11)
$\boldsymbol{G}$	gravitation vector
$h_{\mathrm{S}}(\mathrm{St}, \mathrm{Re}_\lambda)$	rate of caustic formation, Section 3.2.5
$J(a)$	term representing growth due to condensation in Equation (3.1)
k	wavenumber
L	integral length scale
n	number density (of particles)
N	number of *subscript*
$\mathcal{N}_c$	overall rate of collision
p	probability density function (PDF)
P	probability or probability density function (PDF)
$\mathcal{P}$	pressure field divided by fluid density ρ, Section 2.1
$\boldsymbol{Q}$	forcing field in the Navier–Stokes equation (2.2)
$\boldsymbol{r}$	distance vector
R_{ij}	velocity autocorrelation function, Equation (2.5)
$\hat{R}_{ij}$	Fourier transform of the velocity autocorrelation tensor R_{ij}
$\mathcal{R}$	rate of collision encountered by one particle
Re	Reynolds number
$S(k, t)$	transfer of energy into mode k, Section 2.2.3
St	Stokes number, Equation (2.19)
t	time
T_L	integral time scale
$\boldsymbol{u}$	fluid velocity field
$\boldsymbol{V}$	particle velocity vector
$\mathcal{V}$	volume
$\boldsymbol{w}$	relative velocity between two particles
$\boldsymbol{x}$	coordinate, typically as argument in a field
$\boldsymbol{X}$	particle position vector

Greek letters

α	fit coefficient in Equation (6.2)
β	fit coefficient in Equation (6.2)
$\gamma(\mathrm{St}, \mathrm{Re}_\lambda)$	factor relating V_{rms} and u_K, Section 3.2.3

Γ	collision kernel, Section 3.1.2
$\delta(\cdot)$	Dirac delta function
Δt	time-step in numerical simulations
ε	energy dissipation rate per unit mass, Equation (2.11)
ζ	dimensionless quantity in Equation (4.10)
η	Kolmogorov length, Section 2.2.4
θ	polar angle in a spherical coordinate system
$\Theta(\cdot)$	Heaviside step function
κ	fit coefficient in Section 4.3.2
λ	Taylor scale, Equation (2.7)
μ	dynamic viscosity
ν	kinematic viscosity
ξ	fit coefficient in Section 4.3.2
$\varpi^{(2)}$	distribution function, Equation (3.10)
$\Pi(k, t)$	energy flux, Section 2.2.3
ρ	mass density
$\boldsymbol{\sigma}$, σ_{ij}	particle velocity gradient tensor, Section 2.3.2
ς	$\varsigma = V_{\mathrm{rms}}$ in Chapter 4
τ	characteristic time
ϕ	azimuthal angle in a spherical coordinate system
$\varphi(\lvert w_r \rvert)$	Ratio of the flux into the collision sphere with RRV smaller than $\lvert w_r \rvert$, Equation (7.4)
Φ	volume fraction
χ	indicator function in Equation (3.16)
ψ	collision operator, see p. 27
$\boldsymbol{\omega}$	vorticity, Equation (2.3)
Ω	surface of a sphere

Subscripts

$\odot$	concerning a spherical shell
$2a$	having separation $2a$
A	Abrahamson (1975)
b	boxes in cell linked-list algorithm, Section 4.1.1
c	collision
cor	correlation
e	encounter

f	fluid
GCA	ghost collision approximation
ig	ideal gas
K	Kolmogorov scale, Section 2.2.4
l	longitudinal
L	integral scale
λ	based on the Taylor scale
m	multiple (collisions)
max	maximal
min	minimal
p	particle
r	radial
R	associated with the replacement algorithm, Section 6.5.1
rms	root mean square
s	separation
S	sling/caustics, Section 3.2.5
SC	Sundaram & Collins (1997)
ST	Saffman & Turner (1956)
t	transverse

Part I

REVIEW OF FUNDAMENTAL RESULTS

INTRODUCTION

Among the unsolved problems in physics, turbulence is probably the one that affects our daily life the most. The search for the ultimate components of matter, or for the structure of the universe leads to fundamental questions. However, our lack of understanding about dark matter or dark energy comes in large part from the scarcity of experimental information, which ultimately originates from the fact that they are relevant at scales which are very remote from our everyday life. This situation makes the success of the standard model even more impressive—despite the fact that it may still be improved, or that it does not include a theory of gravitation. In comparison, turbulence is encountered in everyday life, yet, we do not have a fully satisfactory theory to describe this important phenomenon.

If we ride our bicycle or Vélo'v along the Rhône, we know how difficult it is to gain that extra 5 km/h, that would allow us to be in time. The reason is the air, which we bring into motion by moving through it—just like the car in Figure 1.1. Simple dimensional arguments allow us to understand, why it is so hard to be faster. Riding our bike at speed v and for a time t, we leave behind us a wake of air in motion of volume Avt, where A is roughly the cross-sectional area of us facing the direction we are heading to. To estimate the energy contained in this corridor we need to estimate its mass, which is simply $Avt\rho$, where ρ is the density of air. This mass is moving at speed v and therefore contains the energy $\frac{1}{2}Avt\rho v^2$. This means the energy we loose just to agitate the gas surrounding us grows with v^3. Going at 25 km/h instead of 20 km/h is two times harder. Furthermore the linear prefactor A explains, why we intuitively duck down, when we try to ride faster or when we are facing a headwind. Every bit by which we diminish the surface A, results directly in less energy that we need to disperse for agitating air.

The Vélo'v is a rental bike in Lyon.

See MacKay (2009) for similar estimates.

FIGURE 1.1

Photograph of a Citroën DS in a wind tunnel. One can clearly see the agitated flow behind the car. © ONERA (2009)

Looking closely at the wake behind the car in Figure 1.1, one notices that the motion of the air is not structureless. While the motion seems chaotic and unpredictable on the one hand, one can on the other hand clearly discern structures on many length scales. This is one of the intriguing features of turbulence. A detailed analysis shows that the above estimate for the energy contained in the wake is too simple. In fact the surface A needs to be replaced by a sort of effective surface described by the so-called drag coefficient. This drag coefficient depends on the geometry of the object that moves through the fluid. Tiny changes in the design of vehicles may easily lead to changes in efficiency of the order of 10 %. Therefore car producers a very interested in the drag coefficient of new models they develop. Understanding the turbulence in the wake is crucial in estimating the drag coefficient without costly wind tunnel experiments.

That review has been reprinted in von Neumann (1961).

The above is just one example where a complete and fully predictive theory of turbulence is missing. There are many other domains including weather prediction or various industrial processes, which would benefit from such a theory. But still this phenomenon evades a conclusive description. In a 1949 review on turbulence John von Neumann expressed "hope to 'break the deadlock' by extensive, but well-planned, computational efforts." His wish has been fulfilled in the sense that nowadays extensive numerical simulations provide deep insights into the phenomenon of turbulence. But the hope that these computations might help answer the "calling for a new form of statistical mechanics" has not materialized yet.

The Millenium Simulation investigates the evolution of the matter distribution in the Universe.

The most precise simulation of a turbulent flow up to now used 4096^3 spatial discretization points in a periodic box (Ishihara et al. 2007; Kaneda et al. 2003 and later also Bitane et al. 2012; Hackl et al. 2011). The codes are based on pseudo-spectral methods and effectively simulate the evolution equation of approximately 7×10^{10} Fourier modes. As a comparison, the well-known Millennium Simulation (Springel 2005; Springel et al. 2005) considered interactions between "only" 1×10^{10} particles. And still, the simulation of Kaneda et al. (2003) achieves a flow at a Reynolds number[1] $\mathrm{Re}_\lambda = 1200$ which is relatively small in comparison to Reynolds numbers observed in many natural phenomena (e.g., $\mathrm{Re}_\lambda = 10^4$ in a typical cloud, Siebert et al. 2010). The reason why it is so hard to perform simulations of turbulent flows at large Reynolds numbers are again the structures, which are present on a wide range of length scales. An exact simulation must resolve all these length scales which may span over several decades.

The present study is in a sense in the tradition of the above cited works. Here also numerical simulations are performed to study turbulent flows. But instead of seeking insights into the fundamental structure of turbulence, this work concentrates on the phenomena that arise when particles are entrained by turbulent flows.

---

[1] The Reynolds number, roughly speaking, determines the intensity of turbulence. Refer to Section 2.1.2 and Equation (2.8) for details.

1.1 PARTICLES IN TURBULENCE AND COLLISIONS

In nature, more often than not, fluids do transport material in another state of matter (Balachandar & Eaton 2010). One may think of aerosol particles in the atmosphere, plankton in the sea, or pollutants in riverbeds. Evidently, whether the fluid is turbulent or not has a big impact on the particulate phase. Stirring in the ocean enhances the mixing of phytoplankton and fertilizers (Abraham et al. 2000). Also, animals, that rely on olfactory perception, may need to adapt their strategies in a turbulent environment (Ferner & Weissburg 2005; Mafra-Neto & Carde 1994).

As long as the entrained objects are small enough, they follow the movements of the flow exactly. For larger particles however, with a different density than the fluid, new phenomena emerge. Clustering of particles in certain regions of the flow is a well-known example.

In this work we focus in particular on collisions between the entrained objects. The collisions occurring between particles are important in a wide range of applications. Many industrial production processes, like manufacturing of titania (Moody & Collins 2003), rely on turbulent mixing to bring the base products into contact. In all kinds of sprays, the coalescence rate of the droplets has an impact on their size distribution. This is of importance for example in diesel engines (Post & Abraham 2002). There, further aspects, like the evaporation of droplets, provide motivation for interesting research (Chareyron et al. 2012).

Also in nature formation of larger particles by collision is very frequent. Wells & Goldberg (1991) find, that there is an abundance of colloidal particles in sea water. For instance a significant part of the carbon, that is considered dissolved in the oceans, "may in fact be present in the form of colloid particles" (Stumm & Morgan 1996, p. 818)[2]. Another example for the importance of collisions in the dispersed phase of a fluid is provided by sandstorms, whose intensity can be enhanced by colliding grains (Carneiro et al. 2013). Even animate matter depends on turbulence induced collisions as can be seen in the works of Lewis & Pedley (2000) and Rothschild & Osborn (1988).

Our main motivation (discussed in Chapter 3) is provided by two further domains. On the one hand, collisions between droplets in clouds, contribute to their growth process and therefore influence the onset of rain (Shaw 2003). They also affect the size distribution of drops, which has a strong influence on the reflection of light from the sun, and thus, on the energy budget of the earth and on the climate. On the other hand we refer to collisions of dust grains in protoplanetary disks that play a crucial role in the formation of planets (Safranov 1972). The contribution of turbulence to the collision rates has been the subject of many studies, in relation to the two problems referred to here. The aim of this work is to provide further quantitative understanding of the problem.

---

2 See also the review by Kepkay (2000).

1.2   OUTLINE

This work is organized in three parts. The first part includes this introduction as well as two chapters on fundamental concepts. Chapter 2 introduces the basic equations and some of the typical reasoning that will be used throughout the text. The following chapter provides a short review of cloud physics in Section 3.1. In Section 3.2 different aspects of collision rates of particles suspended in turbulent flows are discussed. This section constitutes the basics which are important to understand our scientific work presented in the second part.

We split our own results in five chapters. The first two, Chapters 4 and 5, describe different aspects of our numerical simulations. Furthermore, we validate our code, by comparing its results to published data and theoretical predictions. Additionally we present some simple results which we obtained theoretically for ideal gas-like particles in Sections 4.2 and 4.3.

Especially the findings from Section 4.3 will be helpful in interpreting some of the results presented in Chapter 6. There we investigate multiple collisions between a same pair of particles, which astonishingly may take place in a turbulent flow (Section 6.2). These multiple collisions are related to the ghost collision approximation (GCA) in Section 6.1. That approximation is often made in numerical simulations but is also apparent in theoretical results. Inspired by the observation of multiple collisions we proceed to investigate the time that particles stay in contact in Section 6.3. Before discussing an alternative to the GCA in Section 6.5, we present an interpretation of our results in the light of sling/caustics collisions in Section 6.4. Section 6.6 concludes that chapter.

In Chapter 7 we come back to the sling/caustics effect. A subtle post-processing of our numerical data allows us to conclude on the prevalence of the sling/caustics effect over simple shear induced collisions. These results are presented in Section 7.1 and confirmed by additional investigations in Section 7.2. The analysis performed in this work is in fact fully consistent with evidence that was already present in previous numerical results, or anticipated theoretically using simplified models, as we explain in Section 7.3.

All our results presented until Chapter 8 were obtained in direct numerical simulations (DNS). But we started our investigations using a simple model flow known as kinematic simulations (KS). In Chapter 8 we discuss how the lower computational cost of this model allows some further investigations which would be prohibitive in DNS. The qualitative results in KS are the same as presented before for DNS. But quantitatively we find large differences which are shortly discussed in that chapter.

Finally, in the Appendices, we will present two more technical aspects of our work. Some of the approaches developed for our investigations and discussed in Appendices A and B, may be interesting for future work.

FUNDAMENTAL RESULTS

After an introduction of the subject from a broader perspective, and a general presentation of the reasons why it is worthwhile to understand the behavior of particles in turbulent flows, we now discuss the relevant results our work relies on. This presentation does not have the ambition to be exhaustive. Details not covered here can be found in the literature cited in the text. Expert readers may skip this chapter and only get back to it, when it is referenced later on in the text.

2.1 NAVIER–STOKES EQUATIONS[1]

To derive the basic equations governing the motion of a fluid, one starts from two balance equations. The first one describes mass conservation in terms of the density field $\rho(\boldsymbol{x}, t)$, and the other one conservation of momentum, in terms of $\rho(\boldsymbol{x}, t)\boldsymbol{u}(\boldsymbol{x}, t)$, where $\boldsymbol{u}(\boldsymbol{x}, t)$ is the fluid velocity at position $\boldsymbol{x}$ and time t. For an incompressible fluid, the density is independent of time and position and the continuity equation derived from mass conservation simplifies to

$$\nabla \cdot \boldsymbol{u}(\boldsymbol{x}, t) = 0. \tag{2.1}$$

The equation for the momentum has to accurately account for all forces acting on the fluid's surface or volume. In case of incompressible Newtonian fluids, one obtains

$$\frac{\partial}{\partial t}\boldsymbol{u}(\boldsymbol{x}, t) + \boldsymbol{u}(\boldsymbol{x}, t) \cdot \nabla\boldsymbol{u}(\boldsymbol{x}, t) = -\nabla\mathcal{P}(\boldsymbol{x}, t) + \nu\Delta\boldsymbol{u}(\boldsymbol{x}, t) + \boldsymbol{Q}(\boldsymbol{x}, t), \tag{2.2}$$

where the momentum equation has been divided by the constant fluid density ρ. Therefore $\mathcal{P}(\boldsymbol{x}, t)$ is the pressure divided by the density, but usually referred to as just "pressure". The kinematic viscosity $\nu = \mu/\rho$ is the quotient of dynamic viscosity and density, and finally $\boldsymbol{Q}(\boldsymbol{x}, t)$ contains all different external forces like gravitation or the Coriolis force. Equation (2.2) has first been derived by Navier (1823) and Stokes (1843) and hence is known as the Navier–Stokes equation.[2]

Even ignoring external forces, Equation (2.2) may seem to be unclosed at first sight, because the pressure $\mathcal{P}(\boldsymbol{x}, t)$ appears in it. But actually the pressure is fully determined by Equations (2.1) and (2.2) as can be seen when one calculates the divergence of the Navier–Stokes equation. In case of divergence free forces $\boldsymbol{Q}(\boldsymbol{x}, t)$ this yields the Poisson equation

$$\Delta\mathcal{P}(\boldsymbol{x}, t) = -\nabla \cdot \left[\left(\boldsymbol{u}(\boldsymbol{x}, t) \cdot \nabla \right) \boldsymbol{u}(\boldsymbol{x}, t) \right],$$

---

1 This section and parts of the next one loosely follow a former work, originally written in German (Voßkuhle 2009).

2 Or more precisely, as they are actually three differential equations for each component of $\boldsymbol{u}(\boldsymbol{x}, t)$ and need to be combined with Equation (2.1): the Navier–Stokes equations.

which can be solved with the help of Green's function for the Laplacian (see Friedrich 2007) or by inversion of the Laplacian in Fourier space (see Frisch 1996).

Furthermore the solution of Equations (2.1) and (2.2) requires the determination of initial and boundary conditions. In realistic problems the boundary conditions are usually given by impermeability and no-slip walls. In many computer simulations however, it is convenient to impose periodic boundary conditions in a cube. This method will also be employed throughout this work.

2.1.1 *The vorticity*

For the sake of completeness, we introduce the vorticity $\boldsymbol{\omega}(\boldsymbol{x}, t)$ which is simply the rotation of the velocity field

$$\boldsymbol{\omega}(\boldsymbol{x}, t) = \nabla \times \boldsymbol{u}(\boldsymbol{x}, t). \tag{2.3}$$

In the case of a solid body motion, this definition of $\omega(\boldsymbol{x}, t)$ is, within a factor of 2, the definition of the rate of rotation. The equation describing the evolution of the vorticity $\omega(\boldsymbol{x}, t)$ is deduced from Equation (2.2) by applying the rotation operator.

A description of turbulent fluids in terms of "eddies", or vortices, with a wide distribution of scales has emerged over the years, starting with the famous illustrations of Leonardo da Vinci (see Figure 2.1). In fact, the vorticity field is as fundamental as the velocity field, as the latter can be obtained from the former by simply inverting Poisson's equations. Moffatt (1981) and Saffman (1992) review essential results in this field.

2.1.2 *Self similarity and the Reynolds number*

An adimensional form of the Navier–Stokes equation can be handily derived by introducing the dimensionless units (see, e.g., Argyris et al. 2010)

$$\tilde{\boldsymbol{u}} = \frac{\boldsymbol{u}}{U}, \qquad \tilde{t} = \frac{t}{T}, \qquad \tilde{\boldsymbol{x}} = \frac{\boldsymbol{x}}{L}, \qquad \tilde{p} = p\frac{L}{U^2}, \qquad \tilde{\boldsymbol{Q}} = \boldsymbol{Q}\frac{T}{U^2},$$

with some characteristic length, time, and velocity scales L, T, and $U = L/T$. Inserting in Equation (2.2) and immediately dropping the tildas, one obtains

$$\frac{\partial}{\partial t}\boldsymbol{u}(\boldsymbol{x}, t) + \boldsymbol{u}(\boldsymbol{x}, t)\cdot\nabla\boldsymbol{u}(\boldsymbol{x}, t) = -\nabla\mathcal{P}(\boldsymbol{x}, t) + \frac{1}{\text{Re}}\Delta\boldsymbol{u}(\boldsymbol{x}, t) + \boldsymbol{Q}(\boldsymbol{x}, t), \tag{2.4}$$

where we introduced the dimensionless Reynolds number Re $= UL/\nu$. It is named after Osborne Reynolds (1883), who noticed in experiments on pipe flows, that whether the flow is turbulent or laminar depends only on the quantity Re. Indeed, Equation (2.4) demonstrates, that flows with the same Reynolds number behave similarly. This allows engineers to test new developments on model vehicles with reduced size in wind tunnels.

2.2 TURBULENCE

The observation Reynolds (1883) made in his experiments was the following. He was pumping a given fluid, at a fixed viscosity v, through a cylindrical tube of diameter L. By increasing the pumping velocity, hence U, he could increase the value of Re. At low values of Re, the fluid motion is observed to be laminar. Tiny tracer particles would along straight lines. Above a critical value of Re, however, Reynolds observed that the tracer trajectories were no longer straight. The fluid would move in an irregular and unpredictable way. This state of fluid motion is known as turbulence. Its emergence may become more evident, when one interprets the Reynolds number as the ratio between the nonlinear convection term $u(x, t) \cdot \nabla u(x, t)$ and the dissipation term of the Navier–Stokes equations. When the smoothing action of dissipation is outdone by convection, the flow becomes turbulent.

We explained in the introduction (Chapter 1) why it is of such an importance to gain a deeper understanding of turbulence. And it was also discussed, that a satisfactory theory of the phenomenon has not yet been proposed. Nevertheless, during its long history, research in turbulence has produced many important results. Nowadays there is a vast number of textbooks on it, from the classic ones by Batchelor (1959) or Tennekes & Lumley (1972) to more modern ones like those from Frisch (1996) or Pope (2000). Each of these books focuses on some specific aspects of the problem. Here we will only discuss some of the most basic notions, that can be found in almost all textbooks. The typical reasoning we introduce in the coming paragraphs will reappear throughout the text.

2.2.1   *The cascade picture*

The observation that turbulent flows involve many length scales is already obvious in some of Leonardo da Vinci's writings and drawings. Figure 2.1 shows clearly how the large scale structures at which the turbulence is generated –in this case water flowing in a basin– evolve to produce structures on many length scales. A phenomenological explanation of this fact is attributed to Richardson (1922), who in his famous adaption of a poem by Jonathan Swift, explains his view

> *We realize thus that: big whirls have little whirls that feed on their velocity, and little whirls have lesser whirls and so on to viscosity—in the molecular sense.*

What he means is that turbulence receives its energy from large scale vortices (or coherent structures) generated by some external forcing. These vortices will then break up into smaller vortices, who themselves get unstable and break up. The energy gets, in this way, transported to ever smaller scales until it reaches the smallest scales where viscosity acts and transforms it into heat.

The above described picture is known as the Richardson cascade; Figure 2.2 shows a typical illustration. We shall call the length scale at which the
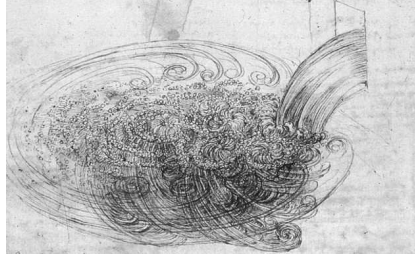
FIGURE 2.1

Detail of "Studies of Water passing Obstacles and falling", drawings by Leonardo da Vinci (c. 1508–1509). Coherent structures of different sizes are well brought out.
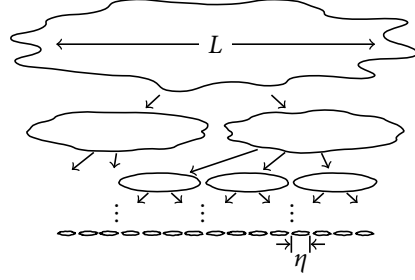

FIGURE 2.2

Typical illustration of the Richardson cascade. External forcing generates turbulence at length scale L. The large scale vortices of this size break up to give ever smaller vortices. Finally, at length scale η, the energy gets dissipated by viscosity.

turbulence is generated L and the one, where the energy gets dissipated by viscosity η. The coming sections will show, how these heuristically defined scales can get quantified.

2.2.2 *Homogenous and isotropic turbulence*

It became clear quite early, that the assumption of turbulence being statistically homogenous and isotropic leads to significant simplifications. Already William Thomson (1887), the later Lord Kelvin, supposed that the velocity field of a turbulent fluid was homogenous and posed the question, in what situation the assumption of isotropy would be justifiable. Subsequent experimental studies supported the validity of both assumptions. Here we follow later work by Taylor (1935) to clarify the concept. An interesting account of the development of the scientific ideas leading to our present knowledge can be found in a recent review of the correspondence between Prandtl and Taylor (Bodenschatz & Eckert 2011). We start by introducing the spatial velocity autocorrelation function

$$R_{ij}(\boldsymbol{r}, \boldsymbol{x}, t) = \left\langle u_i(\boldsymbol{x} + \boldsymbol{r}, t) u_j(\boldsymbol{x}, y) \right\rangle. \tag{2.5}$$

Here, as well as later in the text, the angular brackets $\langle \cdot \rangle$ denote a suitably defined average. The velocity correlation function is a very interesting quantity; it is relatively easy to measure in experiments and numerical simulations, and also convenient to analyze from a mathematical point of view. Metaphorically speaking, it tells how much the velocity at point $\boldsymbol{x}$ is influenced by the velocity at position $\boldsymbol{x} + \boldsymbol{r}$.

If we assume *homogeneity*, all points in space become statistically equivalent and the velocity correlation function does not depend on $\boldsymbol{x}$ any more.
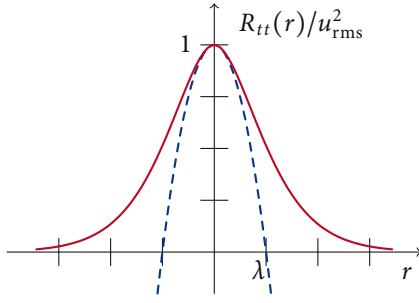
FIGURE 2.3

A parabola, corresponding to the second term in a Taylor expansion of the transverse velocity autocorrelation function, intersects the axis at the Taylor length λ, Equation (2.7).

For *stationary* statistics, the correlation function does not depend on time. Finally, if the statistics are assumed to be *isotropic*[3], the second order tensor $R_{ij}(\boldsymbol{r})$ can only take a certain form (see, e.g., Robertson 1940)

$$R_{ij}(\boldsymbol{r}) = R_{tt}(rr)\delta_{ij} + \left[R_{ll}(r) - R_{tt}(r)\right]\frac{r_i r_j}{r^2} \tag{2.6}$$

This is discussed in more detail by, e.g., Batchelor (1953) and Landau & Lifshitz (1987). $R_{ll}(r)$ and $R_{tt}(r)$ are respectively the longitudinal and transverse autocorrelation functions. Taylor (1935) used them to define two distinct length scales. Both may be defined for the longitudinal as well as for the transverse correlation, but we limit ourselves to the latter.

First, we define a short length scale. To this end $R_{tt}(r)$ is developed into a series. The first term of this series, $R'_{tt}(0)$, vanishes due to incompressibility, Equation (2.1). The second term can be evaluated, $R''_{tt}(0) = \langle(\partial u_1/\partial x_2)^2\rangle$ (Pope 2000), and used to define the length scale[4]

$$\lambda^2 = \frac{2u_{\text{rms}}^2}{\left\langle\left(\frac{\partial u_1}{\partial x_2}\right)\right\rangle}. \tag{2.7}$$

A geometrical interpretation of λ can be found in Figure 2.3. Taylor (1935) interpreted λ as the length scale of the smallest eddies. This is not correct, actually λ is intermediate between the smallest and largest turbulent length scales, η and L respectively (see, e.g., Pope 2000, for details). Despite this fact, λ is widely used and its simple but exact definition is appreciated. The correspondingly defined Taylor scale Reynolds number

$$\text{Re}_\lambda = \frac{u_{\text{rms}}\lambda}{\nu} \tag{2.8}$$

is one of two quasi-standard forms to give the Reynolds number in DNS and in experiments.

Next, we introduce the integral length scale L_t. The index t does not only indicate that it is based on the transverse velocity autocorrelation function, but also differentiates it from the conceptual integral length scale L, that has

---

3 That means invariant under rotation and usually also reflexion.
4 The variable u_{rms} denotes the root mean square velocity *of one component*, i.e., $u_{\text{rms}} = \langle\boldsymbol{u}(\boldsymbol{x},t)\cdot\boldsymbol{u}(\boldsymbol{x},t)/3\rangle^{1/2}$.

been introduced before. It is a large length scale given by the surface under the autocorrelation function

$$L_t = \frac{1}{u_{\text{rms}}^2} \int_0^\infty R_{tt}(r)\,\mathrm{d}r. \tag{2.9}$$

The velocity field decorrelates at L_t, which therefore characterizes the length scale of the largest eddies.

As mentioned before, corresponding length scales can be derived from the longitudinal velocity correlation function $R_{ll}(r)$. It can be shown that those are not independent from λ and L_t respectively. Indeed, exact relations can be derived as shown, e.g., in the textbook by Pope (2000).

2.2.3   *Energy flux and energy dissipation rate*

Before coming to the famous phenomenology of Kolmogorov, we need to introduce one more quantity characterizing the cascade process—the energy dissipation rate ε.

An equation describing the temporal evolution of the average energy per unit mass, $\langle u^2/2 \rangle$, can easily be derived from the Navier–Stokes equation. To this end, one multiplies Equation (2.2) by $\boldsymbol{u}(\boldsymbol{x}, t)/2$ and then averages the complete equation. By standard techniques, taking into account incompressibility, Equation (2.1), and especially the boundary conditions, one obtains

$$\frac{\mathrm{d}}{\mathrm{d}t}\frac{\langle u(\boldsymbol{x}, t)^2 \rangle}{2} = v\langle \boldsymbol{u}(\boldsymbol{x}, t) \cdot \Delta \boldsymbol{u}(\boldsymbol{x}, t) \rangle + \langle \boldsymbol{u}(\boldsymbol{x}, t) \cdot \boldsymbol{Q}(\boldsymbol{x}, t) \rangle. \tag{2.10}$$

Frisch (1996, p. 19) explains the derivation for periodic boundary conditions, McComb (1992, p. 524) does the calculation in an arbitrary volume with vanishing velocity at the boundaries. In the stationary case the left-hand side of Equation (2.10) is zero and obviously energy production by the external forces and energy dissipation by viscosity balance. We may therefore define the *energy dissipation rate per unit mass*[5]

$$\varepsilon = -v\langle \boldsymbol{u}(\boldsymbol{x}, t) \cdot \Delta \boldsymbol{u}(\boldsymbol{x}, t) \rangle = \frac{1}{2}v \sum_{i,j} \left\langle \left(\partial_i u_j + \partial_j u_i \right)^2 \right\rangle = v\langle |\boldsymbol{\omega}|^2 \rangle, \tag{2.11}$$

where the latter two equalities can be derived by similar techniques as before and $\boldsymbol{\omega}(\boldsymbol{x}, t)$ is the vorticity as defined in Equation (2.3).

It is interesting to remark, that the nonlinear and nonlocal terms of the Navier–Stokes equation do not contribute to the energy budget in Equation (2.10). Although they neither produce, nor dissipate energy, they do contribute to the transport of energy between scales. This becomes clear when one considers the energy balance in Fourier space. Namely, one observes that

$$\frac{1}{2}\langle u_i(\boldsymbol{x}, t) u_i(\boldsymbol{x}, t) \rangle = \frac{1}{2} \iiint_{-\infty}^{\infty} \hat{R}_{ii}(\boldsymbol{k}, t)\,\mathrm{d}\boldsymbol{k} = \int_0^\infty E(k, t)\,\mathrm{d}k,$$

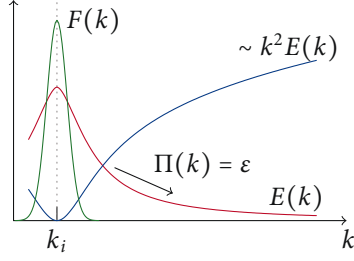[5] We introduce the notation $\partial_i := \partial/\partial x_i$ for spatial derivatives.

FIGURE 2.4

where Einstein summation applies to repeated indices in the first two terms. $\hat{R}_{ij}(\boldsymbol{k}, t)$ is the Fourier transform of the velocity autocorrelation tensor $R_{ij}(\boldsymbol{r}, t)$, defined in Equation (2.6), with respect to $\boldsymbol{r}$. The energy spectrum $E(k, t)$ is a definition that follows by simply integrating over the angular components (see, e.g., Tennekes & Lumley 1972). It can be interpreted as giving the energy contained in each scale k.

An evolution equation for $E(k)$ can be obtained from the Navier–Stokes equation in Fourier space (see, e.g., Orszag 1977), or directly by Fourier transformation of the evolution equation for the velocity correlation tensor $R_{ij}(\boldsymbol{r}, t)$

$$\left(\frac{\partial}{\partial t} + 2\nu k^2\right) E(k, t) = S(k, t) + F(k, t). \tag{2.12}$$

Here $S(k, t)$ arises from the convection term in Equation (2.2), $F(k, t)$ corresponds to the external forcing, and contributions from the pressure term vanish identically. It has been mentioned before, that the nonlinear term does neither produce, nor dissipate energy. When Equation (2.12) is integrated, it should give the Fourier transform of Equation (2.10). This implies that the integral of $S(k, t)$ over k has to vanish

$$\int_0^\infty S(k, t) \, \mathrm{d}k = 0. \tag{2.13}$$

$S(k, t)$ can be interpreted as the transfer of energy into mode k.

We shall now follow Lesieur (1997) in a simple but revealing reasoning, that will finally put Richardson's interpretation on a theoretical basis. To this end we consider a stationary flow, i.e., we drop all the t-dependencies in Equation (2.12) and we define the energy flux

$$\Pi(k, t) = \int_k^\infty S(k') \, \mathrm{d}k' = -\int_0^k S(k') \, \mathrm{d}k',$$

where the second equality follows simply from Equation (2.13). The energy flux is the amount of energy flowing through the Fourier mode k. If it is positive, $\Pi(k) > 0$, energy flows towards larger wavenumbers and vice versa.

Now consider the following situation corresponding to Richardson's picture (comp. Figure 2.4). The external forcing is pumping energy into the system at a small wavelength k_i. As we are in a stationary situation, the

energy injection rate necessarily equals the energy dissipation rate and we have

$$\varepsilon = \int_0^\infty F(k)\,\mathrm{d}k.$$

Then the balance equation for $\Pi(k)$, obtained by integrating Equation (2.10)

$$\Pi(k) = \int_0^k F(k')\,\mathrm{d}k' - 2\nu \int_0^k k'^2 E(k')\,\mathrm{d}k',$$

may be investigated for two distinct regions. In the range $k < k_i$, the integral over the external forcing is zero and in the limiting case of infinite Reynolds number, i.e., $\nu \to 0$, we obtain

$$\lim_{\nu\to 0}\Pi(k) = -2\lim_{\nu\to 0}\nu\int_0^{k<k_i} k'^2 E(k')\,\mathrm{d}k' = 0.$$

For $k > k_i$ the integral over the forcing becomes equal to ε and for some finite $k_i < k \ll \infty$, one has

$$\lim_{\nu\to 0}\Pi(k) = \varepsilon - 2\lim_{\nu\to 0}\nu\int_0^{k_i<k\ll\infty} k'^2 E(k')\,\mathrm{d}k' = \varepsilon.$$

If however we admit $k \to \infty$, the integral in above equation must vanish in order to secure the validity of Equation (2.10), even when the viscosity ν tends towards zero, i.e.,

$$2\lim_{\nu\to 0}\nu\int_0^{k\to\infty} k'^2 E(k')\,\mathrm{d}k' = \varepsilon.$$

Summing up, we have for the energy flux in the three discussed regions in the limit of vanishing viscosity

$$\lim_{\nu\to 0}\Pi(k) = \begin{cases} 0, & k < k_i \\ \varepsilon, & k_i < k \ll \infty \\ 0, & k \to \infty \end{cases}$$

Therefore the energy, generated at large length scales (i.e., small wavenumbers), does flow towards the small scales, just as Richardson's intuitive picture predicted.

2.2.4 *Kolmogorov scales*

"Moreover, I soon understood that there was little hope of developing a pure, closed theory, and because of the absence of such a theory the investigation must be based on hypotheses obtained in processing experimental data."

A. N. Kolmogorov
(Tikhomirov 1991, p. 487)

In his seminal paper, Kolmogorov (1941) introduced two simple and powerful hypotheses on the statistics of locally homogenous and isotropic turbulent flows, which represented a crucial step in our understanding of turbulent flows. Kolmogorov (1941) starts by rigorously defining the terms "locally homogenous" and "locally isotropic". The key assumption is that at scales much smaller than the forcing scale, the flow properties become homogeneous and isotropic. We present here a simplified version of the discussion, and refer to Frisch (1996) for a more thorough presentation.

The main idea is conveyed by Kolmogorov's (1941) *"first hypothesis of similarity"*, which states for distribution functions F_n of small scale velocity increments

> *For the locally isotropic turbulence the distributions F_n are uniquely determined by the quantities v and ε.*

This statement allows us to find the small length scale η, where energy gets dissipated by viscosity. It is uniquely defined by viscosity v and energy dissipation rate ϵ and therefore must be

$$\eta = \left(v^3/\epsilon\right)^{1/4}.$$

Likewise, corresponding time and velocity scales can be obtained

$$\tau_K = \left(v/\varepsilon\right)^{1/2}, \qquad\qquad u_K = \eta/\tau_K = \left(\varepsilon v\right)^{1/4}.$$

These quantities correctly describe the smallest eddies of the flow and are known as the Kolmogorov length, Kolmogorov time, and Kolmogorov velocity respectively.

2.2.5   *Kolmogorov spectrum*

Kolmogorov's (1941) "*second hypothesis of similarity*" extends his first hypothesis and can be rephrased

> *For intermediate scales, larger than the dissipation scale η, the distribution laws F_n are uniquely determined by the quantity ε and do not depend on v.*

This statement may be used to derive a generic form of the energy spectrum $E(k)$. Like for the Kolmogorov scales above, one employs simple dimensional reasoning. When in the inertial range the spectrum $E(k)$ does only depend on the wavenumber k and, according to Kolmogorov's hypothesis, on the energy dissipation rate ε, it can only take the form

$$E(k) = C_K \varepsilon^{2/3} k^{-5/3}. \tag{2.14}$$

Here C_K is the dimensionless Kolmogorov constant. Sreenivasan (1995) reviews a large amount of data from experiments as well as numerical simulations and concludes, that the Kolmogorov constant is universally $C_K \approx 1.5$. Figure 2.5 shows the energy spectrum obtained in a famous wind-tunnel experiment by Comte-Bellot & Corrsin (1971). See also the energy spectrum obtained from our own numerical simulations in Figure 5.1. Typically a scaling according to Equation (2.14) becomes only clearly visible for very large Reynolds numbers.

Interestingly Equation (2.14), was not given by Kolmogorov himself, but has been derived independently by Obukhov (1941), Onsager (1945, 1949), and in collaboration by Heisenberg (1948) and von Weizsäcker (1948).
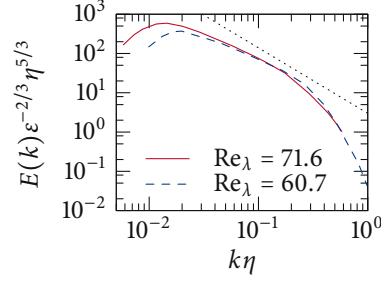
FIGURE 2.5
Data from an experiment by Comte-Bellot & Corrsin (1971). The straight dotted line gives the expected Kolmogorov scaling $\sim k^{-5/3}$. Typically for lower Reynolds numbers, this scaling is only valid in a limited range. That range extends for larger Reynolds numbers.

2.3   MOTION OF SPHERES IN A TURBULENT FLOW — THE MAXEY–RILEY EQUATIONS

In his paper entitled "On the Effect of the Internal Friction of Fluids on the Motion of Pendulums" Stokes (1851) derives the drag force acting on a small sphere of radius a, which moves uniformly with low velocity V through a fluid at rest. He obtains (Eq. (126) in the paper of 1851)

$$F_{\mathrm{drag}} = 6\pi a \mu V, \qquad (2.15)$$

where $\mu = \nu \rho_f$ is the dynamic fluid viscosity. From this result we can obtain in a hand-waving manner the equation of motion of a (small) particle moving freely in a turbulent flow. We assume that the size of the particle is much smaller than the smallest length scale of the flow, i.e., $a \ll \eta$. It therefore sees a laminar flow around itself and we may apply Equation (2.15). The relevant velocity is the difference between the particle velocity V and the fluid velocity $u(X, t)$ at the particle position X. In addition, we have to account for the (reduced) gravitational force acting on the particle $\frac{4}{3}\pi a^3 (\rho_p - \rho_f) G$. Assuming $\rho_f \ll \rho_p$ and therefore neglecting terms proportional to ρ_f / ρ_p, we obtain

$$\frac{\mathrm{d}}{\mathrm{d}t} X = V, \qquad (2.16)$$

$$\frac{\mathrm{d}}{\mathrm{d}t} V = \frac{u(X, t) - V}{\tau_p} + G, \qquad (2.17)$$

where we introduced the time scale

$$\tau_p = \frac{\frac{4}{3}\pi a^3 \rho_p}{6\pi a \nu \rho_f} = \frac{2}{9} \frac{\rho_p}{\rho_f} \frac{a^2}{\nu}. \qquad (2.18)$$

The time τ_p is obtained by comparing the mass of the particle, $\frac{4}{3}\pi a^3 \rho_p$ and the friction force, as expressed in the first equality in Equation (2.18).

This very much simplified approach misses several effects, such as the "added mass" or the "Basset history force" (Basset 1888; Boussinesq 1885; Oseen 1927). When the particle becomes bigger, further effects described by the Faxén (1922) corrections come into play. Maxey & Riley (1983) and Gatignol (1983) independently derived the full set of equations for freely

moving particles. Assuming $\rho_f \ll \rho_p$ and $a \ll \eta$ in their results, all additional terms vanish, leading again to Equations (2.16) and (2.17). They are therefore often referred to as the Maxey–Riley equations. Also, throughout the work at hand, we only consider small ($a \ll \eta$) but heavy ($\rho_f \ll \rho_p$) particles. Consequently the above set of equations in combination with the knowledge of the fluid velocity $\boldsymbol{u}(\boldsymbol{x}, t)$ at arbitrary points in space $\boldsymbol{x}$, fully determines the trajectories of particles in the studied cases. The work of Daitche & Tél (2011) is a reminder that the history term, neglected in Equations (2.16) and (2.17), becomes important when the particle radius becomes comparable to or larger than η. For further information and an overview of recent advances, we refer the reader to the review article by Toschi & Bodenschatz (2009).

2.3.1 *The Stokes number*

The particle relaxation time τ_p, Equation (2.18), may be compared to the shortest (fastest) time scale of the flow $\tau_\eta = (\nu/\epsilon)^{1/2}$. Their ratio defines the dimensionless Stokes number

$$\mathrm{St} = \frac{\tau_p}{\tau_\eta} = \frac{2}{9} \frac{\rho_p}{\rho_f} \left(\frac{a}{\eta} \right)^2, \qquad (2.19)$$

which, in a sense, measures the particles' inertia. For $\mathrm{St} \to 0$ the particles behave like tracer particles and follow the streamlines of the flow exactly. We underline again, that our definition of τ_p, Equation (2.18), is only valid for heavy particles with $\rho_p \gg \rho_f$. For light particles its definition changes and therefore also the right-hand side of Equation (2.19).

Another handy dimensionless quantity is the particle Reynolds number

$$\mathrm{Re}_p = 2a|\boldsymbol{u}(\boldsymbol{X}) - \boldsymbol{V}|/\nu.$$

It tells whether the assumption of smooth flow on the particle scale is valid—$\mathrm{Re}_p \ll 1$ in that case. Therefore it is good practice to observe Re_p, when one is using Equations (2.16) and (2.17), e.g., in a numerical simulation.

2.3.2 *The particle velocity gradient tensor*

For reasons that will become clear only later, we also introduce the particle velocity gradient tensor $\sigma_{ij} = \partial_j V_i$. Taking the partial derivative on both sides of Equation (2.17) and rearranging, yields

$$\frac{\mathrm{d}}{\mathrm{d}t}\sigma_{ij} = \frac{A_{ij}(\boldsymbol{X}, t) - \sigma_{ij}}{\tau_p} - \sigma_{ik}\sigma_{kj} \qquad (2.20)$$

where the velocity gradient tensor of the fluid $A_{ij}(\boldsymbol{x}, t) = \partial_j u_i(\boldsymbol{x}, t)$ was introduced. This equation has the mathematical form of a Matrix Riccati equation. The solutions of this type of differential equation typically display singularities. This type of behavior may at first seem surprising, but it has

physical significance, that will be discussed in Section 3.2.5. Furthermore, in Appendix B we discuss two ways to numerically overcome the caveat of those singularities.

3

INERTIAL PARTICLE COLLISIONS IN TURBULENT FLOWS

In the introduction (Section 1.1), we presented several problems, whose description relies on a good understanding of collisions between particles in a turbulent environment. Here, we discuss one of them, rain formation in clouds, in more detail. Another domain, the formation of planets in protoplanetary disks, will be rapidly reviewed. It will serve as justification for our choice of a broader parameter range than is of interest in the formerly mentioned context. Most technical aspects discussed in the coming sections are similarly applicable in other domains as well.

3.1 DROPLETS IN TURBULENT CLOUDS—AN OVERVIEW

The enormous range of involved length scales is commonly described as one of the most fascinating aspects of cloud microphysics, but it is also one of the most difficult to understand in quantitative terms. When approaching Earth from space, clouds are one of the first distinct features one can perceive. They can expand over lengths of hundreds of kilometers, while individual droplets and aerosol particles have radii of only several tenths of micrometers (Bodenschatz et al. 2010). Depending on what effects are taken into consideration, this range may even be extended in both directions (Siebesma et al. 2009). Evidently, clouds have a huge impact on our climate system and a better understanding is not only necessary for improved short term weather predictions, but also for long term projections of climate change—notably when aspects like "climate engineering" are discussed (Rickels et al. 2011). Consequently the interest in cloud physics has intensified in recent years. Particularly the influence of turbulence has been widely discussed and related progress is documented in many review articles.[1] Especially physicists started to adopt the topic, as can be seen for example in the focus issue, that Falkovich & Malinowski (2008) edited for the New Journal of Physics. Further reasons for the increased interest in cloud turbulence are certainly the improved numerical and experimental possibilities (Devenish et al. 2012). Here we shall present only the basic notions necessary for the understanding of the discussion of our work in the coming chapters. For individual details, we refer the reader to the already mentioned review articles.

---

1 A non-exhaustive list includes the papers of Beard & Ochs 1993; Blyth 1993; Devenish et al. 2012; Grabowski & Wang 2013; Jonas 1996; Pinsky & Khain 1997; Shaw 2003; Vaillancourt & Yau 2000.

3.1.1   *The droplet size distribution*

The life of a raindrop, from the moment it is formed by condensation to the time it has grown large enough to fall on Earth can be simplified as follows. First, it forms by condensation of vapor on tiny aerosol particles. Those are called cloud condensation nuclei (CCNs) and have sizes $< 1 \, \mu\text{m}$ (Devenish et al. 2012). Then comes a stage, where the droplets, continue to grow from initially $\sim 1 \, \mu\text{m}$ to a few tens of microns. This step is in the beginning still dominated by condensation, but the range between $15 \, \mu\text{m}$ and $40 \, \mu\text{m}$, known as the "size gap", is not very well understood (Grabowski & Wang 2013). Larger droplets can continue to grow by gravitational collisions in which they capture smaller ones with whom they coalesce. Different mechanisms have been proposed, that could drive droplet growth through the bottleneck of the size gap. One of them is turbulence, which can enhance the collision rate between medium sized droplets.

The whole process described above is conveyed for the ensemble of drops in a cloud by the droplet size distribution $f(a, \boldsymbol{x}, t)$. It gives the number density of droplets of radius a at position $\boldsymbol{x}$ and time t, in the sense that $\int_0^\infty f(a') \, \mathrm{d}a = n$, where n is the number density of all droplets in the volume (Shaw 2003). We will focus on warm clouds, that is clouds, whose top is still below the freezing level and assume a spatially homogenous distribution. In this case the droplet size distribution obeys the Boltzmann-type equation

$$
\begin{aligned}
\frac{\partial f(a)}{\partial t} = J(a) &- \frac{\partial}{\partial a} \left[\dot{a} f(a) \right] \\
&+ \frac{1}{2} \int_0^a \frac{a^2}{a''^2} \Gamma(a'', a') f(a'') f(a') \, \mathrm{d}a' \\
&- \int_0^\infty \Gamma(a, a') f(a) f(a') \, \mathrm{d}a', \quad (3.1)
\end{aligned}
$$

where we introduced the substitution $a'' = (a^3 - a'^3)^{1/3}$. The terms on the right-hand side consist of a particle source in form of the activation rate $J(a)$, a term representing growth by condensation and the two integral terms, which convey production and destruction of particles of radius a by collisions. We refer the interested reader to Shaw (2003) for a more detailed discussion.

In terms of the droplet size distribution, the aforementioned "size gap" problem corresponds to the question, how a distribution, that is initially sharply peaked around some smallish value of a, can develop into a broader distribution displaying a finite probability for larger droplet sizes. The figures of Berry & Reinhardt (1974a,b) illustrate this evolution nicely.

3.1.2   *The collision kernel*

The integrands in the two integrals on the right-hand side of Equation (3.1) depend on the collision kernel $\Gamma(a, a')$. It is defined as the proportionality

between the collision rate per unit volume of particles of radius a and a' and their respective number densities per unit volume

$$\mathcal{N}_c = nn'\Gamma(a, a').$$
(3.2)

In the monodisperse case, i.e., $a = a'$, a factor of ½ has to be added to the right-hand side to avoid double counting.

In realistic situations various phenomena contribute to $\Gamma(a, a')$. For example, larger particles falling faster in the gravitational field collect smaller ones, thus enhancing their mutual collision kernel. On the other hand, not all particles that come into contact will necessary coalesce—a fact typically accounted for by introducing a coagulation efficiency (see Section 3.2.7). In the remainder of this work, we will entirely concentrate on geometric collisions due to particle–turbulence interactions. All other effects, although important in more sophisticated models, will be neglected. This is a well established approach[2] allowing us to concentrate on a limited number of effects. We achieve a further simplification by limiting ourselves to the case of monodisperse solutions, thus writing simply $\Gamma(a)$ in that case.

Note that describing the droplet size distribution with Equation (3.1) requires the knowledge of the collision kernel $\Gamma(a, a')$ for different particle radii a and a'. Technically, this can be determined from numerical simulations of bidisperse solutions. Such simulations have been carried out, for example, by Bec et al. (2005). Typically the collision kernel is larger for solutions with particles of different sizes than for monodisperse ones. The review of various models for the collision kernel $\Gamma(a, a')$ presented by Ayala et al. (2008) reveals some of the differences between monodisperse and bidisperse solutions.

3.1.3 *Typical values*

Having briefly introduced the basic principles of droplet growth in clouds, we now discuss typical values of the two dimensionless quantities introduced in the last chapter—the Reynolds number and the Stokes number. Both depend implicitly on the energy dissipation rate ε found in clouds and the kinematic viscosity v of air. The latter is tabulated and varies with temperature (Haynes 2012). We assume an intermediate value of $v = 1.7 \times 10^{-5}\,\mathrm{m}^2/\mathrm{s}$. Measuring the energy dissipation rate in clouds is a complicated task. Usually, first the energy spectrum is determined from velocity measurements during flights by balloon (Kitchen & Caughey 1981), aircraft (Smith & Jonas 1995), or more recently by helicopter (Siebert et al. 2006b)[3], through clouds. Then, from the spectrum, using Equation (2.14) with some empirical Kolmogorov constant, the energy dissipation rate ε is determined. The measured value differs

---

2 See for example the works of Sundaram & Collins (1997), Wang et al. (2000), and Williams & Crane (1983). But we also note the studies of Rosa et al. (2013) and Woittiez et al. (2009), which suggest, that the combined effects of gravity and turbulence cannot be understood independently.

3 In fact, Siebert et al. (2006b) use a different, but conceptually similar approach.

depending on the type of cloud, its age, the region within the cloud, and other factors. In general, the energy dissipation rate ε has been documented to vary in between $10^{-3}\,\mathrm{m^2/s^3}$ and at least $10^{-1}\,\mathrm{m^2/s^3}$ (see Grabowski & Wang 2013; Pinsky & Khain 1997, and references therein).

Making use of the relation $\lambda/u_{\mathrm{rms}} = (15\nu/\varepsilon)^{1/2}$ (Pope 2000, p. 200), the energy dissipation rate ε and the root mean square velocity u_{rms} suffice to determine the Taylor scale Reynolds number Re_λ—see Equation (2.8). It is, again depending on the same various factors as ε, of the order of 10^3 to 10^4 (Siebert et al. 2010; Siebert et al. 2006a).

To estimate the Stokes number of droplets, we further need the densities of water and air, as well as the size of the droplets. The range of the latter has already been mentioned. The density of water at typical temperature and pressure is roughly $\rho_W \sim 1000\,\mathrm{kg/m^3}$, the density of air can be estimated $\rho_A \sim 1\,\mathrm{kg/m^3}$ (Haynes 2012). With these values we find from Equation (2.19) an upper bound for the Stokes number of about $\mathrm{St} < 1$.

Another important dimensionless number is the volume fraction Φ. Consider a given volume V containing N_p particles of size a, then the volume fraction is $\Phi = N_p \frac{4}{3}\pi a^3/V$. Its exact value depends on the droplet size and the type of cloud, but is typically of order 10^{-6} (Grabowski & Wang 2013). For a more detailed discussion, we refer to Pruppacher & Klett (1997, Sec. 2.1.3).

A word of caution

The simplifying approach often employed by physicists has repeatedly been criticized by the atmospheric research community (e.g., Grabowski & Vaillancourt 1999; Khain et al. 2007). This criticism is certainly justified, when one attempts to transpose the results to the cloud physical context without any further discussion. We argue however, that these simplifications are necessary to isolate different phenomena and to gain a deeper insight. In a second step, the improved understanding can be adopted in more complete models. Therefore, when in the coming chapters we present our results, we will deliberately extent the investigated range of Stokes numbers and neglect, as has been mentioned, aspects, like gravitation, that are incontrovertibly of huge importance in the context of clouds.

Dust grains in protoplanetary disks

Further motivation for our choice of an extended parameter range is provided by the fact that larger Stokes numbers may be important in other domains. In the astrophysical context where turbulence induced particle collisions are discussed as a possibly important factor in the formation of planets (Johansen et al. 2007; Safranov 1972; Shariff 2009), the experimental data is much more uncertain. But Stokes numbers of $\mathcal{O}(1)$ and larger are expected (Pan et al. 2011; Wilkinson et al. 2008). For a short overview of the domain, the interested reader is referred to Beckwith et al. (2000). We
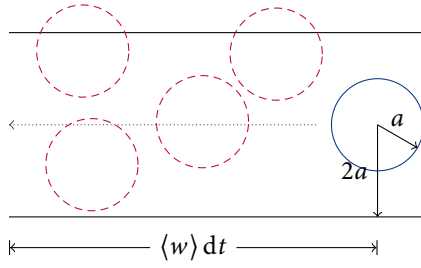
FIGURE 3.1

Consider a sphere of radius a moving on a straight line with average relative velocity $\langle w \rangle$ (with respect to the other particles). Such a sphere can collide per unit time with all particles in a cylinder of radius $2a$ and length $\langle w \rangle$ around its trajectory.

also note with anticipation that novel experimental work is under way by Capelo et al. (2013).

3.2 ANALYTICAL RESULTS ON COLLISION KERNELS

The collision kernel Γ has been defined in Section 3.1.2. In this section, we present different limiting cases, where the collision kernel can be analytically derived, as well as other important results.

3.2.1 *Collision kernel for an ideal gas*

To get a feeling for the typical reasoning, we start by deriving the collision rate in an ideal gas. To this end we follow the textbook by Moore (1972). The result obtained in this section will be used later, to verify our numerical collision detection scheme.

Imagine particles with a number density n, each moving with a constant normally distributed velocity V. The collision rate for any such particle can be calculated by considering the collision cylinder as shown in Figure 3.1. If all other particles were at rest, the considered particle would collide with all particles in a cylinder with radius $2a$ around its trajectory. Therefore, the corresponding collision rate per unit time would be $n\langle|V|\rangle\pi(2a)^2$. The other particles do however move and hence the correct velocity to determine the cylinder's height is the mean relative velocity $\langle w \rangle = 2^{1/2}\langle|V|\rangle$. To obtain the total collision rate per unit volume, the above quantity needs to be multiplied by $n/2$, finally leading to

$$\mathcal{N}_c = \frac{1}{2}n^2\sqrt{2}\pi(2a)^2\langle|V|\rangle. \tag{3.3}$$

Based on this result and according to Equation (3.2) we can then define the collision kernel for an ideal gas $\Gamma_{ig} = 2^{1/2}\pi(2a)^2\langle|V|\rangle$.

3.2.2 *Zero inertia*

Owing to its importance, but also to the difficulties involved in this task, much effort has been made to determine the collision kernel for turbulent flows. The paper by Saffman & Turner (1956) introduces some of the seminal
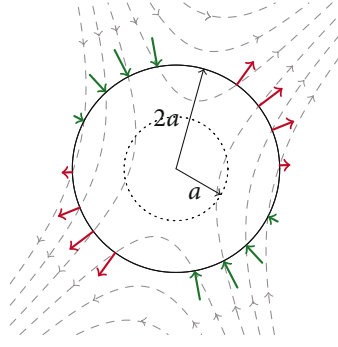
ideas. It describes a way to theoretically derive an estimate for the collision kernel of two particles of identical size, which follow the flow exactly, i.e., for the case St $\to$ 0. The main idea is illustrated in Figure 3.2. For a sphere of two times the particle radius a around one central particle, the total rate of inflow is determined. Multiplied by n, the number density of particles in the flow, this quantity determines the rate of collision $\mathcal{R}$ for the particle at the center. Mathematically this idea is described with the help of an integral over the surface of the sphere Ω

$$\mathcal{R} = n \int -w_r(2a, \Omega)\Theta[-w_r(2a, \Omega)]\,\mathrm{d}\Omega. \qquad (3.4)$$

This integral sums the radial component of the fluid velocity $w_r(\boldsymbol{x}, t)$ on the sphere, whenever it is negative—the Heaviside step function $\Theta(\cdot)$ assures that condition.

For an incompressible fluid the inflow and the outflow into a given volume cancel exactly. Therefore the integral in Equation (3.4) simplifies to

$$\int -w_r(2a, \Omega, t)\Theta[-w_r(2a, \Omega)]\,\mathrm{d}\Omega = \frac{1}{2}\int |w_r(2a, \Omega, t)|\,\mathrm{d}\Omega. \qquad (3.5)$$

Up to this point, only one central particle has been considered. To obtain an estimate for the overall collision rate, it is necessary to average $\mathcal{R}$. This further simplifies the situation, because for isotropic statistics it is now sufficient to consider $\langle|w_x(2a)|\rangle$. For small particles with radius $a \ll \eta$ this can be identified with $\langle|w_x(2a)|\rangle = 2a\langle|\partial u_x/\partial x|\rangle$. Taylor (1935) had found $\langle(\partial u_x/\partial x)^2\rangle = \varepsilon/15\nu$. With this result, assuming Gaussian statistics for the velocity gradients, Saffman & Turner (1956) finally obtain

$$\mathcal{N}_c = \frac{1}{2}n^2\Gamma_{ST}, \qquad \text{with} \quad \Gamma_{ST} = \frac{(2a)^3}{\tau_K}\left(\frac{8\pi}{15}\right)^{1/2}. \qquad (3.6)$$

In their paper Saffman & Turner go on to present a derivation of the collision rate for inertial particles—see Section 3.2.8 for a short comment on that part.

3.2.3 Infinite inertia

Abrahamson (1975) noted that most previous studies aiming at modeling the collision kernel for particles in a turbulent flow dealt with the case of

particles following the flow (St → 0). He argued that this condition is however not fulfilled in many situations and therefore derived the collision rate for a "vigorously turbulent fluid", which corresponds to the case St → ∞. In such a situation, particle velocities, even for those passing close to each other, can be considered randomly distributed. The correct approach to derive the corresponding collision rate is the same as for the ideal gas described in Section 3.2.1. Hence the problem reduces to estimating the average relative velocity between the particles. Assuming the velocities are Gaussian distributed, the average velocity can be related to the root mean square of its components

$$\langle |V| \rangle = 2\sqrt{\frac{2}{\pi}}\, V_{\mathrm{rms}}. \tag{3.7}$$

Based on Corrsin's hypothesis on the relation between Lagrangian and Eulerian correlation functions and following former work by others, Abrahamson (1975) obtains from a simplified version of the Maxey–Riley equations (Section 2.3), adequate for particles with large Stokes numbers,

$$V_{\mathrm{rms}}^2 = \frac{u_{\mathrm{rms}}^2}{1 + \frac{3}{2}\tau_p \varepsilon / u_{\mathrm{rms}}^2} = \left(\frac{\eta}{\tau_K}\right)^2 \frac{\mathrm{Re}_\lambda}{2\sqrt{15} + 45\,\mathrm{St}/\mathrm{Re}_\lambda},$$

where in the second step $\varepsilon = \eta^2/\tau_K^3$ and $(u_K/u_{\mathrm{rms}})^2 = 15^{1/2}/\mathrm{Re}_\lambda$ (see, e.g., Pope 2000) have been used. Given the empirical reasoning involved in the derivation of the above result, the exact factors may vary, but it is important to note the functional form $V_{\mathrm{rms}} = (\eta/\tau_K)\gamma(\mathrm{St}, \mathrm{Re}_\lambda)$. Combining this result with Equations (3.3) and (3.7), Abrahamson (1975) obtains the collision kernel

$$\Gamma_A = 4\sqrt{\pi}(2a)^2 \frac{\eta}{\tau_K}\gamma(\mathrm{St}, \mathrm{Re}_\lambda), \tag{3.8}$$

which differs from Saffman & Turner's result by a factor $\sim \eta/a$.

Mehlig et al. (2007) point out, that Abrahamson did not account for the "multiscale nature of the flow". They provide a different approach based on Kolmogorov-type reasoning: In the inertial range, V_{rms} can only depend on the dissipation rate ε and the particle relaxation time τ_p. By dimensional analysis they find $\gamma(\mathrm{St}, \mathrm{Re}_\lambda) \sim \mathrm{St}^{1/2}$ with a possibly Reynolds number dependent prefactor.

3.2.4 *Preferential concentration*

In both turbulent cases presented above—zero and infinite inertia—the particles are distributed homogeneously. Maxey (1987) however noted, that for inertial particles with intermediate Stokes numbers, the particle velocity field becomes compressible and particles tend to cluster in certain regions

of the flow. This becomes obvious, when one writes the formal solution of Equation (2.17)[4]

$$V(t) = \int_0^t e^{(t'-t)/\tau_p} \left(\frac{u(t')}{\tau_p} + G \right) dt'.$$

Assuming small inertia, the above equation can be developed in τ_p by consecutive integration by parts

$$V = u + \tau_p G - \tau_p \dot{u} + \mathcal{O}(\tau_p^2), \qquad (3.9)$$

where $\dot{u}$ has to be interpreted as the material derivative $\partial_t u + u \cdot \nabla u$. Taking the divergence of Equation (3.9) yields

$$\begin{aligned} \nabla \cdot V &= -\tau_p \nabla \cdot (u \cdot \nabla u) = -\tau_p (\partial_i u_j)(\partial_j u_i) \\ &= \frac{\tau_p}{4} [(\partial_i u_j + \partial_j u_i)^2 - (\partial_i u_j - \partial_j u_i)^2]. \end{aligned}$$

The first term in the square brackets can be related to the so called "rate of strain tensor", the second term to the vorticity (see Section 2.1.1). Maxey (1987) concluded, that the particle velocity field is divergent in regions of high vorticity, while it is convergent in regions of high strain. Therefore the particles would get ejected from vortices and cluster in regions of low vorticity.

Later work by Wilkinson et al. (2007) and Gustavsson & Mehlig (2011b) provides an alternative approach. Their analytical results, which they obtain for a model flow, are able to explain features present in numerical simulations of turbulent flows.

The clustering, or preferential concentration, evidently needs to be taken into account, when one determines the collision kernel. In the following, we present the approach introduced by Sundaram & Collins (1997), which is based on ideas from statistical mechanics.

RADIAL DISTRIBUTION FUNCTION   Consider a system with N_p particles. We define the probability that particle "1" is in dX_1 at X_1, particle "2" is in dX_2 at X_2, etc. $P^{(N_p)}(X_1, \ldots X_{N_p})$. Then the probability that *any* two particles are in dX_1 at X_1 and in dX_2 at X_2 is (e.g., McQuarrie 1976)

$$\varpi^{(2)}(X_1, X_2) = N_p(N_p - 1)P^{(2)}(X_1, X_2). \qquad (3.10)$$

A further useful definition is the radial distribution function (RDF)

$$g^{(2)}(X_1, X_2) = n^{-2} \varpi^{(2)}(X_1, X_2).$$

For isotropic statistics all above quantities only depend on the two particles' distance $r = X_2 - X_1$. In this case one has $P^{(2)}(X_1, X_2) = P(r)/V$ and can define

$$g(r) = \frac{N_p(N_p - 1)}{n^2 V} P(r), \qquad (3.11)$$

where we dropped the upper index for simplicity.

---

4 Here we omit the argument $X(t)$, which should in principle appear in V and u. See the original paper by Maxey (1987) for a more rigorous treatment.

JOINT PROBABILITY   To decide whether two particles are about to collide, one needs, aside from their distance, knowledge about the relative velocity $w = V_2 - V_1$. Therefore, instead of the above probability $P^{(2)}(X_1, X_2)$, one has to consider the joint probability of position and velocity $P^{(2)}(X_1, V_1; X_2, V_2)$. Here again, we can make use of isotropy, which means $P(r, w)$ is enough to describe the statistics. The latter can be beneficially rewritten with the help of the conditional probability $P(w|r)$

$$P(r, w) = P(w|r)P(r) = P(w|r)g(r)\frac{n^2 V}{N_p(N_p - 1)}, \qquad (3.12)$$

where in the second equality the RDF from Equation (3.11) was introduced.

COLLISION OPERATOR   It is convenient to introduce a function that, based on the values of r and w, recognizes whether a pair of particles is going to collide. Sundaram & Collins (1997) rigorously construct a function $\psi(r, w; \tau)$, which returns 1 if the particles collide within a time τ, and 0 if not. We shall see, that the derivative with respect to τ is enough to determine the collision rate. Sundaram & Collins (1997) obtain

$$\frac{\mathrm{d}\psi(r, w; 0)}{\mathrm{d}\tau} = -w_r\Theta(-w_r)\delta(2a - r), \qquad (3.13)$$

where

$$w_r = \frac{(V_2 - V_1) \cdot (X_2 - X_1)}{|X_2 - X_1|}$$

is the radial relative velocity (RRV) and $\Theta(\cdot)$ and $\delta(\cdot)$ are respectively the Heaviside and Dirac functions. Note that this is again simply Saffman & Turner's (1956) integral kernel—see Equation (3.4).

COLLISION RATE   Now we put together Equations (3.10) and (3.12), as well as the collision operator, to determine the number of collisions that happen in a time τ

$$N_c(\tau) = \frac{1}{2}N_p(N_p - 1) \iint \psi(r, w; \tau)P(w|r)g(r)\frac{n^2 V}{N_p(N_p - 1)} \, \mathrm{d}r \, \mathrm{d}w.$$

From $N_c(\tau)$ the collision rate per unit volume may be obtained by derivation with respect to τ and division by V

$$\mathcal{N}_c = \frac{1}{V}\lim_{\tau \to 0}\frac{N_c(\tau)}{\tau} = \frac{1}{V}\frac{\mathrm{d}N_c(\tau)}{\mathrm{d}\tau}.$$

Noting that $\psi(r, w; \tau)$ is the only τ-dependent term and introducing Equation (3.13), Sundaram & Collins (1997) finally obtain

$$\mathcal{N}_c = \frac{1}{2}n^2 4\pi(2a)^2 g(2a) \int_{-\infty}^{0} -w_r P(w_r|2a) \, \mathrm{d}w_r.$$

Making the same argument as in Equation (3.5), one can write for the collision kernel

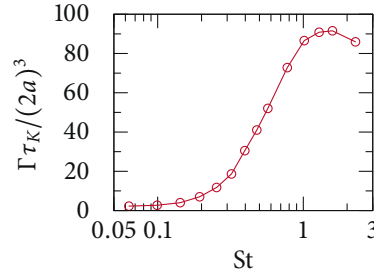$$\Gamma_{SC} = 2\pi(2a)^2 \langle|w_r|\rangle g(2a), \qquad (3.14)$$

FIGURE 3.3
The collision kernel as determined in a numerical simulation by Rosa et al. (2013) at $Re_\lambda \sim 200$. Note the strong increase at about $St \sim 0.5$. For larger Stokes numbers the collision rate decreases only slowly.

which differs from Saffman & Turner's collision kernel, Equation (3.6), only by the appearance of the RDF, that accounts for preferential concentration. But note also, that—as opposed to the former results—no explicit expression is given for the RRV $\langle |w_r| \rangle$.

3.2.5 *Caustic/sling collisions and random uncorrelated motion*

Falkovich et al. (2002) and Wilkinson et al. (2006) noticed independently that the enhancement of the collision rate may not be solely due to the preferential concentration effect. In fact, they predicted another mechanism, which could explain the very strong increase in the concentration rate observed at $St \sim 0.5$ (Figure 3.3). This effect is due to an increase of the RRV, independently of the clustering of particles. It has recently been verified experimentally by Bewley et al. (2013).

A third independent approach to describe the same phenomenon was presented by Février et al. (2005) and Simonin et al. (2006). It has become known as "random uncorrelated motion" (Reeks et al. 2006), and will be discussed shortly towards the end of this section.

CAUSTICS   Wilkinson et al. (2006) remind that according to the approach of Maxey (1987) the clustering should be most pronounced for $St \sim 1$. Numerical results, like those shown in Figure 3.3, however show that the collision rate starts to grow explosively for $St \ll 1$. Furthermore, the collision rate does not abruptly fall for $St > 1$, but slowly approaches Abrahamson's (1975) prediction for $St \to \infty$. Wilkinson et al. (2006) argue further, that the usual clustering process could only bring together particles on a distance similar to the smallest scales of the flow. In a typical cloud however—see Section 3.1.3—there is on average only one droplet per cube of edge size η. Therefore Wilkinson et al. (2006) provide a different explanation for the observed enhancement of the collision rate.

An initially single valued distribution of inertial particles in phase space may become multivalued due to the formation of so-called "caustics". This effect is similar to the formation of shocks in Burgers' equation (Frisch & Bec 2001) or to the formation of the characteristic light pattern that can be observed on the ground of a swimming pool, from which this effect borrows its name (Berry 1981). Consider the one-dimensional example depicted in
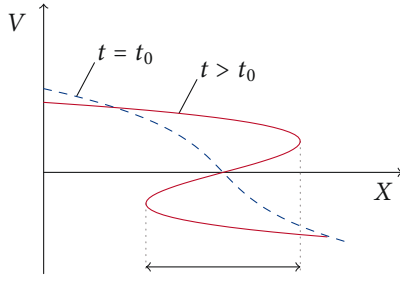
FIGURE 3.4

The particle phase space is spanned by their position X and velocity V. The lines may be interpreted as manifolds on which the particles are distributed homogeneously. Although initially there is only one particle at each position, particles overtake each other leading to the formation of a fold caustic (comp. Wilkinson et al. 2006).

Figure 3.4. Over the course of time, faster particles will overtake slower ones. Those with negative velocities will move to the left, those with positive velocities will move to the right. Thus a region, where the particle velocity field is multivalued develops in coordinate space. This has two consequences, which can potentially lead to collisions. On the one hand, particles may find themselves close to each other, but with largely differing velocities. In this case Abrahamson's (1975) approach for uncorrelated particle motion is more appropriate to describe the collision rate, than Saffman & Turner's (1956). On the other hand, the number density of particles diverges at the edges of the caustics. Wilkinson & Mehlig (2005) had investigated this in an earlier publication, but do consider its contribution to the collision rate negligible in systems, where $n\eta^3 \ll 1$.

In the presence of caustics, an obvious decomposition of the collision kernel is

$$\Gamma = \Gamma_{ST}\, g(2a) + \Gamma_A\, h_S(\text{St}, \text{Re}_\lambda), \tag{3.15}$$

where the RDF $g(2a)$ has been introduced according to (3.14) to account for the effect of preferential concentration, which affects only shear induced collisions. The function $h_S(\text{St}, \text{Re}_\lambda)$ can be interpreted as the fraction of position space, where the velocity has become multivalued due to the formation of caustics (Wilkinson et al. 2006). This quantity can be related to the rate of caustic formation, which Wilkinson & Mehlig (2003) had determined analytically for a model flow in a previous publication. From their results it is finally concluded, that $h_S(\text{St}, \text{Re}_\lambda) = \exp(-C/\text{St})$ with some universal dimensionless constant C. Duncan et al. (2005) determined this constant for particles advected by a three-dimensional random vector field. In a subsequent work Falkovich & Pumir (2007) could confirm the functional form of $h_S(\text{St}, \text{Re}_\lambda)$ in a DNS of turbulent flow. They found in addition, that the constant C falls with growing Re_λ.

SLING EFFECT   Falkovich et al. (2002) predicted the sharp increase in the collision rate using a different string of arguments. They imagine particles getting ejected out of vortices, like stones from a sling. These particles will have a large RRV when they collide, as well as a totally uncorrelated motion with the particles they collide with. The caustics and sling effects turn out to be essentially the same, despite the two different approaches and presentations.

RELATION TO PARTICLE VELOCITY GRADIENT   Consider Figure 3.4 again. It is obvious that the formation of a caustic is accompanied by the divergence of the quantity $\mathrm{d}V/\mathrm{d}X$ on its edges. In three dimensions this translates to singularities of the particle velocity gradient tensor σ_{ij} as introduced in Equation (2.20). Therefore this quantity was used by Falkovich & Pumir (2004, 2007) to study the sling effect. If one has access to σ_{ij} for each particle in every collision, it is even possible to estimate the ratio of sling collisions. This has been done by Ducasse & Pumir (2009) in a model flow (kinematic simulations).

RANDOM UNCORRELATED MOTION   Yet another way of describing essentially the same phenomenon has been proposed by Février et al. (2005) and Simonin et al. (2006). They note that the velocity field describing the motion of inertial particles can be decomposed into two contributions. One describing the smooth spatially correlated movement of the particles and another one describing "random uncorrelated motion" (Reeks et al. 2006). The latter is responsible for caustics and sling collisions.

IJzermans et al. (2010) present a method to study similar effects based on the deformation of an infinitesimal volume around a particle along its trajectory. This work was extended by Meneguz & Reeks (2011). The relationship between the different interpretations described in this section is discussed and studied in two model flows by Gustavsson et al. (2012).

3.2.6   *Ghost collision approximation*

A typical simplification, when studying collisions in numerical simulations is the so-called "ghost collision approximation" (GCA). A collision is detected whenever the distance between two particles falls below the collision radius $2a$, but the particles do not interact in any way and are allowed to overlap. When the particles separate and collide again afterward, either with each other or with further particles, these contacts are counted as new collisions. Evidently, this approximation leads to an overestimation of the collision rate—this has been noted by Zhou et al. (1998). Also the preferential concentration effect is affected by the GCA, as Reade & Collins (2000) show. They compare the RDF obtained from simulations with ghost particles and from simulations, where particles bounce off each other like hard spheres. The two values for $g(r)$ differ with a dependence on the Stokes number St and the particle size a.

The inaccuracy of the GCA is by no means restricted to a particular numerical algorithm. In fact, Andersson et al. (2007) and Gustavsson et al. (2008) point out, that all theories based on similar reasoning as introduced by Saffman & Turner (1956) suffer from this inaccuracy. When in Equation (3.4) the amount of inflowing fluid is summed up by the integral, it is not asked, whether it is "fresh fluid", which enters the sphere. In a turbulent flow it is however possible, that a parcel of fluid traverses the collision sphere several times. In this case, only the first passage should be counted

in for the collision rate. Saffman & Turner considered a locally hyperbolic flow as shown in Figure 3.2, which they assumed to be persistent. This is however incorrect: a turbulent flow is neither at every instant and space point hyperbolic (Bec 2005; Chong et al. 1990) nor is its structure persistent in time (Brunk et al. 1998b). To circumvent the problems associated with fluid elements that pass the collision sphere multiple times, Andersson et al. (2007) propose to incorporate an indicator function in Equation (3.4), such that

$$\mathcal{R} = n \int -w_r(2a, \Omega)\Theta[-w_r(2a, \Omega)]\chi(2a, \Omega) \, \mathrm{d}\Omega. \qquad (3.16)$$

The indicator function χ is unity only if the point reaching the surface of the sphere at $(\Omega, 2a)$ has not previously traversed it, elsewise it is zero. This function is analytically hard to determine though, as in principle it necessitates knowledge about the full history of every fluid element.

We finally mention the work by Wang et al. (2005b) who study the combined effect of the GCA and hydrodynamic interactions in terms of a collision efficiency (see next section). Their work is interesting from an engineer's point of view, as it provides a simple way to compensate the bias introduced by the GCA. From a physical point of view it is however unsatisfactory as it seems to miss a conclusive explanation of the origins of that bias. One of the main objectives of this work has been to provide a better understanding of the biases introduced by the GCA. Our results are presented in Chapter 6.

3.2.7 *Collision efficiency*

In most of the work dealing with collisions in turbulent flows, the interactions between particles are effectively neglected. In particular, hydrodynamic forces are not taken into account. These interactions may however cause a reduction of the collision rate (Brunk et al. 1998a,b, demonstrate this for coagulating particles). Usually these effects are described with the help of an effective collision radius, from which the collision efficiency $0 \le \mathcal{E}_c \le 1$ can be obtained (Pruppacher & Klett 1997). This effective collision efficiency is then introduced in the above expressions for the collision kernel as a multiplicative factor. We refer the interested reader to Pruppacher & Klett (1997) for an overview.

3.2.8 *Two interesting remarks*

In the late 1990s and early 2000s some interesting remarks concerning the derivation of collision kernels were made by L.-P. Wang and co-workers. Here we briefly summarize two important results that will be helpful in the coming chapters.

Wang et al. (1998b) noted that two different ways to model collisions were used in theoretical descriptions of the collision kernel. On the one hand, there is the "cylindrical formulation", similar to the one we presented in

Section 3.2.1, on the other hand there is the "spherical formulation" as used by Saffman & Turner (Section 3.2.2). The former makes the assumption of uniform relative velocity w, at least on the scale of the collision radius $2a$. This assumption is correct in the case of Maxwellian particles, it fails however for turbulent flows at intermediate Stokes numbers. In addition to the one we presented in Section 3.2.2, Saffman & Turner (1956) give a second derivation of the collision kernel, this time for inertial particles. That result differs from the one in Equation (3.6), but they explain the discrepancy with inexact assumptions made on the turbulent flow. Wang et al. (1998b) show that actually Saffman & Turner's (1956) second derivation differs from the first, in that it makes use of the "cylindrical formulation". The correct approach is however, as Wang et al. (1998b) go on to demonstrate, the "spherical formulation".

Another remark with practical importance is made by Wang et al. (2000). It explains an effect which may seem puzzling at first: When one determines, for example in a numerical simulation, the average radial relative particle velocity $\langle |w_r| \rangle_c$, based *only* on colliding particles, then the result differs from the one obtained, when one takes into account *all* pairs at a distance $2a$. Obviously, the correct average $\langle |w_r| \rangle$ is the one that considers all pairs, but interestingly the two values can be related. To this end it is helpful to reflect the procedure, how $\langle |w_r| \rangle_c$ would be calculated. Consider again Saffman & Turner's (1956) picture of one central particle and especially only one surface element $d\Omega$ of the collision sphere. For each such surface element, the radial relative velocity $|w_r|$ is registered and summed up at a rate $d\mathcal{R} = -nw_r(2a, \Omega)\Theta[-w_r(2a, \Omega)]\,d\Omega$ (comp. Equation (3.4)). By integrating over the sphere, averaging, and multiplying $\frac{1}{2}n$ to account for all particles, one obtains the sum of $|w_r|$ from all collisions per volume and time,

$$(\mathcal{V}\mathcal{T})^{-1} \sum_{\text{collisions}} |w_r| \approx n^2\pi(2a)^2\langle |w_r|^2 \rangle.$$

In this casual notation $\mathcal{V}$ and $\mathcal{T}$ simply mean the observation volume and time. From the above quantity the average radial relative velocity conditioned on collisions, $\langle w_r \rangle_c$, is obtained by normalizing with the number of collisions per volume and time $\mathcal{N}_c$—Equation (3.6). One finally obtains

$$\langle |w_r| \rangle_c = \frac{\langle w_r^2 \rangle}{\langle |w_r| \rangle}, \tag{3.17}$$

which is the result given by Wang et al. (2000). Although maybe confusing at first, this result is numerically verified and will be of importance in Section 4.3. Furthermore Ducasse (2009) discusses interesting implications that arise from this result for the PDFs of collision angles.

Part II

MAIN SCIENTIFIC WORK OF THE THESIS

4

COLLISION DETECTION AND IDEAL GAS PARTICLES

The work carried out in this thesis is based on numerical simulations of turbulent flows, in which we follow particles. The detection of collisions between particles requires some careful treatment of the numerical data, which we explain in this chapter. Some more technical aspects will be discussed in the appendix.

In Section 3.2.1 the collision kernel for an ideal gas was derived. This simple case will be used in the following to check our scheme. In addition some results, which are of interest in the coming chapters, will be derived for this simple example.

4.1 COLLISION DETECTION SCHEME

To detect collisions in a system of N_p particles, one may want to check all particle pairs, which requires of the order of $\mathcal{O}(N_p^2)$ operations. In some of our simulations we have up to $\mathcal{O}(10^7)$ particles. With such a number of particles, the simple-minded approach leads to a prohibitively expensive computational cost. It is however common to use a technique originally developed in molecular dynamics simulations called "cell linked-list" algorithm (Allen & Tildesley 1989) to reduce that cost. Sundaram & Collins (1996) describe an implementation of this technique to study collisions of inertial particles in a turbulent flow.

4.1.1 *Cell linked-list algorithm*

The basic idea of the cell list algorithm is, that only particles in a certain region around one central particle can collide with that particle during the next time-step. To make use of this observation, the (cubic) computational domain is divided into N_b^d boxes, where d is the dimensionality of the system—in our case $d = 3$. In a first step, a list of particles in each box is generated. Then, each particle in every box is checked for a collision with any particle in the $(3^d - 1)$ surrounding boxes. In the ideal case, N_b would be chosen such that each box contains only one particle (or even less). Then the computational cost would reduce to a mere $\mathcal{O}(N_p)$. There is however a minimal size for the boxes, which is given by the maximal distance, one particle can travel within one time-step. When the simulation domain has length L_{sys} in all directions, each box has length $L_b = L_{sys}/N_b$. Now consider the situation illustrated in Figure 4.1—two particles move with maximal velocity V_{max} perpendicular to the cell. One particle is located at the far end of the cell under consideration, the other one on the near end of the next but one cell. If the collision between these two particles would take
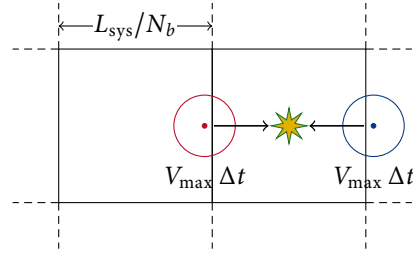
place within the next time-step, it would be missed by the cell list algorithm. Therefore the maximal number of boxes per direction is

$$N_b = L_{\text{sys}}/[2(V_{\text{max}}\,\Delta t + a)],$$

where Δt is the time-step and a is the particle radius. Typically this constraint is not too restrictive. But other effects, like particle clustering can reduce the efficiency of this approach.

There are other algorithms, like k-d trees, which require of the order of $N_p \log N_p$ operations to determine nearest neighbors, and can therefore further reduce the computational cost of detecting collisions. But in systems, where the particles are sufficiently homogeneously distributed and where the constraint on N_b is not too strong, they are unlikely to perform better than the cell linked-list algorithm. This showed also in some comparative tests we did with a freely available implementation of the k-d tree algorithm (Kennel 2004).

4.1.2   Trajectory interpolation

In Section 4.1.1 it has been described, how the number of particle pairs that need to be checked for eventual collisions can be reduced. It was however not explained, how a collision could be detected for a given pair. Simply measuring the distance between the two particles is not enough, because one cannot tell whether they have been in contact before. A more elaborate approach consists in taking into account the two particles' positions and velocities at one time-step. Then one can extrapolate their trajectories linearly and determine whether they approach closer than $2a$ within the next time-step. With a sufficiently small time-step, this approach is correct. But usually one has interest to keep the time-step as large as possible. In this case problems like the one illustrated in Figure 4.2 may arise. Therefore we used a more sophisticated approach in our simulations. Particle positions and velocities of two consecutive time-steps are stored. This allows a third-order interpolation of the trajectories, which is more accurate. Comparing the two approaches in a typical situation, we found that the linear extrapolation detected up to 5 % collisions in excess and missed a few others. In Appendix A both approaches are discussed in more detail.
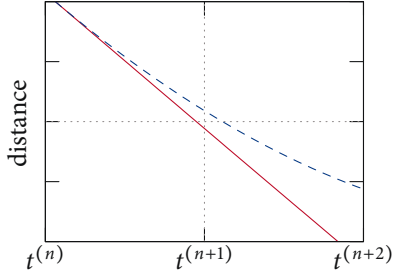
FIGURE 4.2

The dashed line shows the exact distance between a pair of particles over the course of two time-steps. The straight line corresponds to a linear extrapolation at time-step $t^{(n)}$. This falsely predicts a collision. At the next time-step $t^{(n+1)}$ a second collision would be counted.

4.1.3 *Numerical determination of the main variables*

The variables we are most interested in are the collision kernel Γ, the mean RRV $\langle |w_r| \rangle$, and the RDF $g(2a)$ at the collision distance $2a$. All these quantities have been introduced in Chapter 3. In the following paragraphs we explain how they are determined numerically.

COLLISION KERNEL   The collision detection scheme allows to determine the number of collisions $N_c(\tau)$ that take place in a time interval of length τ. Then the collision rate per time and volume in this interval is

$$\mathcal{N}_c = \frac{N_c(\tau)}{\tau \mathcal{V}_{\text{sys}}}, \tag{4.1}$$

where $\mathcal{V}_{\text{sys}}$ is the volume investigated for collisions. From Equation (4.1) the instantaneous collision kernel can be derived

$$\Gamma_\tau = \frac{2 \mathcal{V}_{\text{sys}} N_c(\tau)}{\tau N_p^2}. \tag{4.2}$$

The final value for the collision kernel Γ is obtained by averaging over consecutive intervals. This procedure also provides an estimate for the uncertainty in the determination of the collision kernel, namely the standard error of the mean (Sachs & Hedderich 2006).

For the length τ of the interval, we usually choose a large time scale of the flow. In the DNS, which will be introduced in the next chapter, we use the large eddy turnover time T_L.

RADIAL DISTRIBUTION FUNCTION   To determine the RDF at contact $g(2a)$, the cell-linked list algorithm gets employed again, but this time to detect all particle pairs that have a separation $2a - \Delta r/2 < r < 2a + \Delta r/2$, where Δr is some very small distance. Different values of Δr were tested. If the value is chosen too small, one will detect almost no pairs and therefore introduce a large statistical uncertainty. If on the other hand Δr is too large, the variation of the function $g(r)$ can not be neglected anymore in the range $2a \pm \Delta r/2$. All results reported on in this work were obtained with $\Delta r = 0.04a$, which was found to give correct results. Given the number N_{2a}

of particle pairs with a separation $2a$ at one time-step, the momentary RDF can be obtained from Equation (3.11)

$$g(2a)_{\Delta t} = \frac{N_{2a}\mathcal{V}_{\mathrm{sys}}}{\mathcal{V}_\odot N_p^2/2},$$

(4.3)

where $\mathcal{V}_\odot = \frac{4}{3}\pi\big[(2a+\Delta r)^3 - (2a+\Delta r)^3\big]$ is the volume of the shell around each particle, in which other particles were searched. Note that Equation (4.3) gives the RDF at one instant in time, i.e., at one time-step. It is not necessary to apply the interpolation used to detect collisions in between time-steps. Again, the final result $g(2a)$ is obtained by averaging over all time-steps.

RADIAL RELATIVE VELOCITY   As before, all particle pairs in a distance $2a$ of each other are detected. For each such pair the RRV $|w_r|$ is calculated and by averaging over all pairs and all time-steps, one obtains $\langle|w_r|\rangle$.

4.2   PARTICLES WITH GAUSSIAN VELOCITY DISTRIBUTION

In this section we consider a system of particles, whose velocity components are distributed according to a Gaussian

$$p(V_i) = \frac{1}{\varsigma\sqrt{2\pi}}\exp\left(-\frac{V_i^2}{2\varsigma^2}\right),$$

(4.4)

where the notation $\varsigma = V_{\mathrm{rms}}$ was introduced for clarity of presentation. This situation corresponds to the classic model for an ideal gas. In Section 3.2.1, the collision kernel for this case was derived. We chose this special system for two reasons: First, it is useful to calibrate our collision detection algorithms. Second, it will allow a relatively simple access to a first theoretical description of some not yet studied aspects.

4.2.1   *Verification of collision detection scheme*

We applied our implementation of the techniques described in the above sections, to a set of particles with constant (in time) velocities according to Equation (4.4). The expected mean velocity is $\langle|V|\rangle = 2^{3/2}\varsigma\pi^{-1/2}$. Therefore the collision kernel can be expressed in terms of ς as

$$\Gamma_{ig} = 4\sqrt{\pi}\varsigma(2a)^2.$$

We have determined the collision kernel in our numerical simulations by counting the number of collisions per time and volume. Table 4.1 shows a comparison between the results and the theoretical predictions for three different ratios of the particle radius a over the size of the simulation box L_{sys}. The boundary conditions were, as always throughout this work, periodic. The results confirm the correctness of our implementation.

a/L_{sys}	$\Gamma/4\sqrt{\pi}\sigma(2a)^2$
2.1×10^{-4}	0.9995 ± 0.0003
3.0×10^{-4}	1.0001 ± 0.0007
3.8×10^{-4}	1.0003 ± 0.0014

TABLE 4.1
The theoretical prediction and our measured collision kernel match very well, confirming our collision detection scheme. The uncertainty increases due to slightly poorer statistics for larger particles.

4.3   CONTACT TIMES

In Section 6.3 we will be interested in the time τ_c that two inertial particles spend closer than a certain distance d_c in a turbulent flow. For the choice $d_c = 2a$ this time corresponds to the contact time of particles. In this section we will derive the PDF of this quantity for an ideal gas of particles with radius a. To this end we start by deriving the PDF of relative velocities *only* for collisions.

4.3.1   *Probability of relative velocity and statistics conditioned on collisions*

The PDF of the relative velocity $\boldsymbol{w} = \boldsymbol{V}_2 - \boldsymbol{V}_1$ between two particles in a Maxwellian gas can be determined from Equation (4.4). Elementary algebraic manipulations lead to

$$p(\boldsymbol{w}) = \frac{1}{(2\sqrt{\pi}\varsigma)^3} \exp\left(-\frac{\boldsymbol{w} \cdot \boldsymbol{w}}{4\varsigma^2}\right), \qquad (4.5)$$

where it was assumed that all particles and all velocity components are independent.

To determine the PDF of $\boldsymbol{w}$, conditioned on the fact that the particles are about to collide, one proceeds as described in Section 3.2.8. One obtains in analogy to Equation (3.17)

$$p_c(\boldsymbol{w}_c) = \int \delta(\boldsymbol{w} - \boldsymbol{w}_c) \frac{-2w_r \Theta(-w_r)}{\langle|w_r|\rangle} p(\boldsymbol{w}) \, \mathrm{d}^3 w, \qquad (4.6)$$

where the Heaviside step function $\Theta(\cdot)$ picks only negative RRVs. The index c indicates that the PDF is restricted to collision events.

Equation (4.6) can be evaluated for an ideal gas, if one takes into account isotropy. Without loss of generality one may assume that $w_r = w_z$. Inserting Equation (4.5) yields

$$p_c(\boldsymbol{w}) = \frac{\boldsymbol{w} \cdot \hat{\boldsymbol{z}}}{2^3 \varsigma^4 \pi} \Theta(\boldsymbol{w} \cdot \hat{\boldsymbol{z}}) \exp\left(-\frac{\boldsymbol{w} \cdot \boldsymbol{w}}{4\varsigma^2}\right), \qquad (4.7)$$

where $\hat{\boldsymbol{z}}$ designates the unit vector in z-direction. Note that we dropped the index c on the relative velocity $\boldsymbol{w}$, assuming that it suffices to indicate it at the probability distribution itself.
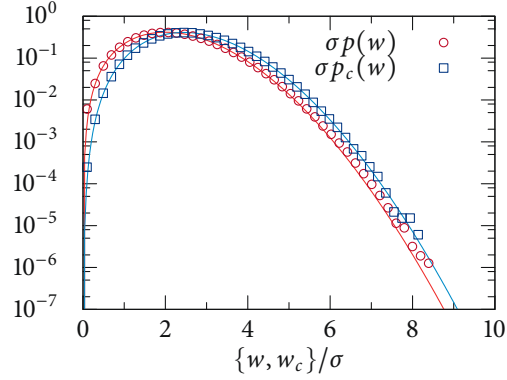
FIGURE 4.3

Numerical verification of Equation (4.8) shown here as lines. The points represent the results of a numerical simulation.

At this point it is instructive to perform a simple numerical experiment. To this end we first transform Equations (4.5) and (4.7) to spherical coordinates

$$\boldsymbol{w} \cdot \hat{\boldsymbol{x}} = w \sin(\theta) \cos(\phi),$$
$$\boldsymbol{w} \cdot \hat{\boldsymbol{y}} = w \sin(\theta) \sin(\phi),$$
$$\boldsymbol{w} \cdot \hat{\boldsymbol{z}} = w \cos(\theta).$$

Then we integrate the polar and azimuthal contributions to obtain the PDFs of the absolute value of the relative velocity. The final results are

$$p(w) = \frac{w^2}{2\sqrt{\pi}\varsigma^3} e^{-w^2/(2\varsigma)^2} \quad \text{and} \quad p_c(w) = \frac{2w^3}{(2\varsigma)^4} e^{-w^2/(2\varsigma)^2}. \quad (4.8)$$

We estimated both PDFs in a numerical simulation, taking into account all particle pairs in the one case, and only colliding pairs in the other. The results, shown in Figure 4.3, support our reasoning.

4.3.2   *Probability of contact times*

After the validation of our collision detection algorithm, we discuss now the PDF of the contact time τ_c as defined in the beginning of this chapter. We restrict ourselves to $d_c = 2a$, but obviously more general results may be obtained by simple substitution. In the case of particles that are moving with a constant velocity without changing direction, the collision time can be easily related to their relative velocity (see Figure 4.4)

$$\tau_c = \frac{4a \cos \theta}{|\boldsymbol{w}|} = \frac{4aw_r}{|\boldsymbol{w}|^2},$$

where θ is the collision angle.

So the contact time is entirely determined by the relative velocity $\boldsymbol{w}$ at the moment of collision. Therefore we may obtain its PDF with the help of the
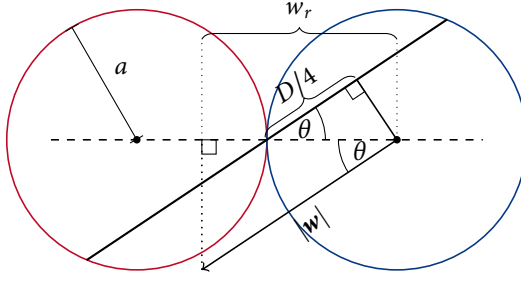
Illustration of the calculation of the contact time τ_c. Two particles moving with a relative velocity w are just about to collide. The thick line passing through the point where both particles touch, gives the distance $D = 4a \cos\theta$ for which both particles will intersect. Dividing this distance by their relative velocity gives the contact time τ_c.

Dirac delta function from Equation (4.7). We start by placing ourselves in a spherical coordinate system

$$p(\tau_c) = \int_0^\infty \int_0^{\pi/2} \int_0^{2\pi} \delta\left(\tau_c - \frac{4a\cos(\theta)}{w}\right)$$

$$\times \frac{w\cos(\theta)}{2^3 \varsigma^4 \pi} \exp\left(-\frac{w^2}{4\varsigma^2}\right) w^2 \sin(\theta)\, \mathrm{d}w\, \mathrm{d}\theta\, \mathrm{d}\phi. \quad (4.9)$$

The Heaviside function from Equation (4.7) has already been evaluated, such that the θ-integration spans only the interval $[0, \pi/2]$. Note also that the index c at the probability itself has been omitted. The integration in θ can be further simplified

$$\int_0^{\pi/2} \delta\left(\tau_c - \frac{4a\cos(\theta)}{w}\right) \cos(\theta)\sin(\theta)\, \mathrm{d}\theta$$

$$= \int_0^1 \delta(\tau_c - \frac{4a}{w}\xi)\xi\, \mathrm{d}\xi = \frac{w}{4a} \int_0^1 \delta\left(\frac{w\tau_c}{4a} - \xi\right)\xi\, \mathrm{d}\xi$$

$$= \begin{cases} \left(\frac{w}{4a}\right)^2 \tau_c & \text{if } w \leq 4a/\tau_c, \\ 0 & \text{else.} \end{cases}$$

Introducing this in Equation (4.9) leads to

$$p(\tau_c) = \frac{\tau_c}{(2\varsigma)^4 (2a)^2} \int_0^{4a/\tau_c} w^5 \exp\left(-\frac{w^2}{4\varsigma^2}\right) \mathrm{d}w,$$

which can be solved by standard techniques

$$p(\tau_c) = \tau_c \left(\frac{\varsigma}{a}\right)^2 \left\{1 - \left[1 + \left(\frac{2a}{\varsigma\tau_c}\right)^2 + \frac{1}{2}\left(\frac{2a}{\varsigma\tau_c}\right)^4\right] \exp\left[-\left(\frac{2a}{\varsigma\tau_c}\right)^2\right]\right\}$$

Finally introducing the dimensionless quantity $\zeta = 2a/(\varsigma\tau_c)$ we obtain

$$p(\tau_c) = 2\frac{\varsigma}{a}\frac{1}{\zeta}\left\{1 - e^{-\zeta^2}\left[1 + \zeta^2 + \frac{1}{2}\zeta^4\right]\right\}. \quad (4.10)$$

Note that Jørgensen et al. (2005) derive a very similar PDF for a slightly different situation.

FIGURE 4.5

The contact time PDF from Equation (4.10), shown here as a thick continuous line. The symbols indicate results from two numerical simulations with different size particles. Furthermore two pointed lines are shown to guide the eye along the limiting behavior for small ($\sim \tau_c$) and large ($\sim \tau_c^{-5}$) contact times.
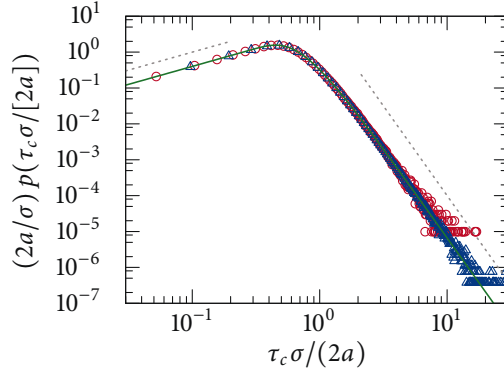
Again we performed numerical analysis. The results shown in Figure 4.5 confirm our derivation. The PDF consists basically of an increasing branch proportional to τ_c for small τ_c to and a rapidly decreasing branch proportional to τ_c^{-5} for large contact times. It peaks at about $\tau_c = 2a/\varsigma$, a value that is small compared to the typical time-step in a numerical simulation.

DIRECT NUMERICAL SIMULATIONS

In the last chapter we described, how collisions are detected given the trajectories of particles. To actually determine these trajectories, we integrated the Maxey–Riley equations (2.16) and (2.17), which in turn necessitates knowledge of the fluid velocity at arbitrary points in space. In this and the coming chapters we present results for which the fluid velocity field was obtained by direct numerical simulation (DNS). Later, in Chapter 8, findings from a different approach, using a simple model for the fluid field, will be shown. Here we start with a summary of our DNS.

5.1 A SHORT INTRODUCTION TO OUR DNS

We obtained the velocity field $\boldsymbol{u}(\boldsymbol{x}, t)$ with the help of a standard pseudo-spectral code. This numerical method makes use of the fast Fourier transform (FFT) to integrate the Navier–Stokes equation (2.2) in Fourier space. We note that one such code has been made publicly available under the GPL by Chumakov (2012) and refer the reader to the introductory book by Boyd (2001) for further information. The code we use was originally developed by Emmanuel Lévêque and Christophe Koudella at the ENS Lyon. It has been used in several publications (e.g., Calzavarini et al. 2009) and was optimized to be especially efficient on the cluster of the PSMN. A periodic cube of 384^3 grid points was used in our simulations with a dealiasing following Orszag's (1971) two-thirds rule, therefore leaving effectively 256^3 modes. The forcing term was chosen to continuously excite a small band of low wavenumbers such that the energy injection rate ε remains constant (Lamorgese et al. 2005). The energy injection rate and the viscosity can be freely chosen and were in our simulations $\varepsilon = 10^{-3}$ and $\nu = 4 \times 10^{-4}$ respectively. These values are given in dimensionless (or rather DNS) units. As explained in Section 2.1.2 one may scale length and time in order to compare our results to different systems with the same Reynolds number. The Taylor scale Reynolds number of our homogenous isotropic turbulent flow is $\mathrm{Re}_\lambda = 130$. In Figure 5.1 the energy spectrum from one of our DNS is shown. It corresponds well to classical experimental data (Comte-Bellot & Corrsin 1971) and is typical for this type of simulation. We finally note that time-stepping was achieved with a second order Adams–Bashforth scheme bearing in mind the Courant–Friedrichs–Lewy condition $\mathrm{Co} = u_{\mathrm{rms}} k_{\mathrm{max}} \Delta t \lesssim 0.1$ (Courant et al. 1928) for the time-step Δt.
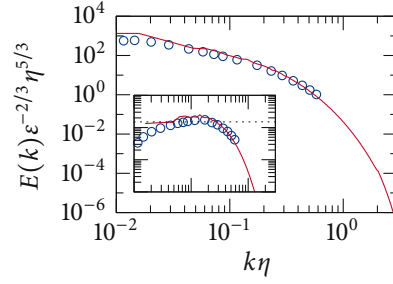
FIGURE 5.1

Typical energy spectrum in our DNS (line) compared to an experimental spectrum (Comte-Bellot & Corrsin 1971, Re_λ = 71.6, symbols). The inset shows the same spectra compensated according to the Kolmogorov scaling, see Equation (2.14), along with the value $C_K = 1.5$ (comp. Sreenivasan 1995).

TABLE 5.1

Characteristic values of the DNS. Given are the energy injection rate ε, the kinematic viscosity ν, the root mean square velocity u_rms, the Taylor scale Reynolds number Re_λ, the Kolmogorov length scale η, the Kolmogorov time τ_K, the longitudinal integral length L_l, and the integral (or large eddy turnover) time T_L.

ε	ν	u_rms	Re_λ	η	τ_K	L_l	T_L
1.0×10^{-3}	4.0×10^{-4}	0.14	130	0.016	0.64	0.97	6.7

Table 5.1 summarizes the values that characterize our DNS. Among these values the longitudinal integral length L_l is given, which is calculated in the DNS according to the Fourier space equivalent of Equation (2.9)

$$L_l = \frac{\pi}{2u_\mathrm{rms}^2} \int k^{-1} E(k) \, \mathrm{d}k \qquad (5.1)$$

(e.g., Batchelor 1953). The large eddy turnover time $T_L = L/u_\mathrm{rms}$ is derived from this value and the root mean square velocity u_rms.

5.1.1 Particle trajectories

Once the DNS had reached a statistically steady state, N_p particles were introduced. We performed several runs with particles of different Stokes numbers, but in each such run, all particles had the same Stokes number. More details about the runs will be given in the next section.

The particle trajectories were integrated by the velocity Verlet algorithm (Press et al. 2007; Swope et al. 1982)—a second order scheme—and the fluid velocity at each particle's exact position was obtained by tri-cubic interpolation. After a transient time of the order of $10 T_L$, all particle positions and velocities were stored at a rate of one per $0.055 \tau_K$, although the actual time-step used in the integration was a factor 10 smaller. This data was then post-processed for all subsequent studies. At first this procedure may seem cumbersome, but it allowed us to adapt our treatment of the data without the additional cost of integrating the trajectories anew.

The above mentioned transient time is necessary, because particles are inserted homogeneously distributed in the fluid and with velocities equal to the fluid velocity. It has however been described before, that inertial
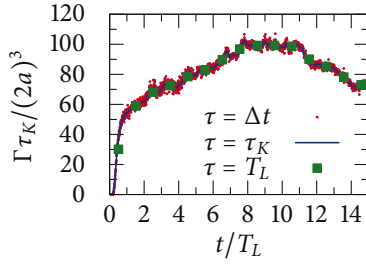
FIGURE 5.2

FIGURE 5.2

The collision kernel Γ during the initial time period. The result is shown for different sampling rates τ, according to Equation (4.2). The initial transient takes at least $5T_L$. In our simulations, we wait for $10T_L$ before recording Γ with a sampling rate of $\tau = T_L$.

particles in a turbulent flow are not homogeneously distributed, but tend to cluster in certain regions. Also, their velocities are different from the fluid velocity. Therefore the freshly introduced particles need a time of the order of a few large eddy turnover times to "find their places" in the flow. This transient time is illustrated by Figure 5.2, which shows the evolution of the instantaneous collision rate during this period.

Due to the very long integration time and a minor neglect in the setup, very few particle trajectories (less than 2 % of the whole population) became deficient after a certain simulation time. As we could deal with this on the level of the collision detection scheme, we decided not to repeat the integration of the trajectories. In the collision detection code, we check, whether any particle runs the risk of becoming deficient. If that is the case, the corresponding particle is replaced, by one additional particle that had not been under consideration for collisions before. The disqualified particle gets then ignored for the rest of the simulation. This approach was easy to implement, because we usually track more (ca. 10 %) particles than are actually considered for collisions. The reasons for this procedure will become clear in Section 6.5.1.

5.2   DESCRIPTION OF THE DIFFERENT RUNS

As mentioned above, several runs were performed at different Stokes numbers (Section 2.3.1). The different runs are summarized in Table 5.2. The number of particles was determined by our choice of the volume fraction $\Phi = N'_p \frac{4}{3}\pi a^3/L_{\text{sys}}^3$, where $L_{\text{sys}} = 2\pi$ in DNS. The volume fraction was typically $\Phi_0 = 4.5 \times 10^{-5}$, except for three cases, where it was $\Phi_0 = 4.5 \times 10^{-6}$. Both values can be considered dilute and effects involving three particles and more can be a priori neglected. In Section 6.5.2 we will discuss a case though, where such effects have a measurable influence. Instead of simply integrating the N'_p particle trajectories necessary to achieve those volume fractions, we integrated an additional 10 % of particles amounting to a total of $N_p = {}^{10}\%\, N'_p$ particles. The reason for this will be explained in Section 6.5.1.

Usually it is assumed in our post-processing, that the density ratio is $\rho_p/\rho_f = 1000$, which corresponds to raindrops in air. But for every Stokes number, one may consider differently sized particles by varying the density ratio. This fact will be used in Chapter 7. In all cases we assured that the

TABLE 5.2
Summary of the basic DNS runs. Given are the Stokes number St, the volume fraction occupied by the particles Φ_0, the total time t_{tot}, for which the trajectories have been integrated after the initial phase of $10T_L$, and finally the total number of collisions detected in the ghost collision approximation N_{GCA}, when assuming a density ratio of $\rho_p/\rho_f = 1000$.

St	0.0	0.10	0.20	0.30	0.51	0.76	1.01
$\Phi_0 \times 10^6$	4.5	4.5	45	4.5	45	45	45
t_{tot}/T_L	15.5	15.5	4.2	31.4	15.9	10.4	47.6
$N_{\text{GCA}}/10^4$	0.6	1.3	29	3.3	200	180	400
St	1.27	1.52	2.03	2.53	3.04	4.05	5.07
$\Phi_0 \times 10^6$	45	45	45	45	45	45	45
t_{tot}/T_L	13.0	52.4	52.1	52.5	52.3	53.1	42.1
$N_{\text{GCA}}/10^4$	81	250	150	99	72	42	22

conditions necessary for the application of the simple form of the Maxey–Riley equations (2.16) and (2.17), namely $a \ll \eta$ and $\rho_f \ll \rho_p$, were fulfilled.

Table 5.2 also lists the special case St = 0, which corresponds to Lagrangian tracer particles, that follow the flow exactly. In principle those particles do have no extent, but it was necessary to assume a finite size, to be able to detect collisions. Therefore in terms of the collision detection algorithm, the radius of these particles was chosen to be the same as for particles with St = 0.1.

5.3   VERIFICATION OF RESULTS

The DNS code described above has been used in various scientific publications. It has been validated many times, and its results have been demonstrated to be correct. The post-processing code however, that does the collision detection and all particle statistics, has been written for this purpose and needs proper checking. To this end we will compare different exemplary results to published data. We start with the RDF.

5.3.1   *Radial distribution function*

Since Sundaram & Collins (1997) first used it to study particle collisions, many studies have been devoted to a precise determination of the RDF. In one of the earlier extensive publications, Reade & Collins (2000) give the functional form

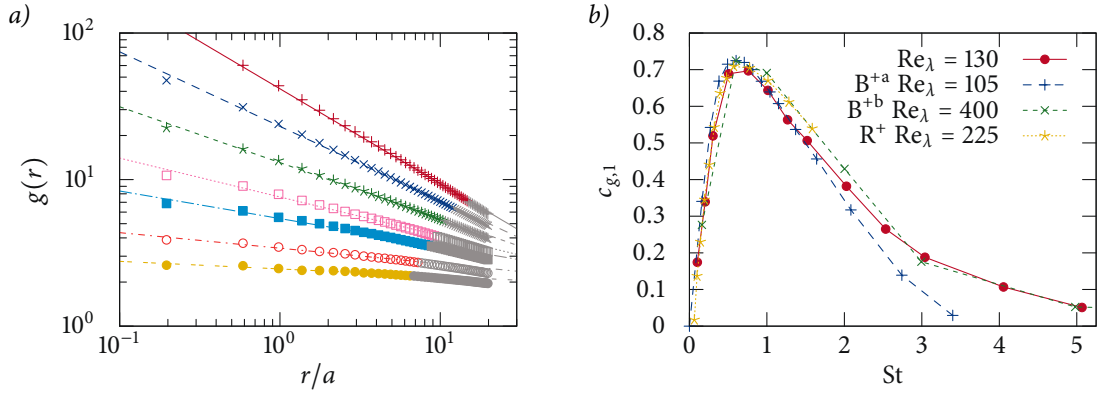$$g(r) = c'_{g,0}(r/\eta)^{-c'_{g,1}} \exp\left(-c'_{g,2}(r/\eta)\right) + 1,$$

FIGURE 5.3

(a) The RDF for, from top to bottom, St = 1.0, 1.5, 2.0, 2.5, 3.0, 4.0, 5.0. Smaller Stokes numbers were omitted, because the slopes do not behave monotonically in the whole range (comp. Figure 5.3b). Additionally to the numerical results (symbols), power law fits according to Equation (5.2) (lines) are shown. This law holds only true for $r < \eta$; larger values are grayed out in the plot. *(b)* The power law coefficient $c_{g,1}$ as defined in Equation (5.2) from our DNS in comparison to other published results. Shown is data from Bec et al. (2007, B^{+a}), Bec et al. (2010, B^{+b}), and Rosa et al. (2013, R^+).

which gives the correct asymptotic behavior for large distances r. Most recent studies however content themselves with the simpler functional form, which holds for $r/\eta \ll 1$

$$g(r) = c_{g,0}(r/\eta)^{-c_{g,1}} \tag{5.2}$$

and so do we. Results of our DNS and fits according to Equation (5.2) are shown in Figure 5.3a.

As pointed out by Bec et al. (2005), the latter formulation of the RDF in Equation (5.2) stands in close relation to the correlation dimension $\mathcal{D}_2$ known from dynamical systems theory (Grassberger & Procaccia 1983). This allows us to compare our results to those in Bec et al. (2010, 2007) by the simple transformation $c_{g,1} = 3 - \mathcal{D}_2$. The comparison is shown in Figure 5.3b, where we also show data from Rosa et al. (2013). Our results are in good correspondence with the published data.

As explained in Section 3.2.4, sole the value of the RDF at the collision radius, $g(2a)$, enters in the kinematic determination of the collision rate. In Figure 5.4a we compare our results again to data from Rosa et al. (2013) and, in addition, from Woittiez et al. (2009). We find a good agreement, although the results of Woittiez et al. (2009) are smaller than ours.

5.3.2 *Radial relative velocity*

Next, we want to check our results for the RRV, which presents the second ingredient of the kinematic formulation of the collision kernel. In this case we determine the mean value directly without passing by the PDF. The latter could again be fit similarly to Equation (5.2) (see Rosa et al. 2013).
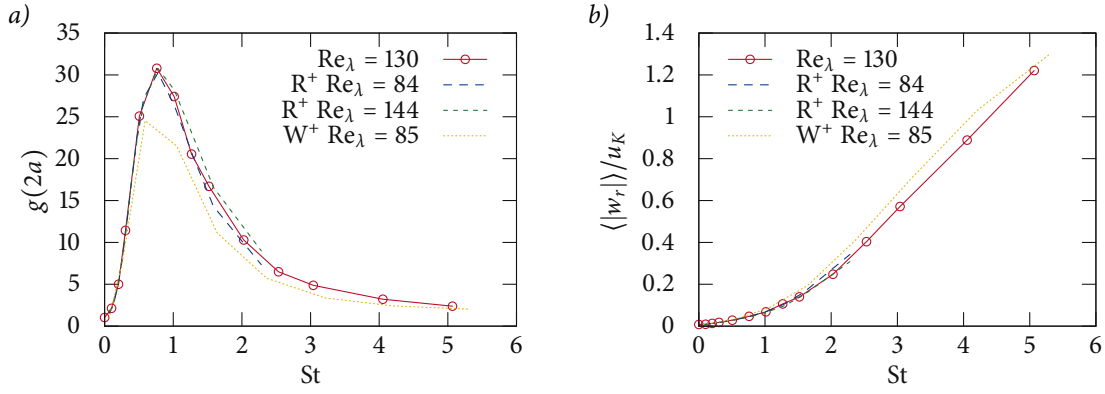
a)

b)

FIGURE 5.4

(a) The RDF at the collision radius $g(2a)$. (b) The RRV $\langle|w_r|\rangle$ normalized by the Kolmogorov velocity u_K for different Stokes numbers. Alongside our data (symbols), we show data from Rosa et al. (2013, R^+) and Woittiez et al. (2009, W^+) for comparison.
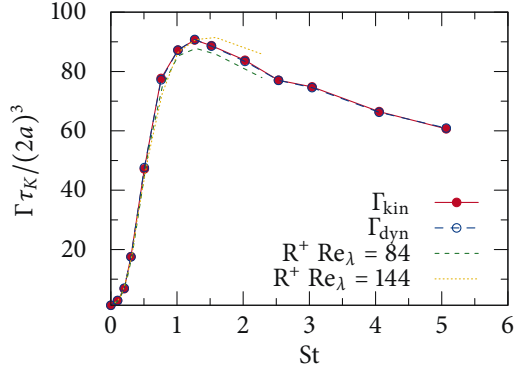
FIGURE 5.5

Comparison of the dynamic and kinematic collision kernels determined within the GCA. This provides a cross-check between our collision detection scheme and the evaluation of $\langle|w_r|\rangle$ and $g(2a)$. Also shown is data from Rosa et al. (2013, R^+).

We content ourselves however with comparing the mean value $\langle|w_r|\rangle$ to published data, again from Rosa et al. (2013) and Woittiez et al. (2009), in Figure 5.4b. In this case the values from Woittiez et al. (2009) lie above ours, but the correspondence with the results from Rosa et al. (2013) is very good.

5.3.3 Dynamic and Kinematic Collision kernel

Finally, to verify our collision detection scheme, we compare in Figure 5.5 the kinematic and the dynamic collision kernel. Up to a tiny uncertainty, the two ways of determining the collision kernel, give the same result. Also the comparison to the results of Rosa et al. (2013) displays no problems.

We conclude thus, that our post-processing gives the correct results and we proceed with the main scientific questions treated in this thesis.

MULTIPLE COLLISIONS AND SHORTCOMINGS OF THE GHOST COLLISION APPROXIMATION

Section 3.2.6 introduced the ghost collision approximation (GCA), which consists in counting every collision between a given pair of particles as a new collision, even though the pair may have already collided before. In this chapter we quantify the error, which this simplification introduces in the estimation of the collision kernel. This error will be related to multiple collisions between a same pair of particles, which in turn is closely related to a tendency of particles to stay in proximity for long times. We will present the contact time, which has been introduced in Section 4.3, for inertial particles in turbulent flows. Finally, different alternative algorithms will be discussed.

6.1 GHOST COLLISION AND FIRST COLLISION KERNEL

We introduce Γ_{GCA}, the collision kernel obtained by using the GCA. The rate Γ_{GCA} can be compared to Γ_1, which counts only the first collisions occurring between a given pair of particles. The definition of Γ_1 can be generalized in a straightforward manner to Γ_{N_c}, which counts the number of times that a particle collides for the N_c-th time. To determine Γ_{N_c}, we store for every pair the number of collisions it has undergone with each other. If a new collision of that pair is detected, the corresponding number of collisions of this pair is incremented as well as the number of collisions used to determine the corresponding Γ_{N_c}.

The rates Γ_{N_c} in fact allow us to decompose Γ_{GCA} systematically as

$$\Gamma_{\mathrm{GCA}} = \sum_{N_c=1}^{\infty} \Gamma_{N_c}.$$

We argue, that in a system, where particles react upon their first contact, e.g., a cloud where droplets coalesce (assuming unity efficiency), the collision kernel of first contacts, Γ_1, is a more appropriate estimate for the "real" collision kernel. Our arguments will be presented in more detail in Section 6.5. With these definitions, one obtains that

$$\Gamma_{\mathrm{GCA}} = \Gamma_1 + \Gamma_m, \qquad\qquad \Gamma_m = \sum_{N_c=2}^{\infty} \Gamma_{N_c}. \qquad (6.1)$$

Figure 6.1a shows the ghost collision kernel, Γ_{GCA}, and compares it with the value of Γ_1. Clearly, Γ_{GCA} overestimates the real collision kernel, the difference being due to the multiple collisions collected in Γ_m. To quantify the error introduced by the GCA, Figure 6.1b shows the ratio Γ_m/Γ_1 for a range of Stokes numbers. It shows that the GCA overestimates the collision
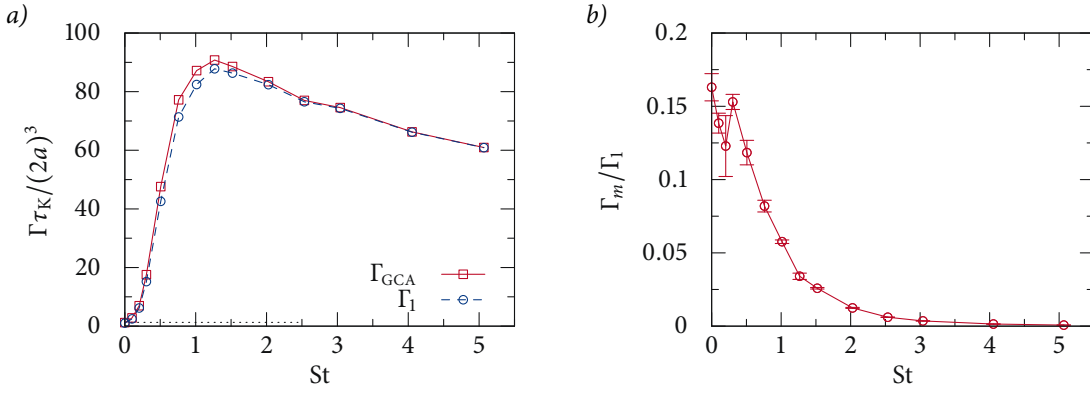
(*a*) The collision kernel as obtained in the GCA in comparison to the collision kernel of first collisions. The dotted line on the bottom gives the value expected for St → 0 according to the Saffman–Turner theory (Section 3.2.2). (*b*) Ratio of the multiple collision kernel Γ_m, representing the spurious contribution of Γ_{GCA}, and Γ_1.

kernel by more than 15 % for small Stokes numbers. The error diminishes when Stokes increases, and seems to tend to zero for large values of the Stokes number. Gustavsson & Mehlig (2013a) confirm this behavior for a random flow model.

For particles without inertia (St = 0) errors of comparable magnitude have been reported by Wang et al. (1998a) and in a slightly different setup by Brunk et al. (1998b), see in particular their Fig. 4. Andersson et al. (2007) predict *first* collisions of particles advected in Gaussian random flows. The collision rate in the GCA corresponds to what they call the "initial transient". Andersson et al. (2007) provide numerical results for a three-dimensional Gaussian random flow at small Kubo number.[1] In this limit, they find a ratio that corresponds to $\Gamma_m/\Gamma_1 \approx 5$ (comp. Fig. 1*b* in Andersson et al. 2007). This is much larger than what we find in our DNS, but in their system the Kubo number is only Ku = 0.04. For Ku = 1, Gustavsson & Mehlig (2013a) find in a similar but two-dimensional model $\Gamma_m/\Gamma_1 \approx 0.6$ (see their Fig. 1*a*). This is already closer to our findings. It would be very interesting to check this model in three dimensions and at Ku = 1.

6.2   MULTIPLE COLLISION PDF

The results from Figure 6.1 demonstrate that multiple collisions between a given pair of particles play a significant role in the estimates obtained with

---

[1] The Kubo number Ku is often used in plasma physics and diffusion processes. It compares the length a particle travels during the correlation time of the flow $u_{rms}\tau_{cor}$ with the correlation length of the flow ℓ_{cor} (e.g., Bakunin 2008)

$$Ku = \frac{u_{rms}\tau_{cor}}{\ell_{cor}}.$$

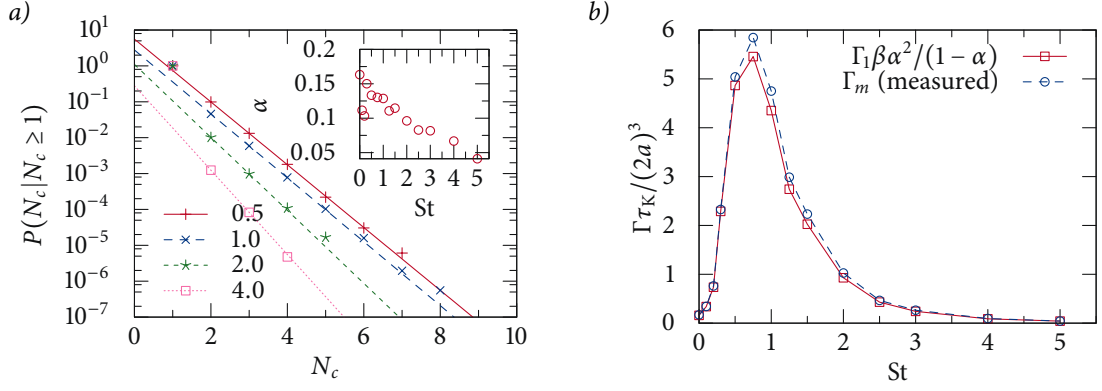In turbulent flows Ku is typically of order unity (Wilkinson et al. 2006).

FIGURE 6.2

(*a*) The conditional PDF for a pair to undergo N_c collisions after one initial collision. The data (symbols) is fitted very well by Equation (6.2) (lines). One of the corresponding fit parameters, α, is shown in the inset. (*b*) Verification of Equation (6.3).

the GCA. To further describe this effect, we introduce the PDF for a pair to undergo N_c collisions with each other, conditioned on the fact, that the pair collides at least once. This PDF $P(N_c|N_c \geq 1)$ is shown in Figure 6.2*a* and interestingly obeys a law

$$P(N_c|N_c \geq 1) = \beta \alpha^{N_c}, \tag{6.2}$$

for $N_c \geq 2$. This result can be interpreted in a Markovian sense: After a pair has collided at least two times, it has a probability $(1 - \alpha)$ to separate and not collide again, and a probability α to undergo more collisions. Together with our data Figure 6.2*a* shows fits according to Equation (6.2) and the corresponding fit parameter α. The probability varies with the Stokes number, such that multiple collisions are less probable for particles with larger Stokes numbers. This agrees with the findings of the last section, where it was found that the spurious effect of the GCA diminishes with growing St.

Combining Equations (6.1) and (6.2), we may re-express the collision rate of multiple collisions

$$\Gamma_m = \Gamma_1 \sum_{N_c=2}^{\infty} \beta \alpha^{N_c} = \Gamma_1 \frac{\beta \alpha^2}{1 - \alpha}. \tag{6.3}$$

As a test for consistency, we present in Figure 6.2*b* a comparison between Equation (6.3) and the numerical results for Γ_m. The difference between the two is less than 10 %.

6.2.1 *An example of a trajectory displaying multiple collisions*

Aside the striking functional form of $P(N_c|N_c \geq 1)$, Figure 6.2*a* reveals another astonishing feature. Even for particles with a relatively strong inertia, e.g., St = 1, we find cases, where a same pair collides eight times. Figure 6.3 illustrates the difference between pairs of particles that experience either
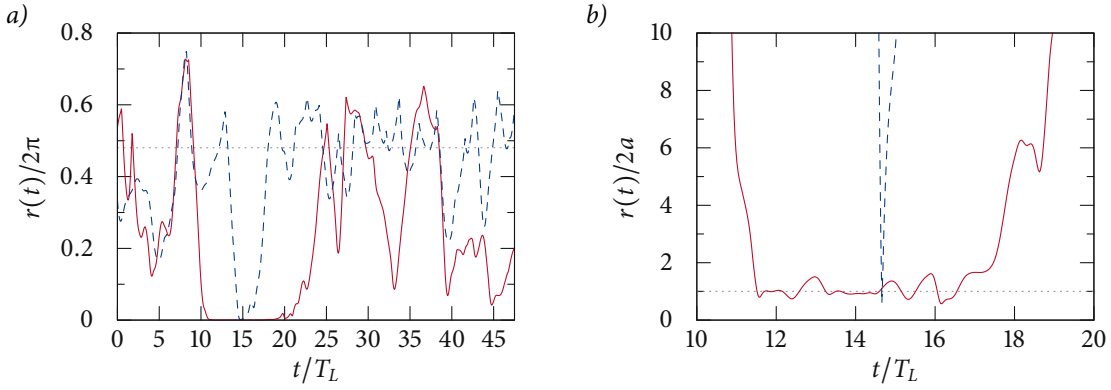
FIGURE 6.3

The distance between two different pairs of particles over the course of time, both with St = 1. The distance for the one pair is given as full lines, the distance for the other as dashed lines. Panel (*a)* shows the entire runtime of the simulation and the distance in units of the box size 2π. The dotted line gives the expected average distance for a pair in a periodic cube. In (*b*) a zoom of the data is shown. Here the distance is given in units of the collision radius, which is also highlighted by a dotted line. In both cases the time is given in units of the large eddy turnover time.

only one collision, or many collisions. It shows the distance $r(t)$ between two particles. The dashed lines correspond to a pair of particles that collides only once, and separates right after this collision. The full lines correspond, on the contrary, to a pair of particles that stays in proximity after an initial collision. The distance $r(t)$ fluctuates around the collision radius of $2a$, thus causing several events which are interpreted as different collisions when using the GCA. Overall, this pair stays closer than $4a$ for a time of $6T_L$, whereas the contact time of the other pair is orders of magnitude smaller. This observation motivates the investigation of the contact time presented in the next section.

The fact that particles in turbulent flows may stay close for relatively long times has been noted before, for example by Jullien et al. (1999), Rast & Pinton (2011), or Scatamacchia et al. (2012). But up to now, this feature was mostly documented for Lagrangian tracer particles. The trajectories in Figure 6.3 are from particles with St = 1. Thus here we report on the novel fact, that also inertial particles may exhibit this feature.

6.3   CONTACT TIME STATISTICS

The contact time τ_c has been introduced in Section 4.3 for ideal gas particles with only one consecutive collision in mind. Figure 6.3 shows however, that the situation for particles in a turbulent flow is more complicated. We therefore refine the definition of the contact time as illustrated in Figure 6.4. With these definitions, we can for example express the contact time during an i-th collision as $\tau_{c,i} = t_{s,1} - t_{e,1}$. Similarly the time between two consecutive encounters can be expressed as $t_{e,i+1} - t_{e,i}$.
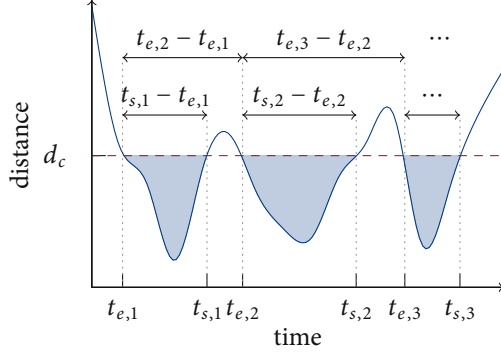
FIGURE 6.4

Illustration of our definition of the different "contact" times. Shown is the distance between a pair of particles over time. When it falls below some value d_c for the i-th time, we term this an encounter and name the corresponding moment $t_{e,i}$. We proceed correspondingly with the times, when the particles separate, and name them $t_{s,i}$. From these definitions different time intervals, like the contact time $\tau_{c,i} = t_{s,1} - t_{e,1}$ can be derived.
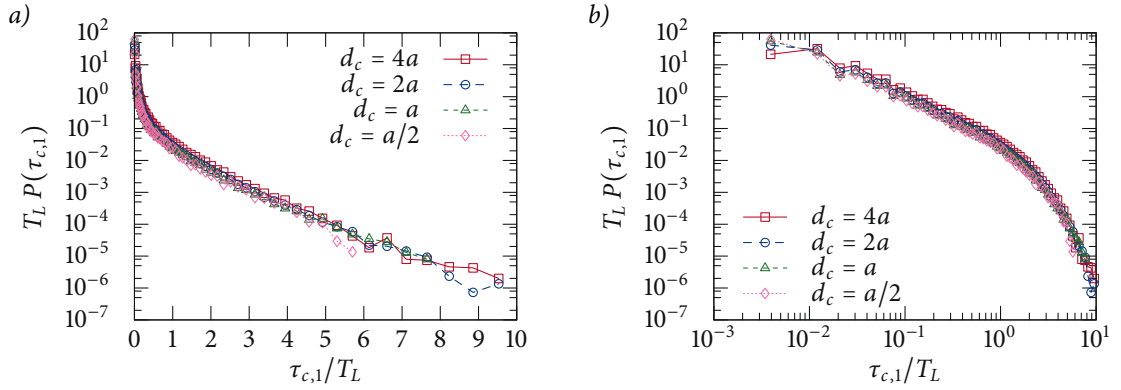

FIGURE 6.5

The PDF of the first contact time for different critical distances in semi-logarithmic (*a*) and doubly-logarithmic (*b*) scaling.

We have seen that the contact times may be relatively large, therefore we express them in terms of the large eddy turnover time. Another plausible choice could be the inverse of the dominant Lyapunov exponent of the particles (Bec et al. 2006). These two time scales are very similar for the Reynolds number considered here. Deciding which is the proper time scale would require simulations at different Reynolds number, which were not performed in the realm of this work.

Figure 6.5 shows the PDF of the first contact time $\tau_{c,1}$, which we have determined for different values of the critical distance d_c. In the investigated range with $d_c \ll \eta$, the results depend only very slightly on this parameter, which will be set to $d_c = 2a$ in the following.

The data shown in Figure 6.5 was obtained for particles with St = 1.5 (the Stokes number dependence will be discussed later). As it was the case for the ideal gas particles, see Figure 4.5, the PDFs exhibit a power law behavior for a range of values of $\tau_{c,1}$. The constraint that the PDF has to be normalizable imposes that the scaling law cannot extend all the way to $\tau_{c,1} = 0$ when the exponent is larger than 1. We suspect that the functional form changes again for very small times, as was the case for the ideal gas
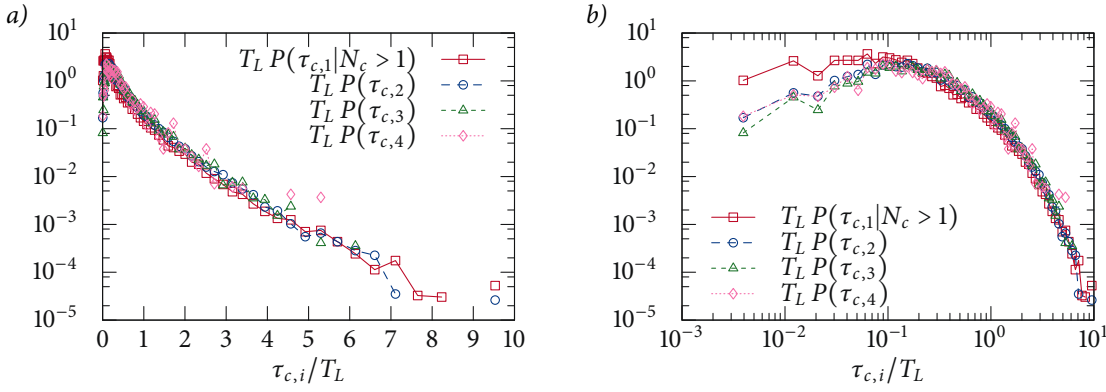
FIGURE 6.6

The PDFs for the second, third, and fourth contact time, as well as the PDF for the first contact time conditioned on the fact, that the same pair will collide at least one further time. The data is shown in both semi-logarithmic (a) and doubly-logarithmic (b) scaling. The Stokes number is St = 1.5.

particles (comp. Section 4.3.2). We do however not resolve such small times in our DNS.

Contrary to the results obtained for the ideal gas, the PDFs in Figure 6.5 display exponential tails at long contact times, revealing a finite probability for particles to stay close for several large eddy turnover times. This feature seems to be related to the phenomenon of multiple collisions. Further evidence for this conclusion comes from Figure 6.6, which shows the contact time probabilities for second and higher collisions. Here the power law behavior vanishes. This behavior was interpreted as being related to ideal gas particles—that is particles, which collide once and separate right afterward. The fact that it disappears for multiple collisions confirms our interpretation. The exponential tails for long contact times however rest, confirming again the interpretation, that those are related to multiple collisions.

A further interesting conclusion from Figure 6.6 is, that also for the first contact time PDF, the power law vanishes, if it is conditioned on having further collisions after the initial one. Remarkably, this conditional PDF is very similar to the PDFs of higher contact times. Figure 6.7 further illustrates this phenomenon, by comparing the usual first contact time PDF to two conditional PDFs: Once conditioned on having one unique contact, the other time conditioned on having multiple contacts.

We go on by presenting the PDF of time in between collisions in Figure 6.8. Evidently, the typical timescales become larger, i.e., the PDFs get shifted to the right with respect to the contact time PDFs presented up to this point. Even the cutoff at small times gets resolved in this case. There is however no power law for intermediate times, which is in accordance with our interpretation, that it is related to ideal gas like collisions. The exponential tails remain.
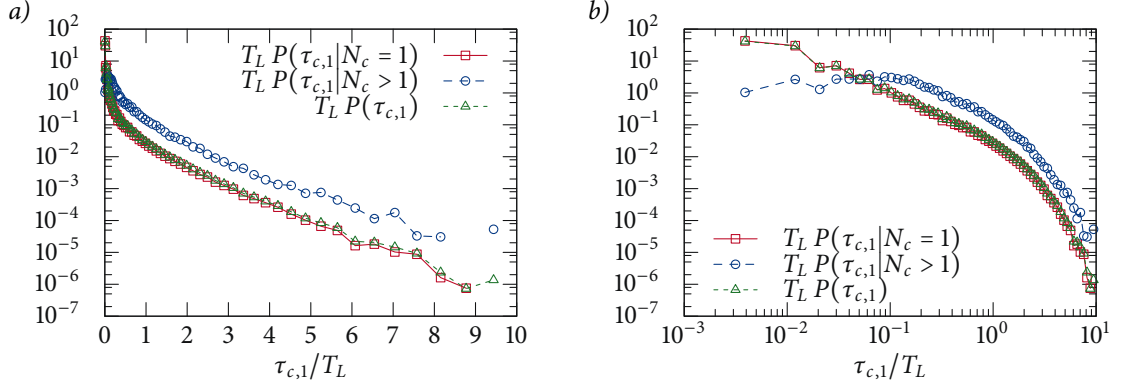
FIGURE 6.7

The first contact time PDF for St = 1.5, as well as the same PDF conditioned on two different facts. One time, that pairs will collide only once, $P(\tau_{c,1}|N_c = 1)$. The other time, that pairs collide several times, $P(\tau_{c,1}|N_c > 1)$. Again the data is shown in semi-logarithmic (*a*) as well as doubly-logarithmic (*b*) scaling.
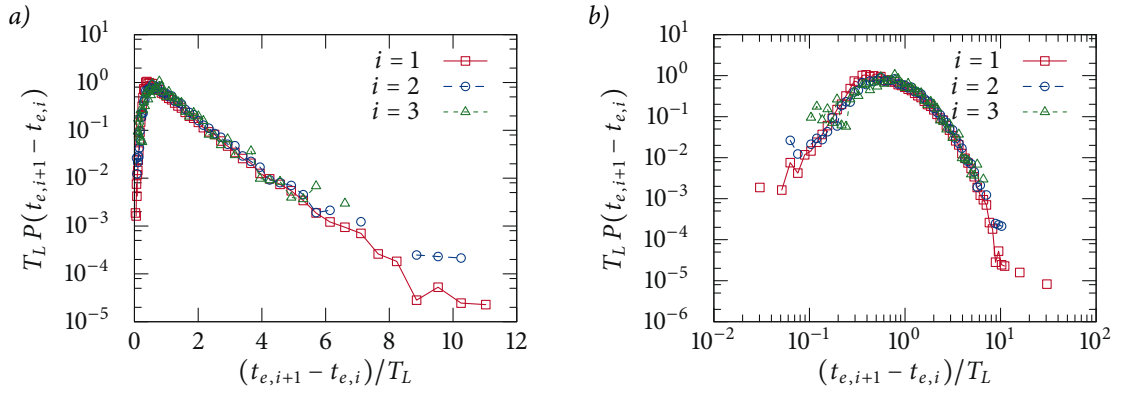

FIGURE 6.8

PDFs of the time between contacts for the first and second, second and third, as well as for the third and fourth contacts. The data is for St = 1.5 and shown in semi-logarithmic (*a*) and doubly-logarithmic (*b*) scaling.
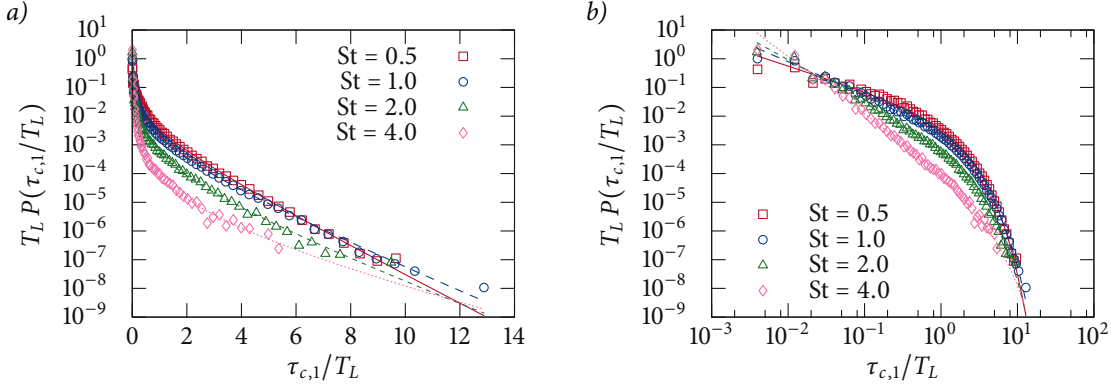
The first contact time PDF for different Stokes numbers as indicated in the legend. Alongside the data (symbols) fits according to Equation (6.4) (lines) are shown. The data is given in semi-logarithmic (*a*) and doubly-logarithmic (*b*) scaling.

6.3.1 *Dependence on the Stokes number*

Up to here, all shown contact time PDFs were for the case St = 1.5. Figure 6.9 shows the first contact time PDF for different Stokes numbers. The qualitative appearance does not change. But the overall probability for long contact times decreases with increasing St, whereas the range of the power law extends and its slope steepens. We find that all these PDFs can be fitted by

$$P(\tau_{c,1}) \sim (\tau_{c,1}/T_L)^{-\xi} \exp\left(-\kappa \tau_{c,1}/T_L\right), \qquad (6.4)$$

where the omitted proportionality constant is determined by the correct normalization. The lines in Figure 6.9 show fits of this form. They all work very well, but the quality of the fits degrades for St < 0.3 (not shown).

The two fit parameters κ and ξ are shown in Figure 6.10 as a function of the Stokes number. As noted before, the slope of the power law conveyed by the parameter ξ steepens and one may suspect that it reaches $\xi = 5$ for St $\to \infty$ according to our findings for the ideal gas particles in Section 4.3.2. The exponential law seems to vanish.

6.4 RELATION TO SLING/CAUSTICS COLLISIONS

In Equation (3.15) a decomposition of the collision kernel into one contribution from shear induced collisions, and another one from sling/caustics collisions, was proposed. It is interesting to ask, whether the multiple collisions we report on in this chapter, belong mainly to one of these two groups. An evident assumption is, that multiple collisions are mainly due to shearing motion. Sling/caustics collisions happen between particles originating from different regions of phase space, at large RRV. It is probable that those particles will continue their trajectories after the collision and separate quickly without further collisions. This reasoning is confirmed by the results shown
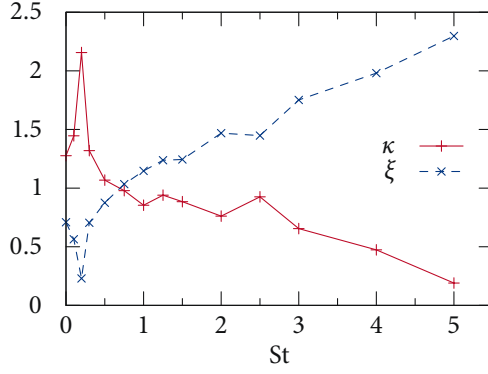
FIGURE 6.10

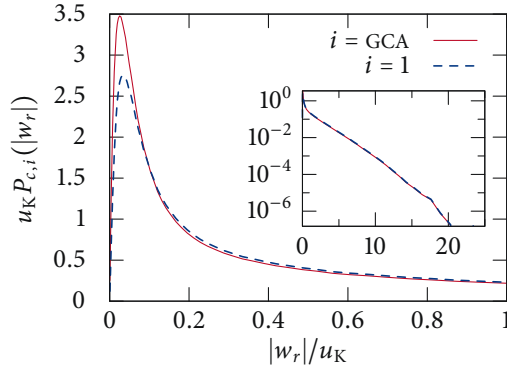The fit coefficients according to Equation (6.4) for our data.

FIGURE 6.11

The PDF of the RRV obtained for all colliding particles as in the GCA (full lines) and for only first collisions (dashed line). The inset shows the same PDFs in a wider range and in semi-logarithmic scaling. These results are for St = 1.0.

in Figure 6.11, which shows the PDF of the absolute value of the RRV. This PDF was obtained once, taking into account all collisions, as in the GCA, and another time, taking into account only first collisions. Both PDFs are sharply peaked at low RRV and have exponential tails. A close comparison however reveals, that the PDF for first collisions lies below the other PDF for small RRV and above it for larger RRV. As the difference between the two PDFs must be attributed to multiple collisions, on may therefore conclude, that multiple collisions happen at small RRV. A strong evidence for this conclusion is provided by Figure 6.12. There the ratio of the mean RRV of first collisions, $\langle |w_r| \rangle_{c,1}$, and the mean RRV of all collisions, $\langle |w_r| \rangle_{c,\mathrm{GCA}}$, is shown. At small values of the Stokes number, the mean RRV of first collisions is larger, hinting again that multiple collisions have on average small RRV. At larger Stokes numbers the difference between the first collision kernel Γ_1 and the ghost collision kernel Γ_{GCA} vanishes and so does the difference in the mean RRVs.

The inset of Figure 6.12 shows the mean RRV for only multiple collisions, in comparison to the mean RRV of first collisions. The value for multiple collisions is much smaller than the one for first collisions. The assumption, that multiple collision are not due to sling/caustics collisions, which happen at large RRV, but rather due to shear induced collisions is therefore fully consistent with our numerical results.
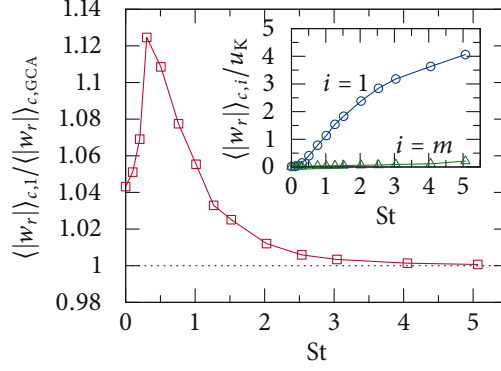
The ratio of the mean values of the RRV in the GCA and for only first collisions as a function of the Stokes number. In the inset the mean values are shown for only first collisions (circles) and for all multiple collisions (triangles) in units of the Kolmogorov velocity u_K.

6.5 ALTERNATIVE ALGORITHMS

In the introduction to this chapter it has been argued, that the collision kernel, for which only first collisions were taken into account, was a more realistic estimate than the collision kernel obtained in the GCA. This argumentation was based on a system, where particles react upon their first collision. To be more precise one should define, what kind of reaction the particles undergo. Krstulovic et al. (2013) investigate a system, where the unique species of particles Λ reacts with each other by disappearing, or in other terms $\Lambda + \Lambda = \varnothing$. In this case Γ_1 is certainly a better estimate, but it is not clear, if it is the correct estimate. In such a system it is not only impossible that a pair collides with each other a second time. Actually each of the particles is not allowed to collide with *any* further particle after an initial collision. To investigate such a system, we propose to mimic it with the help of the algorithm described in the following section.

6.5.1 *Replacement algorithm*

It has been mentioned before that we usually integrate a total of N_p' particles in our simulations. Nevertheless, we restrict ourselves to a subset of N_p particles to check for collisions. Therefore we may, at each collision, replace the two colliding particles by two of the additional $N_p' - N_p$ particles. Replacing the particles instead of just "deleting" them, has the advantage, that the system stays in a stationary state with respect to the number of particles N_p. We will refer to this algorithm, that replaces both colliding particles, as R2 and to the corresponding collision kernel as Γ_{R2}.

A second similar algorithm consists in replacing only *one* arbitrarily chosen particle of each colliding pair. We will refer to this algorithm and the corresponding collision kernel as R1 and Γ_{R1} respectively. This algorithm could be seen as representing a system, where the particles react such that $\Lambda + \Lambda = \Lambda$. Of course one would need to take into account other effects like momentum conservation in a more realistic model.
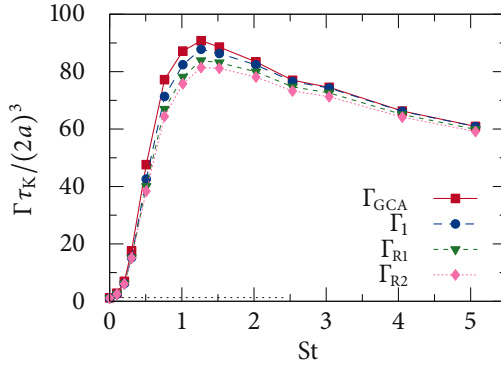
FIGURE 6.13
Here the same data as in Figure 6.1a is shown. Additionally the collision kernels Γ_{R1} and Γ_{R2} that were obtained with the replacement algorithm described in Section 6.5.1 are shown.

We finally note that for tracer particles, it is not necessary to integrate additional trajectories. In this case two new particles may be placed randomly in the flow and their velocities are fully determined by the fluid velocity field at that instant. For inertial particles however, the momentary velocity depends on their history and therefore it is necessary to keep the additional particles in the flow. Wang et al. (1998a) investigated such an algorithm and their results are in accordance with ours. In a companion paper Zhou et al. (1998) investigate particles with finite inertia. There, they use a further algorithm. They simply remove all colliding particles and take the diminishing number of particles into account when calculating the collision kernel.

6.5.2 Dynamic collision kernel with the alternative algorithms

We have implemented the alternative algorithms described in the last section and calculated the corresponding collision kernels. Our results are shown in Figure 6.13. As expected, we find that the results obtained with the new algorithms R1 and R2 lie below those obtained within the GCA. However, they lie even below the collision kernel for only first collisions, which seems puzzling at first. Before explaining the observed difference between Γ_1 and Γ_{Ri}, $i = 1, 2$, we note that also Γ_{R1} and Γ_{R2} differ from each other. When we replace both colliding particles, fewer collisions take place.

To explain the difference between the different algorithms, consider the following situation: Two groups ("jets") of particles, originating from different regions in phase space, are brought into proximity by the sling/caustics effect. In the GCA, as the two jets cross each other, any one particle from one group, may collide with several other particles from the other group. The same is true, of course, for any particle with which that particle collided. Now in this special case, Γ_1 and Γ_{GCA} would not differ at all, because none of the multiple collisions that any particle undergoes takes place with a particle it collided with before. The collision kernels obtained in the two new algorithms however will differ from Γ_{GCA}. With the algorithm R1 only one of the colliding pairs has the chance to collide with further particles, explaining, why Γ_{R1} is smaller than Γ_1. The other algorithm, R2, replaces both
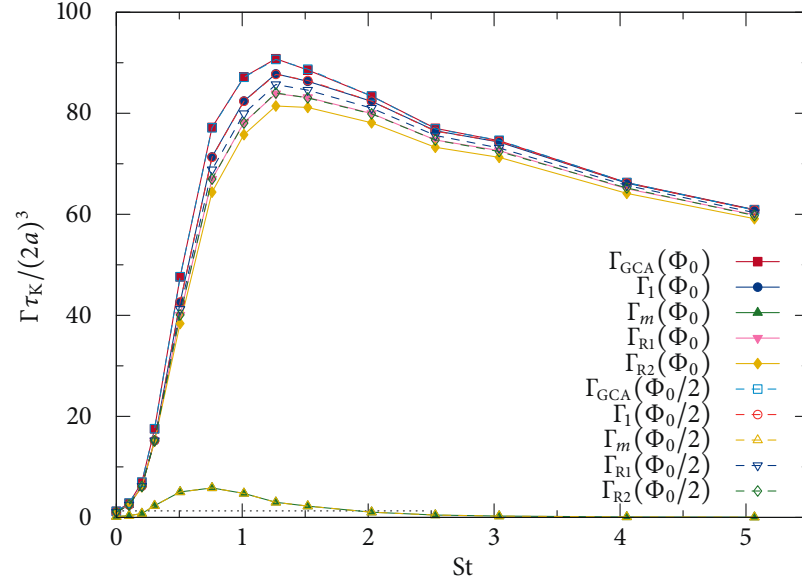
FIGURE 6.14

The collision kernel obtained in the GCA, Γ_{GCA}; the collision kernel for only first collisions, Γ_1; the collision kernel for only multiple collisions, $\Gamma_m = \Gamma_{\text{GCA}} - \Gamma_1$; and the collision kernels for the replacement algorithms introduced in Section 6.5.1, Γ_{R1} and Γ_{R2}. All these collision kernels are shown for two different volume fractions, once for Φ_0 as given in Table 5.2 and once for half that value. As in Figure 6.1a, the dashed line represents the expected result for Γ_{GCA}, when $\text{St} \to 0$.

colliding partners, therefore none of them will participate in any further collisions. That is why Γ_{R2} is even smaller than Γ_{R1}.

The above interpretation relies on some very particular hypothetical assumption, namely that there are events in a turbulent flow, where jets of particles collide with each other. The assumption used here suggests in fact that the algorithms R1 and R2 affect the number of collisions, insofar as groups of three particles (or more) are concerned; namely the two particles that initially collide and at least one other particle. If this is the case, the obtained collision kernel should depend on the number density n of the particles. Remember, that the rate of collisions is proportional to n^2. This proportionality is broken, if we suppress some collisions with a rate proportional to n^3. Therefore the collision kernel, which was defined as precisely the proportionality constant joining the rate of collisions and n^2, will depend on n.

To check our reasoning we performed the same analysis, that led to the results shown in Figure 6.13, for half the number density as before. In other terms, we reduced the number of particles considered in the collision detection scheme by a factor of two, resulting in a halved volume fraction $\Phi_0/2$. The results are shown in Figure 6.14. First of all, one notices, that as expected neither Γ_{GCA}, nor Γ_1, nor Γ_m depend on the volume fraction Φ. The collision
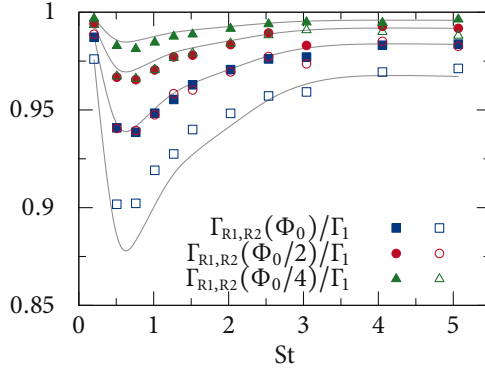
FIGURE 6.15

The ratios Γ_{Ri}/Γ_1, $i = 1, 2$ for three different volume fractions and for different Stokes numbers are represented by symbols as indicated in the legend. We excluded the two points, where according to Table 5.2 Φ_0 is smaller than for the rest. The full lines are meant as a guide for the eye. They are chosen, such that the distance between these curves and 1 falls by a factor of two for the next higher line.

kernels obtained with the alternative algorithms, Γ_{R1} and Γ_{R2}, however do change, when we vary Φ. This is in accordance with our reasoning.

Interestingly, looking closely one realizes, that the collision kernel obtained by replacing both particles coincides with the collision kernel obtained by replacing only one particle at double the volume fraction. This observation as well is in accordance with the above argumentation, that the discrepancy between the Γ_{Ri}, $i = 1, 2$, and Γ_1 stems from effects involving three and more particles. In fact, according to our reasoning, the difference $\Gamma_1 - \Gamma_{Ri}$, $i = 1, 2$, should be to leading order linear in n and therefore in Φ. This is investigated in more detail in Figure 6.15, which shows the ratios Γ_{Ri}/Γ_1, $i = 1, 2$ for three different volume fractions all within a factor two of each other. We empirically find the two rules

$$\Gamma_{R2}(\Phi/2) = \Gamma_{R1}(\Phi) \qquad \text{and} \qquad \Gamma_{Ri} - \Gamma_1 \sim \Phi \quad \text{for } i = 1, 2. \qquad (6.5)$$

The latter seems to be only approximately valid, but both confirm our argumentation.

To make our explanation more clear, let us present it once more, but from another perspective. We try to explain, why Γ_{R1} and Γ_{R2} are smaller than Γ_1 and why the former two vary with the volume fraction Φ. To this end, let us follow a particle along its trajectory. The rate of collision along this trajectory $\mathcal{R}$ as been introduced in Section 3.2.2. It is proportional to n, and therefore to Φ, namely $\mathcal{R} = \Gamma n$. This is exactly true for collisions in the GCA, but also when counting only first collisions. The two alternative algorithms introduced in Section 6.5 however necessitate a correction. When the particle we follow collides, the algorithm R2 changes its position and its (former) surroundings, by replacing also the colliding partner. The algorithm R1 changes only one of these, either the surroundings, or the position of the particle. Both approaches certainly prevent any further collisions between the two colliding particles. But they also suppress collisions between the test particle and a third particle, at least for the time, the flow needs to reorganize after the "perturbation" of replacing one or two particles. During this time, which we shall call τ_R, a part of the collisions, which would take place at a rate $\mathcal{R}$, are suppressed. With respect to the collision kernel, that counts
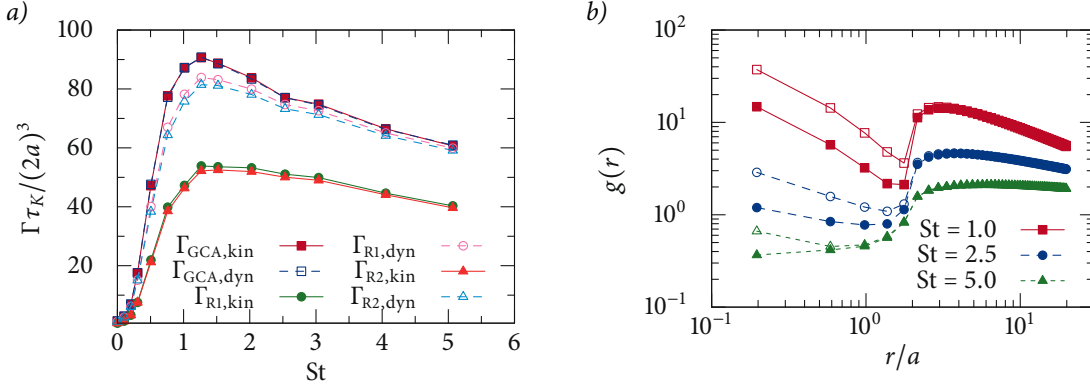
FIGURE 6.16
(a) The kinematic and dynamic collision kernel for the three different algorithms, GCA, R1, and R2. *(b)* The RDF for the two replacement algorithms R1 (filled symbols) and R2 (open symbols).

only first collisions, we therefore expect a correction of the order of $\mathcal{R}\tau_R$, or more precisely

$$\Gamma_{Ri} = \Gamma_1 \left[1 - \mathcal{O}(i\mathcal{R}\tau_R) \right]. \tag{6.6}$$

As mentioned above, the rate $\mathcal{R}$ is proportional to Φ and therefore Equation (6.6) fulfills the two empirically found laws (6.5).

The above explanation of the discrepancy between the collision kernel Γ_1 and the two collision kernels obtained with the alternative algorithm, Γ_{R1} and Γ_{R2}, implies that this difference is proportional to the volume fraction Φ. As a consequence, the discrepancy must vanish in the very dilute limit, i.e., $\Phi \to 0$. Therefore, in this limit the two algorithms R1 and R2 give the correct result.

6.5.3   *Kinematic collision kernel with the alternative algorithms*

One disadvantage of the replacement algorithm is illustrated by Figure 6.16*a*. The collision kernel cannot be determined kinematically, that is with the help of Equation (3.14), anymore. For the GCA, the dynamic collision kernel, determined by counting collisions, and the kinematic kernel coincide. For both alternative algorithms, R1 and R2, however, the kinematic collision kernel is too small. The reason for this becomes clear in Figure 6.16*b*, which shows the RDF in case of the replacement algorithm. By replacing the particles, an artificial drop in the RDF at $r = 2a$ is created. Therefore the RDF at the collision radius $g(2a)$, shown in Figure 6.17*a*, cannot be estimated correctly. The same is true for the RRV at contact, shown in Figure 6.17*b*.

It would be desirable to have a better understanding of how the replacement algorithm affects the estimation of $g(2a)$ and $\langle |w_r| \rangle$. At the moment we cannot provide a conclusive explanation.
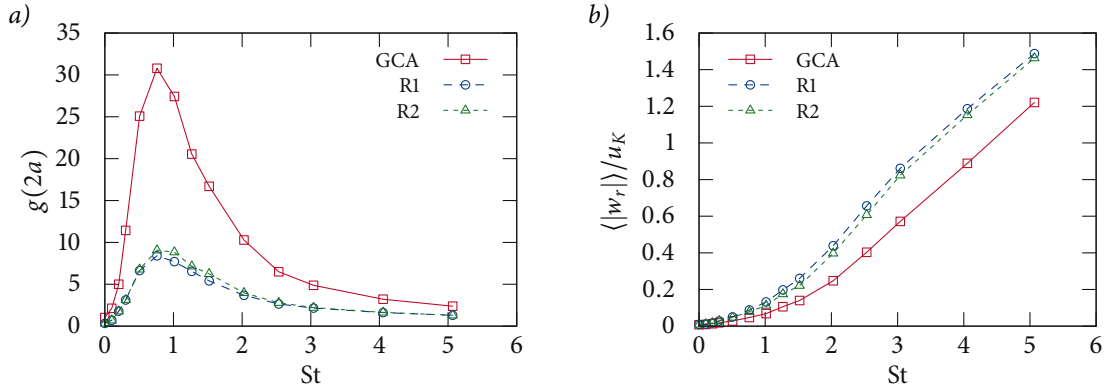
FIGURE 6.17

The RDF (*a*) as well as the mean RRV (*b*) at contact. Shown is data obtained in the GCA and in the alternative algorithms from Section 6.5.

6.6 CONCLUSION AND PERSPECTIVES

We have discussed two striking effects, that can be observed for inertial particles in turbulent flows. Those particles have a tendency to stay in proximity for very long times of the order of the large eddy turnover time. This effect had been reported for tracer particles, but we have shown, that it remains valid for particles with inertia. It slowly decays with growing Stokes number. We presented a thorough study, especially in terms of the contact time PDF. The latter shows some features, which are related to the motion of ideal gas-like particles. But additionally, the contact time PDF shows exponential tails for long contact times.

The fact, that the particles have a certain probability to stay close for long times, has as a consequence that multiple collisions between these particles take place. This effect was studied as well and the corresponding PDF of the number of collisions per pair was discussed. It displays exponential tails leading to a simple modeling of the collision rate for multiple collisions.

These multiple collisions lead to an overestimation of the collision kernel in the GCA. An improved estimate, namely the collision kernel for only first collisions Γ_1 was proposed. Determining the latter is however a tedious task. Therefore an alternative algorithm was proposed, which delivers the correct result in the limit of very dilute suspensions.

PERSPECTIVES   An important aim for future work is to gain a better understanding of the multiple collision events. One can imagine that these events are related to coherent structures in the flow. For instance, the particles which stay together for a long time could be trapped in a strong vortex tube. Answering these questions would necessitate the knowledge of typical fluid parameters, like the fluid velocity or vorticity, along the particle trajectories. This has not yet been implemented, but is in principle feasible and can be envisaged for subsequent work.

In Section 6.1 we compared, as much as feasible, our results to those of Andersson et al. (2007) and Gustavsson & Mehlig (2013a). This theoretical work is based on simplifying assumptions (small Kubo numbers), and it has only been tested in Gaussian random flows. It would be interesting to test the validity of the theoretical approach, at small Kubo numbers, with the help of DNS.

Recently Gustavsson & Mehlig (2011a, 2013b) have developed a theory which describes the PDF of the RRV. At the moment, we do only determine this PDF for *colliding* particles, as presented in Figure 6.11. Applying techniques along the lines of Section 3.2.8 to obtain the PDF for colliding particles from the results of Gustavsson & Mehlig (2011a, 2013b) proves nontrivial. But it is feasible to calculate exactly those quantities for which their theory holds in our simulations. This necessitates the implementation of additional features, which can be envisaged as a future project.

Let us conclude this section by noticing that several significant approximations have been used here, and that it would be important to quantify the errors they induce. For cloud physics applications, the influence of gravity on the effects described in this chapter would need to be studied (Grabowski & Vaillancourt 1999). Also, the role of polydispersity is known to be very important, so similar studies should be carried out for bidisperse solutions with a wide range of particle size differences. The particles that stay together are those which simply follow the flow. We know that for Stokes numbers of moderate size, a fraction of the particle population essentially follows the flow. Therefore we do expect to observe the effects described in this chapter for polydisperse suspensions as well. But they remain to be quantified.

Finally the role of hydrodynamic interactions (see Section 3.2.7) should be studied. This would demand the implementation of slightly more complicated models, like the one by Ayala et al. (2007) and Wang et al. (2005a). The most interesting question in this realm is probably, in how far the phenomenon of multiple collisions affects the collision efficiency (introduced in Section 3.2.7).

PREVALENCE OF THE SLING/CAUSTICS EFFECT

In Section 3.2.4 we presented the decomposition of the collision kernel

$$\Gamma_{SC} = 2\pi(2a)^2\langle|w_r|\rangle g(2a), \tag{7.1}$$

which was rigorously derived by Sundaram & Collins (1997). It has been demonstrated to give the correct results (see also Figure 5.5). The aim of introducing this composition was to study the influence of the preferential concentration effect on the collision rate. But the interpretation of Equation (7.1) is actually more subtle, and the aim of this section is to reconsider it in light of our own numerical results.

We begin by noting that, of course, by the introducing of the RDF, the clustering effect is correctly taken into account by Equation (7.1). Also, the RDF at contact $g(2a)$ grows with the Stokes number, as can be seen in, e.g., Figure 5.4a. Therefore the clustering of particles enhances the collision rate to some extent. But at the same time also the mean RRV $\langle|w_r|\rangle$ increases (Figure 5.4b) thereby additionally enhancing the collision rate. The increase of the mean RRV is due to the presence of a further effect, which is—like the preferential concentration—not present at St = 0, namely the sling/caustics effect as presented in Section 3.2.5. This effect was first described by Falkovich et al. (2002) and independently by Wilkinson & Mehlig (2005) and Wilkinson et al. (2006).

Equation (7.1), while correctly describing the collision rate in the GCA, does not distinguish the two effects, and simply rests on an "effective theory". It is therefore difficult to evaluate precisely which of the two effects accounts for the enhancement of the collision rate as a function of the Stokes number. In this chapter, we demonstrate that our numerical data show very clearly that the sling/caustics contribution provides the dominant mechanism enhancing the collision rate, even at relatively small Stokes numbers. We also show that our results can be best understood with a representation of the collision rate as introduced in Equation (3.15).

The decomposition (7.1) describes the collision rate in the GCA, hence all collision kernels presented in this chapter are obtained in this approximation and suffer from the insufficiencies discussed in Chapter 6. This fact will however not affect the conclusions, which are based on qualitative features of the results, rather than on exact quantitative values.

7.1 DIFFERENT SCALING OF THE COLLISION KERNELS

Remember the decomposition proposed by, e.g., Gustavsson & Mehlig (2011a) or Ducasse & Pumir (2009)

$$\Gamma = \Gamma_{ST}\, g(2a) + \Gamma_A\, h_S(\mathrm{St}, \mathrm{Re}_\lambda) \tag{7.2}$$

from Section 3.2.5 [there printed as Equation (3.15)]. It states that the total collision kernel in a turbulent flow is a combination of Saffman & Turner's (1956) and Abrahamson's (1975) collision kernels. It is interesting to note that the first term, which is due to shearing motion and affects particles that follow the flow, scales like $\Gamma_{ST} \sim (2a)^3/\tau_K$—see Equation (3.6). The other term however, which describes particles that are decorrelated from the fluid motion and may collide with large relative velocities, scales like $\Gamma_A \sim (2a)^2\eta/\tau_K$—see Equation (3.8). Both terms have a prefactor, but only one of them depends on the particle radius a. It has been shown in Section 5.3.1 that $g(r) \sim r^{-c_{g,1}}$. Therefore the entire first part scales like $\Gamma_{ST}\, g(2a) \sim (2a)^{3-c_{g,1}}$, which is always different from $\Gamma_A \sim (2a)^2$ as $c_{g,1} < 1$ (see Figure 5.3b). Hence both terms on the right-hand side of Equation (7.2) behave differently when the size of the particles is changed. The dimensionless Stokes number, $\mathrm{St} = \frac{2}{9}(\rho_p/\rho_f)(a/\eta)^2$, introduced in Section 2.3.1, is the crucial parameter that specifies the dynamics of the particles. This means that the particle size a can be changed without affecting the value of the Stokes number, if at the same time the density ratio ρ_p/ρ_f is varied. We used this fact to investigate the scaling with regard to the particle radius a of the collision kernel in our DNS. To this end we post-processed our data as described in Chapters 4 and 5, but here under the assumption of three different density ratios. These ratios were chosen such that the according particle radii are within a factor two of each other.

The collision kernel obtained for the three different particle radii is shown in Figure 7.1. Both scalings, the one according to Γ_{ST} and the one according to Γ_A, are presented. Saffman & Turner (1956) obtained their result for $\mathrm{St} \to 0$ and in this limit the scaling of their collision kernel, $\sim (2a)^3/\tau_K$, works perfectly. But already for relatively small Stokes numbers our results start to diverge, demonstrating that the scaling is not valid anymore. The scaling which one expects for sling/caustics collisions is correct for larger Stokes number, as can be seen from the good correspondence of our results in Figure 7.1b.

The work of Abrahamson (1975) has been criticized as being inexact, because it takes not into account the multiscale structure of turbulent flows. Therefore alternative versions of the function $h_S(\mathrm{St}, \mathrm{Re})$ have been proposed, e.g., by Völk et al. (1980). Mehlig et al. (2007) derive by dimensional analysis $h_S(\mathrm{St}, \mathrm{Re} \to \infty) \sim \mathrm{St}^{1/2}$. Such a behavior is not present in Figure 7.1b, possibly due to a too small Reynolds number in our simulations.

From Figure 7.1 it becomes clear that for $\mathrm{St} \to 0$ the shear induced collisions describe the overall collision kernel correctly and that for larger Stokes numbers the sling/caustics effect is more important. But the influence of the preferential concentration effect described by $g(2a)$ is not evident. Therefore we plotted in Figure 7.2 the ratio of the collision kernels obtained for two different density ratios. In each case the particle radii differ by a factor of two. Hence one would expect a value of ⅛, if $(2a)^3/\tau_K$ was the correct scaling and a value of ¼ for $(2a)^2\eta/\tau_K$. The entire first term of Equation (7.2) including $g(2a)$ leads to a value of $(1/2)^{3-c_{g,1}}$. Figure 7.2 shows these three
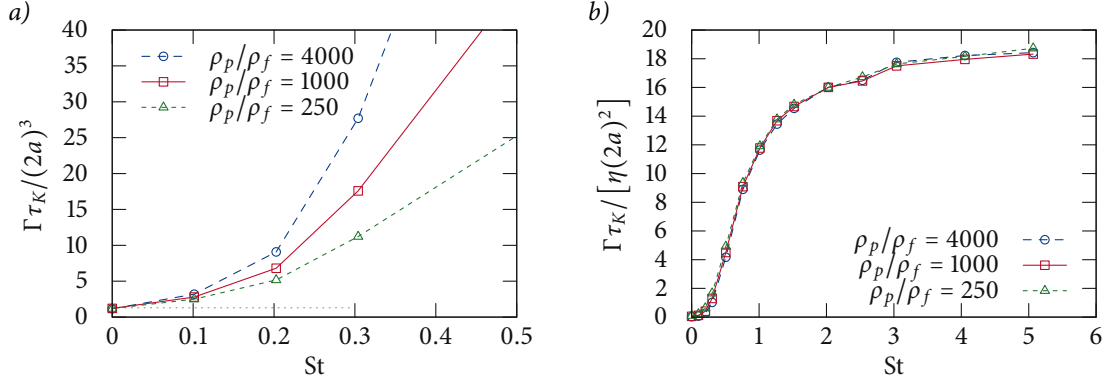
FIGURE 7.1

The collision kernel for three different particle radii (tuned with the help of the density ratio ρ_p/ρ_f). In panel (a) it is shown in the scaling according to Γ_{ST} and only for a range of small Stokes numbers. The value of Γ_{ST} is also shown as a straight dotted line. Panel (b) shows the full range of Stokes numbers in the scaling imposed by Γ_A.
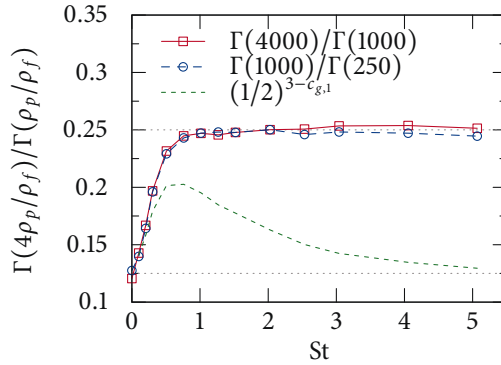

FIGURE 7.2

Ratios of the collision kernels of particles with the same Stokes number, but whose radii differ by a factor two. If the collisions according to the description by Saffman & Turner (1956) dominate, one expects a value of 0.125; else, if most collisions correspond to the description by Abrahamson (1975), the expected value is 0.25. We compare raindrop-like particles ($\rho_p/\rho_f = 1000$) once to two times larger particles ($\rho_p/\rho_f = 250$) and once to two times smaller particles ($\rho_p/\rho_f = 4000$). The dashed line represents the expected scaling of the first term on the right-hand side of Equation (7.2).

values as well as the ratios of the collision kernels we obtained in our DNS. For St < 0.2 the numerical results follow the dashed line given by $(1/2)^{3-c_{g,1}}$. This means that in this range the enhancement of the collision kernel is almost entirely due to the effect of preferential concentration. At larger Stokes numbers however, the dashed line and the numerical results start to diverge. For St $\gtrsim$ 0.75 the curve $(1/2)^{3-c_{g,1}}$ has reached its maximum and starts to fall. Nevertheless the numerical results continue to grow and reach the value ¼, which is expected for sling/caustics collisions. This leads to the conclusion that at larger values of the Stokes number the majority of collisions is due to the sling/caustics effect.

FIGURE 7.3

The cumulative PDF of the RRV $F(|w_r|)$ as defined in Equation (7.3) and the contribution of RRVs smaller than $|w_r|$ to the flux entering the collision sphere $\varphi(|w_r|)$ defined in Equation (7.4). Both are shown for St = 0.5 and in two different scalings: Once in units of the Kolmogorov velocity u_K (bottom axis) and once in units of the shear rate at the particle size $2a/\tau_K$ (top axis).
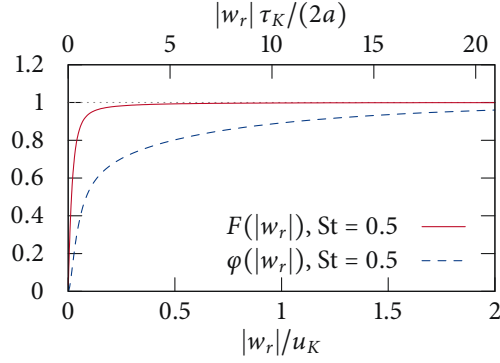
7.2 CUMULATIVE PDF

To provide further evidence for the prevalence of the sling/caustics effect, we calculated the cumulative PDF of the RRV, defined as

$$F(|w_r|) = \int_0^{|w_r|} p(|w_r'|)\, dw_r'. \tag{7.3}$$

The cumulative PDF $F(|w_r|)$ allows us to see, which values of $|w_r|$ are the most probable. For instance, one can read from Figure 7.3 that for St = 0.5 only about 5 % of the particles have relative velocities larger than $|w_r| \gtrsim 2a/\tau_K$.

In addition to $F(|w_r|)$, we calculated the ratio of particles entering the collision sphere with RRV smaller than $|w_r|$

$$\varphi(|w_r|) = \int_0^{|w_r|} \frac{|w_r'|}{\langle |w_r| \rangle} p(|w_r'|)\, dw_r'. \tag{7.4}$$

This can be interpreted as the contribution of velocities smaller than $|w_r|$ to the total collision rate. Along the lines of Sections 3.2.8 and 4.3.1, $\varphi(|w_r|)$ can also be seen as the cumulative PDF of the RRV conditioned on collisions. Figure 7.3 shows that at St = 0.5, although rare, particles with $|w_r| \gtrsim 2a/\tau_K$ contribute about 50 % of the collisions. The collisions with larger RRV are likely to be sling/caustics collisions. Therefore, the numerical values presented here provide a strong evidence that the sling/caustics effect starts to become the leading mechanism enhancing the collision rates already at relatively small Stokes numbers.

Figure 7.4 shows $F(|w_r|)$ and $\varphi(|w_r|)$ for two further Stokes numbers, St = 0.1 and St = 0.75. By comparing the two, the transition from small to large Stokes values becomes evident—note especially the change of scale in the horizontal axes. At small values of St shear induced collisions prevail. Almost all particles have very low RRV and almost all collisions take place at such low RRV. For increasing Stokes numbers however, more particles move at larger RRV and even more collisions are contributed by these particles.
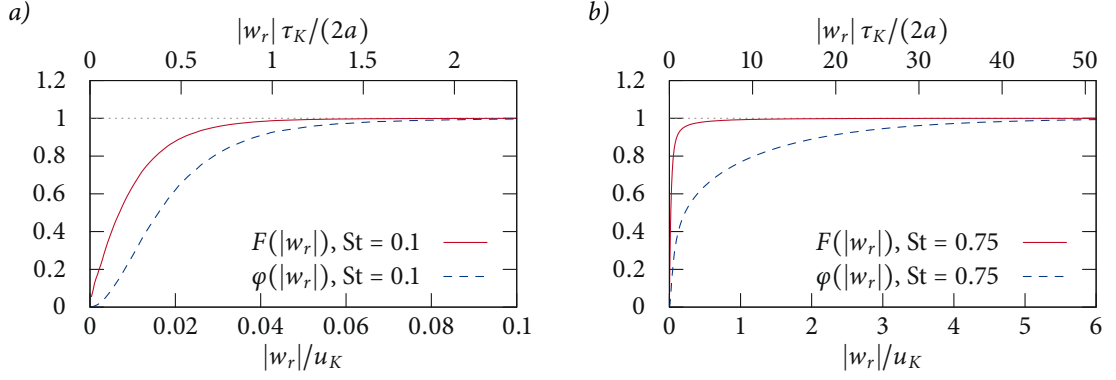
a)

b)

FIGURE 7.4

The same quantities as in Figure 7.3, but here in (*a*) for St = 0.1 and in (*b*) for St = 0.75.
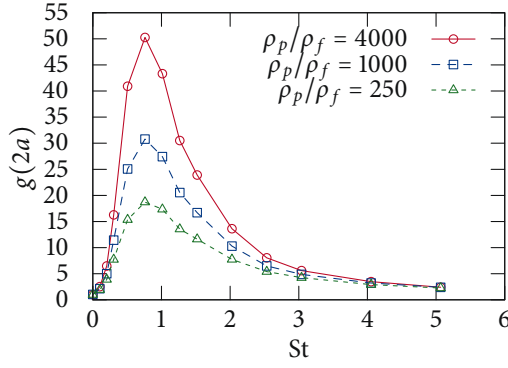

FIGURE 7.5

The RDF at contact $g(2a)$ for differently sized particles (as tuned by the density ratio ρ_p/ρ_f). The smaller the particles, the larger $g(2a)$.

7.3 COMPARISON TO PUBLISHED RESULTS

In Section 7.1 the prevalence of the sling/caustics effect for particle collisions in turbulent flows was deduced from an analysis of the scaling dependence of the collision rate as a function of the particle radius a. To this end numerical simulations of particles with the same Stokes number but varying radii were carried out. Looking again at past numerical and theoretical results, we explain in this section that our conclusions are in fact fully supported by numerical evidence obtained in previous works.

Equation (7.1) reduces the collision kernel to two quantities which have been the subject of many studies, namely $g(2a)$ and $\langle|w_r|\rangle$. Both quantities depend on the particle radius a as can be seen in Figures 7.5 and 7.6, but in different ways. While the RDF becomes larger with decreasing particle radius, the RRV grows with increasing radius. According to Equation (7.1) these opposing behaviors must cancel exactly for larger Stokes values, in order to give the correct scaling of the collision kernel $\sim a^2$. Figure 7.7 demonstrates that this is indeed the case.

A similar observation allows to confirm our results concerning the scaling of the collision kernel by comparison with published data. The RDF $g(r)$
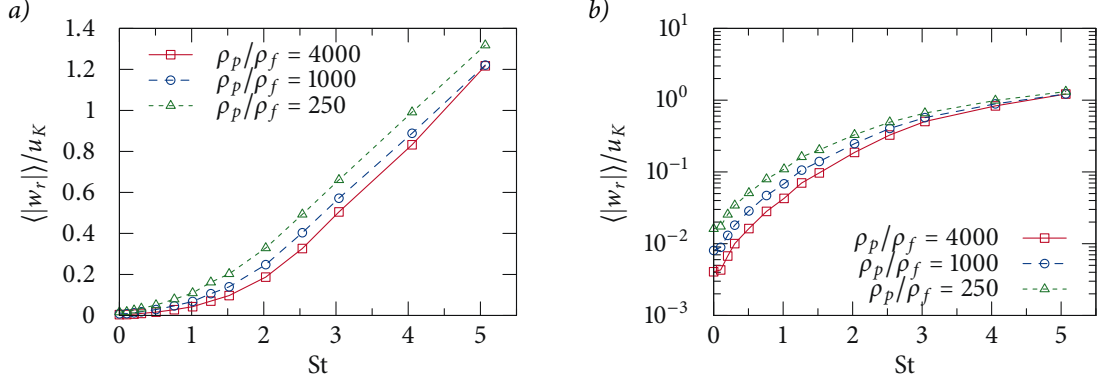
FIGURE 7.6

The RRV at contact for particles of different radii, shown in panel (*a*) in linear scaling and in panel (*b*) in logarithmic scaling. The radius was changed at constant Stokes number by varying the density ratio ρ_p/ρ_f. For growing radii, the RRV increases.
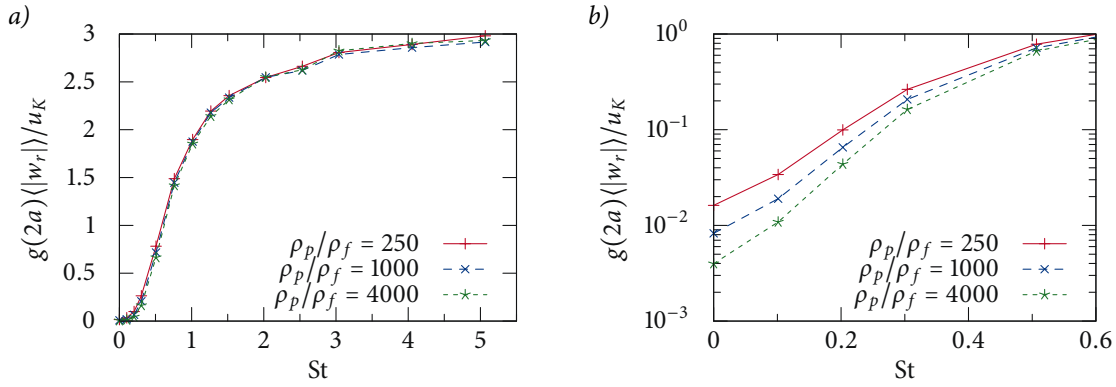
FIGURE 7.7

The RRV multiplied by the RDF at contact. Both scale differently with the particle radius as can be seen in Figures 7.5 and 7.6. Nevertheless for larger Stokes numbers the three curves, which are for particles of different sizes, coincide. Only for small Stokes numbers a difference is present. This can be seen from the zoom in panel (*b*) which gives the same data as panel (*a*) but in logarithmic scaling.
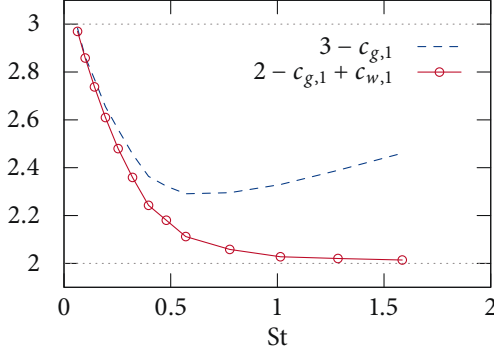
FIGURE 7.8

The exponent of the scaling of the kinematic collision kernel with the particle radius a (circles). Shown is data from Rosa et al. (2013), who report on $c_{g,1}$ and $c_{w,1}$. The straight dotted lines correspond to the scalings for shear collisions ($\sim a^3$) and sling/caustics collisions ($\sim a^2$). The dashed line is the scaling of shear induced collisions including the preferential concentration effect.

obtained in our DNS was shown in Figure 5.3. For small distances $r \ll \eta$ it is described very well by a power-law $g(r) \sim r^{-c_{g,1}}$. Therefore $g(2a)$ must scale like $(2a)^{-c_{g,1}}$. Up to now, only the RRV at contact $\langle |w_r| \rangle$ was discussed in this work. But it is a known fact, that for small separations the RRV scales with the distance at which it is calculated as $\langle |w_r(r)| \rangle \sim r^{+c_{w,1}}$ (e.g., Bec et al. 2010). Theories to predict this power law behavior have been proposed by Gustavsson & Mehlig (2011a, 2013b), who studied in fact a simpler random flow model. As a consequence the collision kernel must scale with the particle radius as $\Gamma_{SC} \sim a^{2-c_{g,1}+c_{w,1}}$.

Rosa et al. (2013) present a thorough study of the collision kernel in DNS. Among others, they show data for $c_{g,1}$ and $c_{w,1}$. From that data we obtained the scaling of the collision kernel $2 - c_{g,1} + c_{w,1}$, which we present in Figure 7.8. Their results confirm ours from Section 7.1. For very small Stokes numbers the scaling of the collision kernel approaches the value expected from Saffman & Turner (1956). But for growing values of the Stokes number, the scaling exponent quickly approaches 2. In this sense, the results of Rosa et al. (2013) provide evidence that for St $\gtrsim 0.75$ the collision rate is determined predominantly by sling/caustics collisions. We note that this phenomenon had in fact been predicted, in the case of simple flow models by Gustavsson & Mehlig (2011a, 2013b) in the spirit of earlier work by Wilkinson et al. (2006).

7.4 CONCLUSION AND PERSPECTIVES

We investigated here collision rates in turbulent flows. Two effects are known to lead to a strong enhancement, with respect to the Saffman–Turner prediction, of the collision rate. On the one hand shear induces collisions of particles which are already in proximity. This effect is enhanced by preferential concentration which augments the particle density in certain regions. On the other hand the sling/caustics effect describes how particles, which come from different regions of phase space, may collide with large RRV. We have shown that for small Stokes numbers an enhancement of the collision rate is due to preferential concentration. But as the Stokes number increases

the sling/caustics effect becomes more and more important, whereas the effect of preferential concentration looses influence. We could identify the region St $\gtrsim 0.75$ as the one where the majority of collisions is due to the sling/caustics effect.

Our conclusions rely on two arguments. First, the scaling of the collision kernel with the particle radius is different for the two effects. But for St $\gtrsim 0.75$ our numerical results reach the value imposed by the sling/caustics effect. Secondly, the cumulative PDF of the RRV $F(|w_r|)$ and a derived quantity $\varphi(|w_r|)$ allowed us to show that for growing Stokes numbers an increasing ratio of collisions happens at large RRV. These collisions are induced by the sling/caustics effect.

PERSPECTIVES   As was the case in Chapter 6, it would be interesting to study the influence of the different approximations that lead to the model investigated numerically. In particular, neglecting gravity tends to "artificially" enhance the collision rate (see, e.g., Rosa et al. 2013). Therefore an important question would be, which of the two different contributions is more affected by the inclusion of gravity. Also the investigation of polydisperse solutions could provide interesting insights. Generally, the collision kernel $\Gamma(a, a')$ is a complicated function of both variables, especially in the presence of gravity (see, e.g., Grabowski & Wang 2009; Woittiez et al. 2009). It is therefore difficult to predict, whether the sling/caustics effect is of similar importance in bidisperse solutions—a thorough investigation would be necessary.

KINEMATIC SIMULATIONS

When we started our investigations of the collision rates of particles in turbulent flows, we did not yet use DNS. Instead we used a simple model flow introduced by Fung et al. (1992) known as kinematic simulations (KS). We learned much from this model, as it allowed us to perform simulations with a very low numerical effort. Also, essentially all the qualitative information we obtained with KS turned out to be in full agreement with the results we obtained with DNS. However, in quantitative terms, we find a large difference between the two approaches. It is the objective of this chapter to discuss the similarities and differences in the KS and DNS problems. The essential conclusion of our comparison is that the sling/caustics effect, as well as preferential concentration, play a much reduced role in KS as compared to DNS. In the light of these observations, studying collisions using KS instead of exact DNS leads to results which should be interpreted with care.

In this chapter we shortly introduce KS before presenting results analogous to those from Chapters 6 and 7. We will focus especially on differences in comparison to the results obtained with DNS. Although a complete understanding of the origin of this difference is still missing, we will present several remarks, aimed at explaining the observed discrepancies.

8.1   DESCRIPTION OF THE APPROACH

The basic idea of KS is to obtain the fluid velocity field $\boldsymbol{u}(\boldsymbol{x}, t)$ as a sum of N_k random Fourier modes

$$\boldsymbol{u}(\boldsymbol{x}, t) = \sum_{n=1}^{N_k} \boldsymbol{a_n} \cos(\boldsymbol{k_n} \cdot \boldsymbol{x} + \omega_n t) + \boldsymbol{b_n} \sin(\boldsymbol{k_n} \cdot \boldsymbol{x} + \omega_n t). \qquad (8.1)$$

These modes k_n and the corresponding coefficients $\boldsymbol{a_n}$ and $\boldsymbol{b_n}$ are chosen such that the resulting flow fulfills certain properties. The wave vectors $\boldsymbol{k_n} = k_n \hat{\boldsymbol{k}}_n$ are pointing in random directions $\hat{\boldsymbol{k}}_n$. To assure incompressibility the directions of the coefficients need to fulfill

$$\hat{\boldsymbol{a}}_n \cdot \hat{\boldsymbol{k}}_n = \hat{\boldsymbol{b}}_n \cdot \hat{\boldsymbol{k}}_n = 0.$$

The amplitudes of these coefficients govern the energy spectrum of the flow $E(k_n)\Delta k_n = a_n^2 = b_n^2$. We impose a spectrum $E(k_n) = E_0 k_n^{-5/3}$ and define the discrete differences between the wave vectors

$$\Delta k_n = \begin{cases} (k_2 - k_1)/2, & n = 1 \\ (k_{n+1} - k_{n-1})/2, & n \in [2, N_k - 1] \\ (k_{N_k} - k_{N_k-1})/2, & n = N_k. \end{cases}$$

Different choices of the energy spectrum, as discussed by Malik & Vassilicos (1999), are possible.

For the amplitudes of the wave vectors there are two possibilities. We choose a geometric distribution

$$k_n = k_1 \left(\frac{L}{\eta} \right)^{(n-1)/(N_k-1)}, \qquad k_1 = \frac{2\pi}{L}, \qquad k_{N_k} = \frac{2\pi}{\eta}. \qquad (8.2)$$

The alternative would be an algebraic distribution as discussed by, e.g., Fung & Vassilicos (1998). In Equation (8.2) L denotes a large and η a small length scale. They may be interpreted as the integral and the Kolmogorov length respectively [note however, that L does not fulfill Equation (5.1)]. We have $L/\eta = 64$ in all simulations discussed here. Malik & Vassilicos (1999) present a comparison between KS and DNS. They obtain a good agreement for a total number of modes $N_k \gtrsim 100$. Therefore we chose $N_k = 109$ which assures 18 modes in each band $[k, 2k]$.

The frequencies ω_n in Equation (8.1) are defined to be proportional to the eddy turnover time on the corresponding length scale

$$\omega_n = \lambda \sqrt{k_n^3 E(k_n)}.$$

The unsteadiness parameter in our simulations was $\lambda = 0.5$. This value is expected to give results similar to those obtained from DNS concerning Lagrangian dispersion (Malik & Vassilicos 1999; Nicolleau & ElMaihy 2004).

All parameters are determined in the initial phase of each simulation. They are not changed for the rest of the run time. Therefore the "randomness" in each run is limited and results do vary with the initial state of the random number generator (RNG). We use the well-known Mersenne twister (Matsumoto & Nishimura 1998) as RNG. For each set of parameters we perform 10 runs initializing the RNG with a different seed. We obtain our final results by averaging over the individual runs.

Our simulations are based on those described by Ducasse (2009) and Ducasse & Pumir (2009). Further details may be found there.

8.1.1 *Integration of particle trajectories*

Equation (8.1) provides a complete representation of the velocity field at any point in space. This is a big advantage over DNS which rely on interpolation schemes to calculate the velocity in between grid points. To obtain the particle trajectories, we integrate Equations (2.16) and (2.17) with a low storage Runge–Kutta scheme of fourth order. This scheme is presented in detail by Gottlieb et al. (2001) based on work by Carpenter & Kennedy (1994). As a rule of thumb we use for the time-step $\Delta t = \min(\tau_p/5, \tau_K/5)$. We also integrate the particle velocity gradient tensor σ_{ij} as defined in Section 2.3.2 with the same scheme. This quantity may diverge, therefore its integration demands some special care. The technical details of this procedure are described in Appendix B.
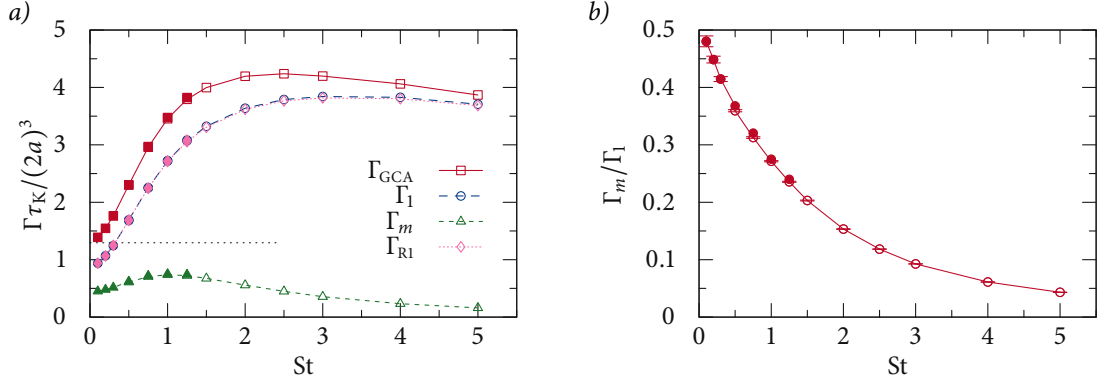
FIGURE 8.1

Panel (*a*) shows four different collision kernels obtained in KS. Γ_{GCA} has been obtained in the GCA, Γ_1 takes into account only first collisions of a same pair, Γ_m represents multiple (i.e., at least two) collisions between a same pair, and Γ_{R1} was determined with the alternative algorithm R1. The straight dotted line gives the Saffman–Turner estimate for St → 0 (Section 3.2.2). Panel (*b*) shows the ratio Γ_m/Γ_1. As always in this chapter, filled symbols represent data obtained with a volume fraction $\Phi = 1.2 \times 10^{-5}$ and empty symbols such obtained with $\Phi = 1.2 \times 10^{-4}$.

In KS the system size L_{sys} can be an arbitrary multiple of L. In our simulations it is $L_{sys} = 2L$. Specifying the system size and a volume fraction Φ determines the number of particles N_p at a certain Stokes number. Due to numerical constraints, we divided the range of Stokes numbers we investigated in DNS into two overlapping regions. In the range St ≤ 1.25 we performed simulations with $\Phi = 1.2 \times 10^{-5}$. In the range St ≥ 0.5 we did another set of simulations with $\Phi = 1.2 \times 10^{-4}$. The smaller volume fraction is represented by filled symbols in all graphics in this chapter. Empty symbols, if they correspond to data obtained in KS, represent values from simulations with the higher volume fraction. We used again the alternative algorithm R1 introduced in Section 6.5.1. In the corresponding simulations 10 % additional particle trajectories were integrated.

8.2 COLLISION KERNELS

We determined the different collision kernels defined in Chapter 6 for KS. The results are shown in Figure 8.1*a*. First of all one notes that the general aspect is the same in KS as it was in DNS. Of all the collision kernels Γ_{GCA} is the largest. The two corrected collision kernels Γ_1 and Γ_{R1} are smaller than Γ_{GCA}. In contrast to our DNS results, here Γ_1 and Γ_{R1} coincide although the volume fraction is even higher. In Chapter 6 we had shown that Γ_{R1} was smaller than Γ_1 by a factor proportional to the volume fraction Φ. A further difference becomes obvious, when one compares the quantitative values. The collision kernels we found in DNS were larger by more than one order of magnitude for St ≳ 1.5. For St → 0 the prediction of Saffman & Turner (1956) is correctly reproduced in both approaches.
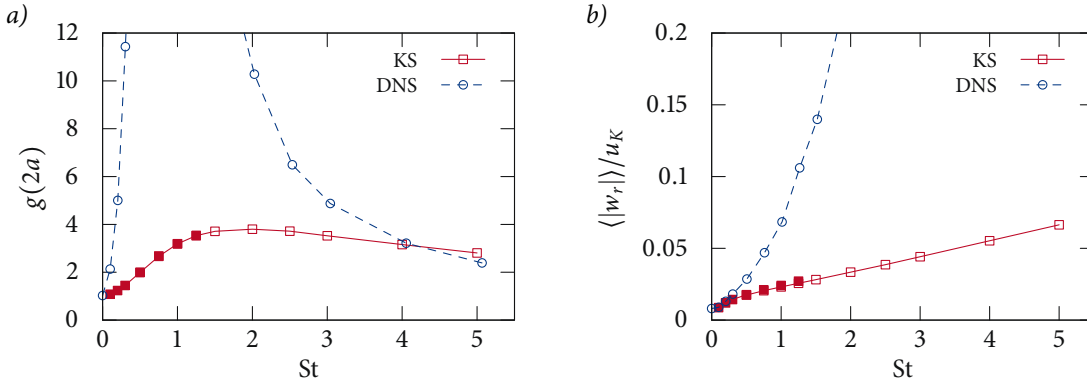
The RDF (*a*) and the RRV (*b*) at contact as obtained in our KS in comparison to results from DNS. The difference between filled and empty symbols is explained in the caption of Figure 8.1.

Figure 8.1*b* shows the ratio Γ_m/Γ_1 as in Figure 6.1*b*, but here for KS. Again the qualitative features are similar, but here we find a maximal error introduced by multiple collisions which is almost 50 %. For comparison, in DNS the maximal error was around 15 %. We conclude that while the overall number of collisions is reduced in KS, the ratio of multiple collisions is higher than in DNS.

The reasons for the large quantitative differences between KS and DNS become a bit clearer from Figure 8.2. There the two constituents of the formulation of the collision kernel as proposed by Sundaram & Collins (1997) [Equation (3.14)] are shown. In comparison to DNS there is almost no clustering in KS, as can be seen from the RDF shown in Figure 8.2*a*. Also the RRV is much smaller (Figure 8.2*b*). Apparently both effects leading to an enhancement of the collision rate—preferential concentration and the sling/caustics effect—are strongly reduced in KS.

Further evidence is provided to some extent by Figure 8.3. It shows the ratio of the mean collision velocity for only first collisions and for all collisions in the GCA. The corresponding data was shown for DNS in Figure 6.12. Because multiple collisions are so rare for larger Stokes values and because the statistics is dominated by sling/caustics collisions, this ratio drops very quickly in the case of DNS. For KS however, this ratio stays significant even for larger values of the Stokes number. This underlines again the suppression of sling/caustics collisions in KS.

The reduced preferential concentration provides also an explanation why we find in Figure 8.1*a* that $\Gamma_{R1} \approx \Gamma_1$. The difference between these two collisions kernels was shown to be proportional to the volume fraction in Chapter 6. More precisely it depends on the effective volume fraction in the region of a particle, namely $g(r)\Phi$. Therefore, if $g(r)$ is smaller in KS, as was shown in Figure 8.2*a*, also the difference between Γ_1 and Γ_{R1} will be reduced.

Finally, in Figure 8.4, we show the PDF of the collision velocity for St = 1.0. It is qualitatively similar to the one for DNS shown in Figure 6.11. But it
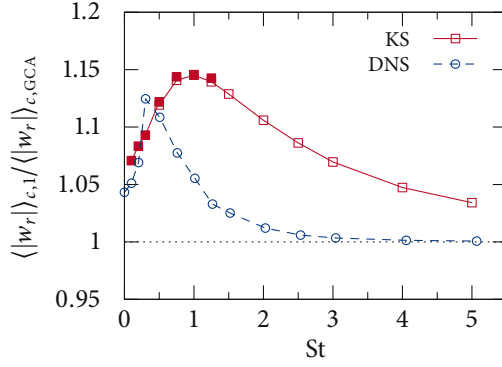
The ratio of the mean collision velocities for only first collisions and in the GCA. Results from KS and DNS are compared. Filled and empty symbols have the meaning as specified in the caption of Figure 8.1
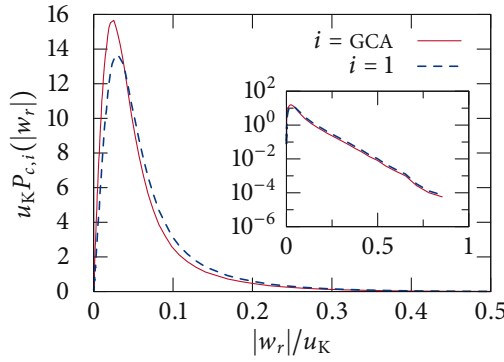
The PDF of the RRV conditioned on the fact that two particles collide. To determine this PDF once all collisions detected in the GCA were taken into account (full lines). Another time only first collisions of a same pair were considered to determine the statistics (dashed lines). The data is for St = 1.0 and was obtained in KS. This figure may be compared to Figure 6.11 where the same quantity is shown for DNS.

peaks at a much smaller velocity and the exponential tails are shorter by an order of magnitude. This provides further confirmation that there are fewer sling/caustics collisions in KS.

8.3 MULTIPLE COLLISIONS

The presence of multiple collisions in KS has become obvious in the previous section. Here we present the statistics of these multiple collisions. In Figure 8.5 we show the PDF of undergoing N_c collisions after an initial one in KS, $P(N_c|N_c \geq 1)$. The same PDF has been shown for DNS in Figure 6.2a. We find again, that this PDF can be described by a function $P(N_c|N_c \geq 1) = \beta \alpha^{N_c}$, although there are larger deviations in the tails as was the case for DNS. For KS we find in general a larger probability for multiple collisions. This is especially evident in the values of the fit coefficient α which is shown in the inset of Figure 8.5. It is roughly two times larger than in DNS. The high probability for multiple collisions underlines again the fact that sling/caustics collisions are less probable in KS. The sling/caustics collisions do not contribute to the multiple collisions and would therefore diminish their probability.

FIGURE 8.5

The probability for a pair of particles to undergo an N_c-th collision conditioned on the fact that it collided at least once. The data shown here was obtained in KS. The different lines show fits according to Equation (6.2). In the inset the fit coefficient α is shown. There the full and empty symbols have again the meaning as explained in Figure 8.1. An analogous graph was shown for DNS in Figure 6.2a.
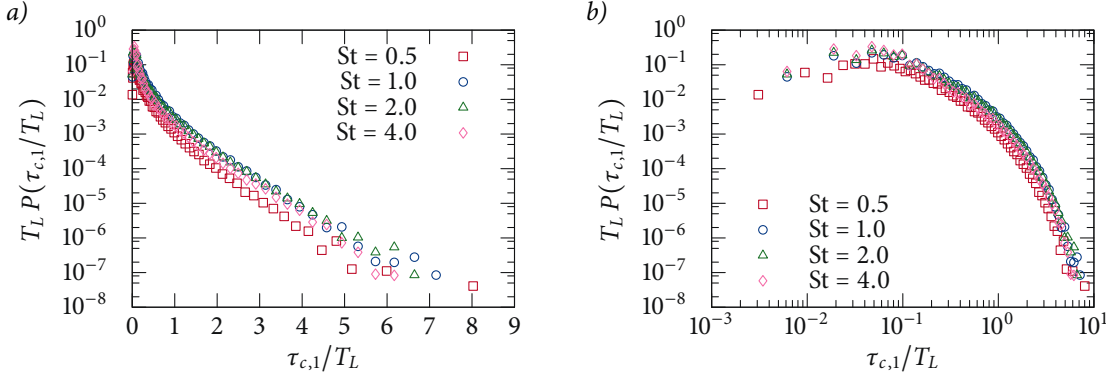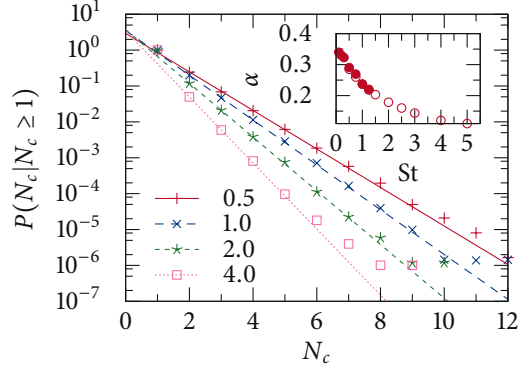
FIGURE 8.6

The first contact time PDF obtained in KS for different Stokes numbers as indicated in the legend. The data is given in semi-logarithmic (a) and doubly-logarithmic (b) scaling. The same quantity is shown in Figure 6.9 for DNS.

8.3.1   Contact time PDF

We also determined the contact time PDF as defined in Section 6.3 for KS. It is shown in Figure 8.6 for the first contact and for different values of the Stokes number. As in DNS, we find exponential tails for long contact times (Figure 8.6a). The dependence on the Stokes number seems to be a bit less pronounced. The most striking difference however is the absence of the power law behavior for intermediate contact times, even at large Stokes numbers (Figure 8.6b). In Section 6.3 it was explained that this feature of the PDF is mainly due to sling/caustics collisions. Therefore the absence of the power law emphasizes again the lack of this effect in KS. Furthermore it is interesting to note that in KS our temporal resolution suffices to see that the PDF reaches $\tau_{c,1} = 0$ with a negative slope.
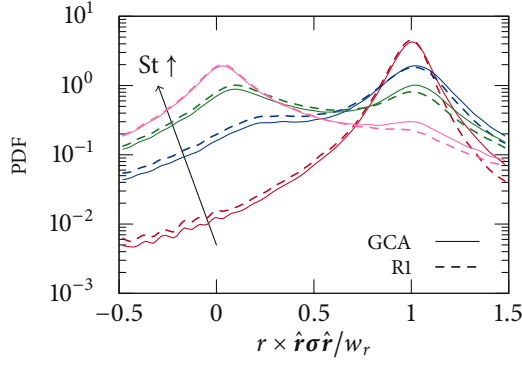
The PDF of the ratio $2a\hat{\boldsymbol{r}} \cdot \boldsymbol{\sigma} \cdot \hat{\boldsymbol{r}}/w_r$ for St $\in$ $\{0.5, 1.0, 2.0, 4.0\}$ as obtained in our KS. The peak at 1 corresponds to shear induced collisions, the peak at 0 corresponds to sling/caustics collisions. We show the PDF obtained in the GCA as well as with the alternative algorithm R1.

8.4 DETECTING SLING/CAUSTICS COLLISIONS WITH THE PARTICLE VELOCITY GRADIENT TENSOR

Typically the particle velocity gradient tensor σ_{ij} can be used to obtain a good estimate for the RRV $w_r(r) \approx \boldsymbol{r} \cdot \boldsymbol{\sigma} \cdot \hat{\boldsymbol{r}}$ as long as the separation r is small enough. If two particles however collide due to the sling/caustics effect, they come from different regions in phase space. This has been explained in Section 3.2.5. Their velocity gradients are different and lead to an estimate that is much smaller than the real RRV between them. This provides a means to decide at every collision, whether it is a shear induced or a sling/caustics collision. One simply has to compare the estimate with the actually measured RRV, i.e., calculate $2a\hat{\boldsymbol{r}} \cdot \boldsymbol{\sigma} \cdot \hat{\boldsymbol{r}}/w_r$. If this ratio is close to one, the collision is induced by shear. If the ratio is close to zero, this means that the actual collision velocity is much larger than the estimate suggests and the collision is therefore a result of the sling/caustics effect. Instead of doing this for every collision it is of course simpler to determine the PDF of the ratio $2a\hat{\boldsymbol{r}} \cdot \boldsymbol{\sigma} \cdot \hat{\boldsymbol{r}}/w_r$. Ducasse & Pumir (2009) present this PDF in a detailed numerical study of collision rates in KS. Here we use the same quantity to reason once again that the spurious effect of multiple collisions is due to shear induced collisions.

In Figure 8.7 we show the PDF of the ratio $2a\hat{\boldsymbol{r}} \cdot \boldsymbol{\sigma} \cdot \hat{\boldsymbol{r}}/w_r$ as obtained in our KS for several Stokes numbers. We estimated the effective gradient tensor $\boldsymbol{\sigma}$ as the average of the two individual particle velocity gradient tensors $\boldsymbol{\sigma}_1$ and $\boldsymbol{\sigma}_2$, i.e., $\boldsymbol{\sigma} = \frac{1}{2}(\boldsymbol{\sigma}_1 + \boldsymbol{\sigma}_2)$. The PDF displays two peaks: One at $2a\hat{\boldsymbol{r}} \cdot \boldsymbol{\sigma} \cdot \hat{\boldsymbol{r}}/w_r = 1$ which corresponds to shear induced collisions; another broader one around zero which corresponds to sling/caustics collisions. The sling/caustics effect becomes more important as the Stokes number grows. This has also been found by Ducasse & Pumir (2009).

Furthermore Figure 8.7 displays for every Stokes number the ratio as determined in the GCA and as determined in the alternative algorithm R1. The difference between the two sheds light on the nature of multiple collisions which are not present in R1. The peak at 1 diminishes when the alternative algorithm is used, while the peak at 0 increases. Therefore the

multiple collisions correspond mainly to shear induced collisions. This is in accordance with the results we found before in Chapter 6.

We did not determine the same quantity in DNS. In the light of our results from Section 8.2, it would however be very interesting to compare the ratio $2a\hat{\boldsymbol{r}} \cdot \boldsymbol{\sigma} \cdot \hat{\boldsymbol{r}}/w_r$ in DNS and KS. We concluded in Chapter 7 that the sling/caustics effect is the dominant contribution to the collision rate in DNS, even at relatively small Stokes numbers. In Section 8.2 it was demonstrated that in comparison to DNS there are very few sling/caustics collisions in KS. Therefore one should expect that the PDF from Figure 8.7 would show a very pronounced peak around zero in DNS even for relatively small Stokes numbers.

8.5   CONCLUSION AND PERSPECTIVES

In this section we presented results obtained in a simple, but established, model for turbulent flows, namely kinematic simulations. On a general perspective these results confirm those from DNS which we presented earlier. But we find a striking discrepancy in quantitative terms. All aspects we investigated confirm an absence or at least a strong suppression of the sling/caustics effect in KS. Also the preferential concentration is much less pronounced. The reason for this could be that the modes in Equation (8.1) are chosen randomly. Therefore it is very unlikely that one finds in KS the coherent structures which are so typical for real turbulent flows. According to the *sling* interpretation these structures are responsible for the sling/caustics effect. They can also be seen as being at the origin of the preferential concentration effect. Therefore the absence of coherent structures in KS would ultimately result in the suppression of the two effects. Future investigations may shed more light on these relationships.

Part III

APPENDICES

INTERPOLATION OF PARTICLE TRAJECTORIES

In Section 4.1.2 two different ways to detect a collision based on the positions and velocities of two particles at consecutive time-steps were introduced. Here, we describe both techniques in more detail.

A.1 LINEAR EXTRAPOLATION

How can one determine that two particles in a distance $r = X_2 - X_1$ moving in relative motion to each other with velocity $w = V_2 - V_1$ eventually collide? To answer this question consider Figure A.1. There, two such particles with radius a are shown. In the following we will consider this situation in the frame of reference where the first particle is at rest. A necessary condition for a collision to take place is that the minimal distance r_{min} between the centers of the particles (given the relative velocity w is constant) is smaller than two times their radius, $r_{min} < 2a$. The minimal distance is the distance between the center of the first particle P_1 and its orthogonal projection onto the hypothetical relative trajectory of the second particle M. Initially the distance $\overline{P_2 M}$ is given by the dot product between the relative distance and the relative velocity $\overline{P_2 M} = r \cdot w / |w|$. So the minimal distance can be obtained by the help of the Pythagorean theorem

This is the usual approach also used in the well-known paper by Saffman & Turner (1956)—see Section 3.2.2.

$$r_{min}^2 = |r|^2 - \frac{(r \cdot w)^2}{|w|^2} \overset{!}{<} (2a)^2. \tag{A.1}$$

Defining $\delta = |w|^2 [(2a)^2 - r_{min}^2]$, Equation (A.1) becomes simply $\delta > 0$.

To introduce a sufficient condition, we have to ask on which timescale τ our hypothesis of a constant relative velocity is satisfied. In numerical simulations this timescale can usually be identified with the time-step. A collision takes place, if the relative distance between the particles falls below $2a$ within a time $\tilde{\tau} < \tau$ given the particles move constantly with relative velocity w. Taking a look at Figure A.1 again, one can determine the point C,

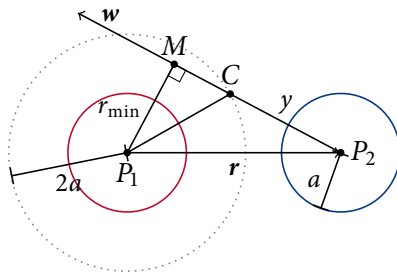FIGURE A.1

Two particles of radius a before an eventual collision. Their vectorial distance is $r = X_2 - X_1$ and they move relative to each other with velocity $w = V_2 - V_1$. More details are given in the text.

where the particle distance is smaller than $2a$ for the first time. To reach this point the second particle has to move a distance y. This distance is equal to

$$y = \overline{P_2 M} - \overline{CM} = \left[\frac{(\boldsymbol{r} \cdot \boldsymbol{w})^2}{|\boldsymbol{w}|^2} \right]^{1/2} - \sqrt{(2a)^2 - x^2} = \frac{\boldsymbol{r} \cdot \boldsymbol{w}}{|\boldsymbol{w}|} - \frac{\sqrt{\delta}}{|\boldsymbol{w}|},$$

where the Pythagorean theorem was used on the triangle (P_1, C, M). Finally the time to travel this distance is given by $\tilde{\tau} = y/|\boldsymbol{w}|$, which has to be compared to the "minimal" timescale τ. If however the collision has already happened in the past, the distance y will be negative and so will be the time $\tilde{\tau}$. Therefore to avoid double counting, i.e., counting the same collision two times in succeeding time-steps, one should also check if $\tilde{\tau} > 0$.

A.2   THIRD ORDER METHOD

The method discussed in the above section is first order in the sense that the particle trajectories are linearly extrapolated in time to detect if they collide within the (up)coming time-step. It is convenient to use, because it only necessitates the knowledge of the particles' position and velocity at one time-step. Unfortunately, as has been explained in Section 4.1.2, this comes not without cost. That is why in this section we present a higher order method.

Using such an interpolation scheme is numerically however relatively costly, therefore it is beneficial to decide early, whether it is *necessary* to calculate it. To this end Wang et al. (1998a) define three different types of collisions, that can happen in between two time-steps, depending on the initial and the final particle distance, $r(t^{(n)})$ and $r(t^{(n+1)})$ respectively, where $r(t) = |\boldsymbol{r}(t)|$.

1. The easiest case is the one, when the particle distance was initially greater than the particle diameter, but is smaller at the end of the time-step, i.e., $r(t^{(n)}) > 2a$ and $r(t^{(n+1)}) \leq 2a$. In this case, which Wang et al. (1998a) refer to as *type I*, (at least) one collision evidently took place.

2. Type II collisions are those, when the initial and final distance are both greater than the particle diameter, $r(t^{(n)}) > 2a$ and $r(t^{(n+1)}) > 2a$, but the distance becomes smaller than $2a$ at an intermediate time t^*, i.e., $r(t^*) \leq 2a$ for one $t^* \subset [t^{(n)}, t^{(n+1)}]$.

3. Type III collisions are, as defined by Wang et al. (1998a), just the opposite of type II ones, i.e., $r(t^{(n)}) \leq 2a$ and $r(t^{(n+1)}) \leq 2a$, but $d(t^*) > 2a$ for one $t^* \subset (t^{(n)}, t^{(n+1)})$.

To detect collisions of type II and type III, knowledge of the particles position in between time-steps is needed. In these cases it is necessary to perform the interpolation.

A.3   THE THIRD ORDER INTERPOLATION AND ITS BOUNDS

Here the interpolation is derived. The two particles' spatial distance in dimension i ($i = 1, d$) in between two time-steps will be denoted as $f^i(t)$ and we seek a representation matching

In this section, the notation differs slightly from the one in the main content.

$$f^i(t) = a + bt + ct^2 + dt^3.$$

The coefficients a, b, c, d can be found, by solving the linear system

$$
\begin{aligned}
f^i(0) &= X_2^i(0) - X_1^i(0) &&= a &&:= \alpha \\
f'^i(0) &= V_2^i(0) - V_1^i(0) &&= b &&:= \beta \\
f^i(\Delta t) &= X_2^i(\Delta t) - X_1^i(\Delta t) &&= a + b\Delta t + c\Delta t^2 + d\Delta t^3 &&:= \gamma \\
f'^i(\Delta t) &= V_2^i(\Delta t) - V_1^i(\Delta t) &&= b\Delta t + 2c\Delta t + 3d\Delta t^2 &&:= \delta
\end{aligned}
$$

Here Δt denotes the length of a time-step and the $X_j^i(t)$ and $V_j^i(t)$ ($j = 1, 2$) are the i-components of the two particles' position and velocity at time t respectively. Finally one obtains

$$a = \alpha \qquad\qquad b = \beta$$

$$c = 3\frac{\gamma - \alpha}{\Delta t^2} - \frac{2\beta + \delta}{\Delta t} \qquad\qquad d = -2\frac{\gamma - \alpha}{\Delta t^3} + \frac{\beta + \delta}{\Delta t^2}$$

Putting this together and sorting for appearances of $\alpha, \gamma, \beta,$ and δ one obtains

$$
\begin{aligned}
f(t) ={}& \alpha\left(1 - 3\frac{t^2}{\Delta t^2} + 2\frac{t^3}{\Delta t^3}\right) + \gamma\left(3\frac{t^2}{\Delta t^2} - 2\frac{t^3}{\Delta t^3}\right) \\
&+ \beta\left(t - 2\frac{t^2}{\Delta t} + \frac{t^3}{\Delta t^2}\right) + \delta\left(-\frac{t^2}{\Delta t} + \frac{t^3}{\Delta t^2}\right) \\
={}& \alpha + (\gamma - \alpha)\left(3\frac{t^2}{\Delta t^2} - 2\frac{t^3}{\Delta t^3}\right) + \beta\left(t - \frac{t^2}{\Delta t}\right) + (\beta + \delta)\left(-\frac{t^2}{\Delta t} + \frac{t^3}{\Delta t^2}\right)
\end{aligned}
$$

$$(\text{A.2})$$

It may be useful to know upper and lower bounds of $f(t)$ in the interval $[0, \Delta t]$, so one can decide whether it is necessary to proceed with the collision checking. To this end one can make use of the following facts,[1] which hold for arbitrary functions $g_k(t)$

$$\min\left(\sum_k g_k(t)\right) \geq \sum_k \min\left(g_k(t)\right)$$

and

$$\max\left(\sum_k g_k(t)\right) \leq \sum_k \max\left(g_k(t)\right). \qquad (\text{A.3})$$

---

1 In more mathematical terms, these equations can be derived from the triangle inequality using the uniform (or supremum) norm. For the present purpose the given simple form should suffice.

In this plot the third order polynomial interpolation for some arbitrary $\alpha, \beta, \gamma,$ and δ is shown. Also shown are the different versions of the upper and lower bounds, given by Equations (A.4) and (A.5)

Hence we can estimate the bounds by calculating the extrema of each term in Equation (A.2). Doing the math[2] and taking into account, that even if there is no extremum within the interval $(0, \Delta t)$ the function might be extremal at the interval's borders, one finally obtains the following two values as lower and upper bounds

$$\bar{f}_{\text{lwr}} = \min(\alpha, \gamma) + \min\left(0, \frac{1}{4}\beta\,\Delta t\right) + \min\left(-\frac{4}{27}(\beta + \delta)\Delta t, 0\right)$$

$$\bar{f}_{\text{upr}} = \max(\alpha, \gamma) + \max\left(0, \frac{1}{4}\beta\,\Delta t\right) + \max\left(-\frac{4}{27}(\beta + \delta)\Delta t, 0\right) \quad \text{(A.4)}$$

or another version (with different, but equally correct values)

$$\bar{\bar{f}}_{\text{lwr}} = \min(\alpha, \gamma) + \min\left(0, \frac{4}{27}\beta\,\Delta t\right) + \min\left(-\frac{4}{27}\delta\,\Delta t, 0\right)$$

$$\bar{\bar{f}}_{\text{upr}} = \max(\alpha, \gamma) + \max\left(0, \frac{4}{27}\beta\,\Delta t\right) + \max\left(-\frac{4}{27}\delta\,\Delta t, 0\right) \quad \text{(A.5)}$$

The two different versions stem from the two different representations of Equation (A.2). The above results are illustrated in Figure A.2.

A lower bound for the real particle distance in three dimensions can now be deduced from the above values. Therefore we want to use the relation $\min\left(f(t)^2\right) = \left[\min\left(f(t)\right)\right]^2$, which is valid if $f(t) \geq 0$ or $f(t) \leq 0$ in the whole domain. To circumvent the resulting problems, one needs to re-define $\bar{f}_{\text{lwr}}$ and $\bar{f}_{\text{upr}}$ in the following way

$$\text{if } \left(\bar{f}_{\text{lwr}}\bar{f}_{\text{upr}} < 0\right) \begin{Bmatrix} \bar{f}_{\text{upr}} = \max\left(|\bar{f}_{\text{lwr}}|, |\bar{f}_{\text{upr}}|\right) \\ \bar{f}_{\text{lwr}} = 0 \end{Bmatrix} \text{ else } \begin{Bmatrix} \bar{f}_{\text{upr}} = \bar{f}_{\text{upr}} \\ \bar{f}_{\text{lwr}} = \bar{f}_{\text{lwr}} \end{Bmatrix}.$$

With this re-definition a lower bound for the particle distance is given by (using Equation (A.3) again)

$$r_{\text{min}} = \left[\sum_i \min\left(\bar{f}^i_{\text{lwr}}\bar{f}^i_{\text{lwr}}, \bar{f}^i_{\text{upr}}\bar{f}^i_{\text{upr}}\right)\right]^{1/2}.$$

This estimate can be used in a code to decide if a more thorough check for a type II collision (see Appendix A.2) is needed. Equally the analogically defined estimate r_{max} can be used for type III collisions.

---

2 This means calculating the derivative of the function, finding the time(s) t^* for which this equals zero and, given $t^* \in [0, \Delta t]$, deducing the function's value at this point.

GIP INTEGRATORS

As discussed in Section 3.2.5 the particle velocity gradient tensor σ_{ij} can diverge when the nonlinear term in Equation (2.20) becomes dominant. Physically this is related to the formation of a caustic. Based on this interpretation Falkovich & Pumir (2007) developed a technique that allows to integrate σ_{ij} despite the singularities. They drew inspiration for their method from earlier work by Girimaji & Pope (1990). Here we present their approach as well as an alternative approach and compare them shortly.

B.1 PHYSICALLY INSPIRED APPROACH

The temporal evolution of the gradient tensor $\boldsymbol{\sigma}$ is given by Equation (2.20). Neglecting the time-dependance of A_{ij}, and limiting oneself to the one-dimensional case, this equation becomes

$$\dot{\sigma} = \frac{A - \sigma}{\tau_p} - \sigma^2.$$

If now σ becomes smaller than $-\tau_p^{-1}$ this equation is governed by the nonlinear term and its solution is $\sigma(t) = 1/(t - \tau_p)$. The local evolution of the particle density $n(t)$ is described by the equation

$$\dot{n}(t) = -n(t)\sigma(t),$$

which can now be solved as well. One obtains $n(t) = -n_0\tau_p/(\tau_p - t)$.

So the particle velocity gradient as well as the density diverge both in finite time. This, of course, is physically not possible. The maximal allowed particle density is one particle per volume of a particle, i.e., $1/a$. So the equations need to be regularized at the time t^* when this value is reached

$$n(t^*) = \frac{1}{a} = -\frac{\tau_p n_0}{\tau_p - t^*} \quad \Rightarrow \quad t^* = n_0 a + \tau_p.$$

This time also defines the maximal velocity gradient $\sigma(t^*) = (n_0 a \tau_p)^{-1}$. Assuming as a realistic value for the initial density $n_0 = 1/\eta$ one finally obtains the estimate from Falkovich & Pumir (2007), namely $\sigma_{\max} = \eta/(a\tau_p)$. If this value is reached the sign of σ has to be inverted. In physical terms this corresponds to a situation where the observed particle is overtaken by another particle.

In a three-dimensional system the scalar σ is replaced by the norm of the matrix $\|\boldsymbol{\sigma}\|$. The norm $\|\cdot\|$ is in principle the Euclidean norm $\|\cdot\|_2$, but in practice the Frobenius norm $\|\boldsymbol{\sigma}\| = [\sum_{i,j}|\sigma_{ij}|^2]^{1/2}$ is sufficient. When this norm reaches the maximal value $\eta/(a\tau_p)$ the signs of all components σ_{ij} should be flipped.
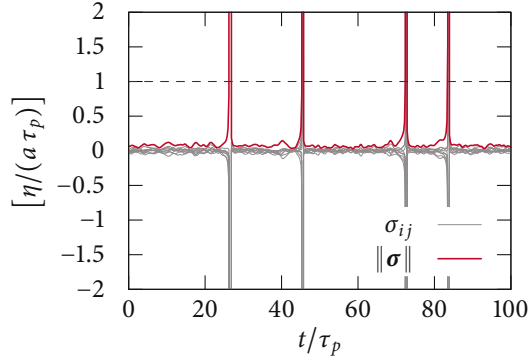
FIGURE B.1

This plot shows all components of the velocity gradient tensor σ_{ij} for one particle (thin shaded lines) as well as the norm of that tensor $\|\boldsymbol{\sigma}\|$ (thick line) obtained from a numerical simulation (KS). In this case $\|\boldsymbol{\sigma}\|$ was allowed to surpass the prescribed value of $\eta/(a\tau_p)$ (straight dashed line) by one order of magnitude.

We implemented this approach and show one short example trajectory in Figure B.1. In that case we allowed the norm of the particle velocity gradient tensor to be at most $\|\boldsymbol{\sigma}\| = 10\eta/(a\tau_p)$. As soon as it surpassed that value the signs of all components σ_{ij} were inverted. This example shows nicely that, as soon as the limiting value is exceeded, $\|\boldsymbol{\sigma}\|$ is bound to diverge. On the other hand the flipping of the signs of the components σ_{ij} makes sure that it returns to physical values.

B.1.1   *Shortcomings of the approach*

The sign-flipping method works quite good in simulations of the particle gradient tensor as can be seen in Figure B.1. It avoids getting infinite values and therefore assures successful numerical integration. However its results are not necessarily as precise as they could be. In his section we will explain some of the shortcomings of this technique and illustrate them in a simple example.

In Appendix B.1 a possible way to determine a physically sound maximal value at which the signs of the particle velocity gradient tensor $\boldsymbol{\sigma}$ should be inverted was derived. But in reality, no matter, how good the estimate of this maximal value, one will always flip the signs "too early". Consequently all following values of σ_{ij} will suffer from errors. This is impressively seen, if one tries this technique in a simple one-dimensional case with known solution, e.g.,

$$x'(t) = 1 + x(t)^2, \quad x(0) = 0 \qquad \Rightarrow \qquad x(t) = \tan(t) \qquad \text{(B.1)}$$

Now, if one tries to reproduce this result employing the sign-flipping technique, one will find that the determination of the first singularity's t-value is relatively exact. But the location of all subsequent singularities will vary with the choice of the maximal x at which its sign is changed, as well as with the time-step. Two cases are presented in Figure B.2. There, Equation (B.1) was integrated by a simple Euler scheme, employing two different techniques: The sign-flipping and a so-called *GIP integrator*. The latter will be discussed in Appendix B.2 and here we will only be concerned with the former. As in
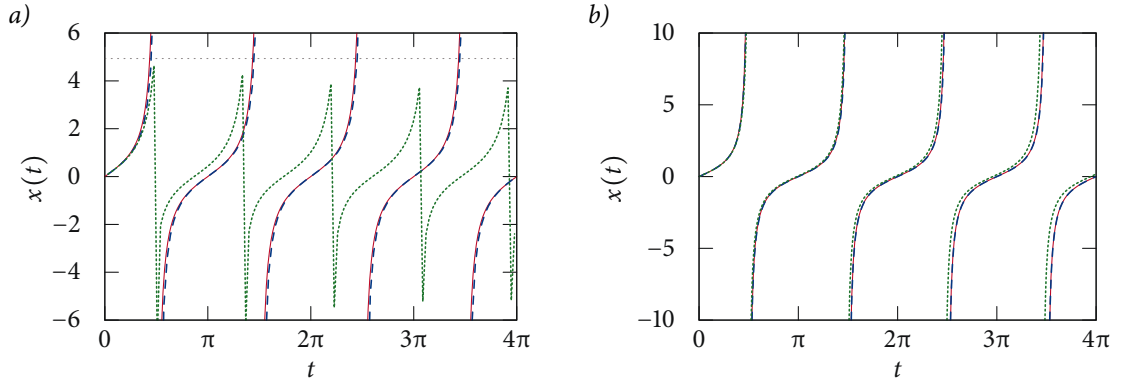
FIGURE B.2

Equation (B.1) has been integrated numerically with a simple Euler scheme. Here we compare the sign-flipping technique with the GIP integrator described in Appendix B.2. Full lines represent the exact solution $x(t) = \tan(t)$, dotted and dashed lines give the results from sign-flipping and the GIP scheme respectively. The straight dotted line gives the maximal value at which the sign of x was flipped [out of range in (b)].

this case the exact solution is known, it is possible to determine the "optimal" maximal value. It is given by the solution, two time-steps before a singularity is reached, i.e., in our case $\tan(\pi/2 - 2\Delta t)$. After the sign of x has been changed, it is as if the numerical integration would start anew with a new initial condition. The real solution however lags behind this initial condition by $2\Delta t$. The thusly generated offset increases at every singularity resulting in a delay between the numerical integration and the exact solution. This effect persists, of course, also for small time-steps as can be seen from Figure B.2b.

B.2   GIP INTEGRATORS

There are quite a few integrators that were developed for matrix Riccati equations like Equation (2.20). Most of them, as for example the Möbius scheme by Schiff & Shnider (1999), present a full specialized time-stepping method. But there is one interesting publication by Garrett & Li (2011), that provides a way to turn every ordinary Runge–Kutta method into an integrator that reliably integrates matrix Riccati equations and even steps over singularities in the solutions. Here we will discuss the basic ideas of this method on the basis of Equation (2.20). The interested reader is referred to Garrett & Li (2011) and Li & Kahan (2012) for details and mathematical proofs.

By the help of the Bernoulli substitution $\boldsymbol{\sigma} = \mathbf{P}_2\mathbf{P}_1^{-1}$, Equation (2.20) can be transformed into a linear homogeneous differential equation

$$\frac{\mathrm{d}}{\mathrm{d}t}\mathbf{P} = \mathbf{BP}, \qquad\qquad (\text{B.2})$$

where the 6×6 and 6×3 matrices

$$\mathbf{B} = \begin{pmatrix} \frac{1}{2\tau_p}\mathbf{I}_3 & \mathbf{I}_3 \\ \left[\frac{1}{\tau_p}\mathbf{A} + \beta\left(\frac{D}{Dt}\mathbf{A} + \mathbf{AA}\right)\right] & -\frac{1}{2\tau_p}\mathbf{I}_3 \end{pmatrix} \quad \text{and} \quad \mathbf{P} = \begin{pmatrix} \mathbf{P}_1 \\ \mathbf{P}_2 \end{pmatrix} \quad \text{(B.3)}$$

respectively, were introduced. Here $\mathbf{I}_3$ designates the 3×3 identity matrix.

Simply integrating Equation (B.2) may lead to numerical instabilities. But one has the freedom to scale the matrix $\mathbf{P}$ by any non-singular 3×3 matrix $\mathbf{M}$ in order to prevent these problems. Because $\mathbf{P}_2\mathbf{P}_1^{-1} = (\mathbf{P}_2\mathbf{M})(\mathbf{P}_1\mathbf{M})^{-1}$ such a scaling does not influence the results. In fact one may even rescale $\mathbf{P}$ at every time-step. Garrett & Li (2011) explain that $\mathbf{M} = \mathbf{P}_1^{-1}$ is an especially convenient choice.

These observations lead to the following recipe: Integrate Equation (B.2) with an ordinary Runge–Kutta scheme and regularly rescale $\mathbf{P}$ such that $\mathbf{P}_1 = \mathbf{I}_3$. Whenever necessary extract $\boldsymbol{\sigma}$ by calculating $\boldsymbol{\sigma} = \mathbf{P}_2\mathbf{P}_1^{-1}$.

Garrett & Li (2011) show that with this recipe one can simply step over all singularities without any further knowledge about the details. As can be seen in Figure B.2 it works correctly and especially it does not display the problem of shifted singularities, as discussed in Appendix B.1.1 We have implemented this technique in our code and the results shown in Chapter 8 were obtained with it. We also compared the two approaches—the GIP integrator and the sign-flipping—in our numerical simulations of particles entrained in a model flow. But we could not find any obvious differences. Probably the problem of the shifted singularities regularizes itself in a more complex environment. Nevertheless, the GIP integrator rests a convenient technique for integrating Equation (2.20).

LITERATURE CITED

This is the complete list of cited articles, books, and other resources. For the comfort of the reader I tried to include a digital object identifier (DOI) where possible. This should allow a stable (in time) access to articles published online. For other online resources, which do not have a DOI, like books that are freely available on the internet, I included a simple URL. These are however, unfortunately not guaranteed to persist for long times. Actually I noticed some already disappearing over the process of writing this manuscript. A good and usually successful practice in these situations, is to head to a web archiving service like the Wayback Machine (http://archive.org).

Abraham ER et al. (2000). "Importance of stirring in the development of an iron-fertilized phytoplankton." In: *Nature* 407, pp. 727–730. DOI: 10.1038/35037555 (cit. on p. 5).

Abrahamson J (1975). "Collision rates of small particles in a vigorously turbulent fluid." In: *Chem. Eng. Sci.* 30, pp. 1371–1379. DOI: 10.1016/0009-2509(75)85067-6 (cit. on pp. xviii, 24, 25, 28, 29, 66, 67).

Allen MP, Tildesley DJ (1989). *Computer Simulation of Liquids*. Oxford: Clarendon Press (cit. on p. 35).

Andersson B, Gustavsson K, Mehlig B, Wilkinson M (2007). "Advective collisions." In: *EPL* 80, p. 69001. DOI: 10.1209/0295-5075/80/69001 (cit. on pp. 30, 31, 50, 64).

Argyris J, Faust G, Haase M, Friedrich R (2010). *Die Erforschung des Chaos: Eine Einführung in die Theorie nichtlinearer Systeme*. 2nd ed. Heidelberg: Springer (cit. on p. 8).

Ayala O, Grabowski WW, Wang L-P (2007). "A hybrid approach for simulating turbulent collisions of hydrodynamically-interacting particles." In: *J. Comput. Phys.* 225, pp. 51–73. DOI: 10.1016/j.jcp.2006.11.016 (cit. on p. 64).

Ayala O, Rosa B, Wang L-P (2008). "Effects of turbulence on the geometric collision rate of sedimenting droplets. Part 2. Theory and parameterization." In: *New J. Phys.* 10, p. 075016. DOI: 10.1088/1367-2630/10/7/075016 (cit. on p. 21). Corrigendum in: *New J. Phys.* 10 (2008), p. 099802. DOI: 10.1088/1367-2630/10/9/099802.

Bakunin O (2008). *Turbulence and Diffusion: Scaling Versus Equations*. Springer complexity. Springer-Verlag Berlin Heidelberg (cit. on p. 50).

Balachandar S, Eaton JK (2010). "Turbulent Dispersed Multiphase Flow." In: *Annu. Rev. Fluid Mech.* 42, pp. 111–133. DOI: 10.1146/annurev.fluid.010908.165243 (cit. on p. 5).

Basset AB (1888). *A treatise on hydrodynamics, with numerous examples*. Vol. 2. Cambridge: Deighton, Bell and Co. URL: http://archive.org/details/atreatiseonhydro2bassgoog (cit. on p. 16).

Batchelor GK (1959). *The Theory of Homogeneous Turbulence*. Cambridge University (cit. on p. 9).

Batchelor GK (1953). *The theory of homogenous turbulence*. Cambridge University Press (cit. on pp. 11, 44).

Beard KV, Ochs HT (1993). "Warm-Rain Initiation: An Overview of Microphysical Mechanisms." In: *J. Appl. Meteor.* 32, pp. 608–625. DOI: 10.1175/1520-0450(1993)032<0608:WRIAOO>2.0.CO;2 (cit. on p. 19).

Bec J, Biferale L, Cencini M, Lanotte AS, Toschi F (2010). "Intermittency in the velocity distribution of heavy particles in turbulence." In: *J. Fluid Mech.* 646, pp. 527–536. DOI: 10.1017/S0022112010000029 (cit. on pp. 47, 71).

Bec J, Celani A, Cencini M, Musacchio S (2005). "Clustering and collisions of heavy particles in random smooth flows." In: *Phys. Fluids* 17, p. 073301. DOI: 10.1063/1.1940367 (cit. on pp. 21, 47).

Bec J (2005). "Multifractal concentrations of inertial particles in smooth random flows." In: *J. Fluid Mech.* 528, pp. 255–277. DOI: 10.1017/S0022112005003368 (cit. on p. 31).

Bec J et al. (2006). "Lyapunov exponents of heavy particles in turbulence." In: *Phys. Fluids* 18, p. 091702. DOI: 10.1063/1.2349587 (cit. on p. 53).

Bec J et al. (2007). "Heavy Particle Concentration in Turbulence at Dissipative and Inertial Scales." In: *Phys. Rev. Lett.* 98, p. 084502. DOI: 10.1103/PhysRevLett.98.084502 (cit. on p. 47).

Beckwith SVW, Henning T, Nakagawa Y (2000). "Dust Properties and Assembly of Large Particles in Protoplanetary Disks." In: *Protostars and Planets IV*. Ed. by V Mannings, AP Boss, S Russell. The University of Arizona Press. URL: http://www.uapress.arizona.edu/onlinebks/PPIV/contents.php (cit. on p. 22).

Berry EX, Reinhardt RL (1974a). "An Analysis of Cloud Drop Growth by Collection: Part I. Double Distributions." In: *J. Atmos. Sci.* 31, pp. 1814–1824. DOI: 10.1175/1520-0469(1974)031<1814:AAOCDG>2.0.CO;2 (cit. on p. 20).

——(1974b). "An Analysis of Cloud Drop Growth by Collection Part II. Single Initial Distributions." In: *J. Atmos. Sci.* 31, pp. 1825–1831. DOI: 10.1175/1520-0469(1974)031<1825:AAOCDG>2.0.CO;2 (cit. on p. 20).

Berry MV (1981). "Singularities in Waves and Rays." In: *Physique des défauts: Physics of defects*. Ed. by R Balian, M Kléman, J Poirier. Les Houches Session XXXV. North-Holland, Amsterdam, pp. 453–543. URL: http://www.phy.bris.ac.uk/people/berry_mv/publications.html (cit. on p. 28).

Bewley GP, Saw E, Bodenschatz E (2013). "Observation of the sling effect." In: *New J. Phys.* 15, p. 083051. DOI: 10.1088/1367-2630/15/8/083051 (cit. on p. 28).

Bitane R, Homann H, Bec J (2012). "Time scales of turbulent relative dispersion." In: *Phys. Rev. E* 86, p. 045302. DOI: 10.1103/PhysRevE.86.045302 (cit. on p. 4).

Blyth AM (1993). "Entrainment in Cumulus Clouds." In: *J. Appl. Meteor.* 32, pp. 626–641. DOI: 10.1175/1520-0450(1993)032<0626:EICC>2.0.CO;2 (cit. on p. 19).

Bodenschatz E, Malinowski SP, Shaw RA, Stratmann F (2010). "Can We Understand Clouds Without Turbulence?" In: *Science* 327, pp. 970–971. DOI: 10.1126/science.1185138 (cit. on p. 19).

Bodenschatz E, Eckert M (2011). "Prandtl and the Göttingen school." In: *A Voyage Through Turbulence*. Ed. by PA Davidson, Y Kaneda, K Moffatt, KR Sreenivasan. Cambridge Univ. Press, Oct. 2011, pp. 40–100 (cit. on p. 10). Draft avail. in: *ArXiv e-prints* (July 2011). arXiv: 1107.4729 [physics.flu-dyn].

Boussinesq J (1885). "Sur la résistance qu'oppose un fluide indéfini au repos, sans pesanteur, au mouvement varié d'une sphère solide qu'il mouille sur toute sa surface, quand les vitesses restent bien continues et assez faibles pour que leurs carrés et produits soient négligeables." French. In: *C. R. Acad. Sci.* 100, pp. 935–937. URL: http://gallica.bnf.fr/ark:/12148/bpt6k3056t (cit. on p. 16).

Boyd JP (2001). *Chebyshev and Fourier Spectral Methods*. 2nd ed. New York: Dover Publications. URL: http://www-personal.umich.edu/~jpboyd/BOOK_Spectral2000.html (cit. on p. 43).

Brunk BK, Koch DL, Lion LW (1998a). "Observations of coagulation in isotropic turbulence." In: *J. Fluid Mech.* 371, pp. 81–107. DOI: 10.1017/S0022112098002183 (cit. on p. 31).

——(1998b). "Turbulent coagulation of colloidal particles." In: *J. Fluid Mech.* 364, pp. 81–113. DOI: 10.1017/S0022112098001037 (cit. on pp. 31, 50).

Calzavarini E et al. (2009). "Acceleration statistics of finite-sized particles in turbulent flow: the role of Faxén forces." In: *J. Fluid Mech.* 630, pp. 179–189. DOI: 10.1017/S0022112009006880 (cit. on p. 43).

Capelo H, Xu H, Lambrechts M, Johansen A, Bodenschatz E (2013). *Studies of gas-particle interaction: Implications for the streaming instability in protoplanetary disks.* Talk given at the European Turbulence Conference 14, 1–4 September 2013, Lyon, France (cit. on p. 23).

Carneiro MV, Araújo NAM, Pähtz T, Herrmann HJ (2013). "Midair Collisions Enhance Saltation." In: *Phys. Rev. Lett.* 111, p. 058001. DOI: 10.1103/PhysRevLett.111.058001 (cit. on p. 5).

Carpenter MH, Kennedy CA (1994). *Fourth-order 2N-storage Runge–Kutta schemes.* NASA Technical Memorandum 109112. NASA (cit. on p. 74).

Chareyron D et al. (2012). "Testing an in-line digital holography 'inverse method' for the Lagrangian tracking of evaporating droplets in homogeneous nearly isotropic turbulence." In: *New J. Phys.* 14, p. 043039. DOI: 10.1088/1367-2630/14/4/043039 (cit. on p. 5).

Chong MS, Perry AE, Cantwell BJ (1990). "A general classification of three-dimensional flow fields." In: *Phys. Fluids A* 2, pp. 765–777. DOI: 10.1063/1.857730 (cit. on p. 31).

Chumakov S (2012). *Homogeneous Isotropic Turbulence in 3D (incompressible).* Comp. software. Version r115. July 2012. URL: http://hit3d.googlecode.com/ (cit. on p. 43).

Comte-Bellot G, Corrsin S (1971). "Simple Eulerian time correlation of full-and narrow-band velocity signals in grid-generated, turbulence." In: *J. Fluid Mech.* 48, pp. 273–337. DOI: 10.1017/S0022112071001599 (cit. on pp. 15, 16, 43, 44).

Courant R, Friedrichs K, Lewy H (1928). "Über die partiellen Differenzengleichungen der mathematischen Physik." German. In: *Math. Ann.* 100, pp. 32–74. URL: http://resolver.sub.uni-goettingen.de/purl?GDZPPN002272636 (cit. on p. 43). Trans. as "On the Partial Difference Equations of Mathematical Physics." In: *IBM J. Res. Dev.* 11, pp. 215–234. DOI: 10.1147/rd.112.0215.

da Vinci L (c. 1508–1509). *Studies of Water passing Obstacles and falling.* Retrieved from the internet. URL: http://commons.wikimedia.org/w/index.php?title=File:Studies_of_Water_passing_Obstacles_and_falling.jpg&oldid=70966304 (visited on 08/01/2013) (cit. on p. 10).

Daitche A, Tél T (2011). "Memory Effects are Relevant for Chaotic Advection of Inertial Particles." In: *Phys. Rev. Lett.* 107, p. 244501. DOI: 10.1103/PhysRevLett.107.244501 (cit. on p. 17).

Devenish BJ et al. (2012). "Droplet growth in warm turbulent clouds." In: *Q. J. R. Meteorol. Soc.* 138, pp. 1401–1429. DOI: 10.1002/qj.1897 (cit. on pp. 19, 20).

Ducasse L (2009). "Mouvements collectifs de particules en turbulence : collisions et concentration préférentielle." French. Thèse pour obtenir le titre de Docteur en Sciences. Universitée de Nice-Sophia Antipolis, Dec. 2009 (cit. on pp. 32, 74).

Ducasse L, Pumir A (2009). "Inertial particle collisions in turbulent synthetic flows: Quantifying the sling effect." In: *Phys. Rev. E* 80, p. 066312. DOI: 10.1103/PhysRevE.80.066312 (cit. on pp. 30, 65, 74, 79).

Duncan K, Mehlig B, Östlund S, Wilkinson M (2005). "Clustering by Mixing Flows." In: *Phys. Rev. Lett.* 95, p. 240602. DOI: 10.1103/PhysRevLett.95.240602 (cit. on p. 29).

Falkovich G, Fouxon A, Stepanov MG (2002). "Acceleration of rain initiation by cloud turbulence." In: *Nature* 419, pp. 151–154. DOI: 10.1038/nature00983 (cit. on pp. 28, 29, 65).

Falkovich G, Malinowski SP (2008). "Focus on Cloud Physics (Editorial)." In: *New J. Phys.* 10, p. 075012. DOI: 10.1088/1367-2630/10/7/075012 (cit. on p. 19).

Falkovich G, Pumir A (2004). "Intermittent distribution of heavy particles in a turbulent flow." In: *Phys. Fluids* 16, pp. L47–L50. DOI: 10.1063/1.1755722 (cit. on p. 30).

——(2007). "Sling Effect in Collisions of Water Droplets in Turbulent Clouds." In: *J. Atmos. Sci.* 64, pp. 4497–4505. DOI: 10.1175/2007JAS2371.1 (cit. on pp. 29, 30, 87).

Faxén H (1922). "Der Widerstand gegen die Bewegung einer starren Kugel in einer zähen Flüssigkeit, die zwischen zwei parallelen ebenen Wänden eingeschlossen ist." In: *Ann. Phys.* 373, pp. 89–119. DOI: 10.1002/andp.19223731003 (cit. on p. 16).

Ferner MC, Weissburg MJ (2005). "Slow-moving predatory gastropods track prey odors in fast and turbulent flow." In: *J. Exp. Biol.* 208, pp. 809–819. DOI: 10.1242/jeb.01438 (cit. on p. 5).

Février P, Simonin O, Squires KD (2005). "Partitioning of particle velocities in gas–solid turbulent flows into a continuous field and a spatially uncorrelated random distribution: theoretical formalism and numerical study." In: *J. Fluid Mech.* 533, pp. 1–46. DOI: 10.1017/S0022112005004088 (cit. on pp. 28, 30).

Friedrich R (2007). "Turbulenz." Lecture notes taken in a course during winter semester 2007/08 at Westfälische Wilhelms-Universität Münster (cit. on p. 8).

Frisch U, Bec J (2001). "Burgulence." In: *New trends in turbulence. Turbulence: nouveaux aspects.* Ed. by M Lesieur, A Yaglom, F David. Vol. 74. Les Houches – École d'Été de Physique Théorique. Springer Berlin Heidelberg, pp. 341–383. DOI: 10.1007/3-540-45674-0_7 (cit. on p. 28).

Frisch U (1996). *Turbulence: The Legacy of A. N. Kolmogorov.* Cambridge University Press, Jan. 1996 (cit. on pp. 8, 9, 12, 14).

Fung JCH, Hunt JCR, Malik NA, Perkins RJ (1992). "Kinematic simulation of homogeneous turbulence by unsteady random Fourier modes." In: *J. Fluid Mech.* 236, pp. 281–318. DOI: 10.1017/S0022112092001423 (cit. on p. 73).

Fung JCH, Vassilicos JC (1998). "Two-particle dispersion in turbulentlike flows." In: *Phys. Rev. E* 57, pp. 1677–1690. DOI: 10.1103/PhysRevE.57.1677 (cit. on p. 74).

Garrett CK, Li R (2011). *GIP Integrators for Matrix Riccati Differential Equations.* Mathematics Preprint Series 5. The University of Texas Arlington. URL: http://www.uta.edu/math/preprint/rep2011_05.pdf (cit. on pp. 89, 90).

Gatignol R (1983). "Faxen Formulae for a Rigid Particle in an Unsteady Non-uniform Stokes Flow." In: *J. Méc. Théor. Appl.* 1, pp. 143–160 (cit. on p. 16).

Girimaji SS, Pope SB (1990). "Material-element deformation in isotropic turbulence." In: *J. Fluid Mech.* 220, pp. 427–458. DOI: 10.1017/S0022112090003330 (cit. on p. 87).

Gottlieb S, Shu C, Tadmor E (2001). "Strong Stability-Preserving High-Order Time Discretization Methods." In: *SIAM Rev.* 43, pp. 89–112. DOI: 10.1137/S003614450036757X (cit. on p. 74).

Grabowski WW, Wang L-P (2009). "Diffusional and accretional growth of water drops in a rising adiabatic parcel: effects of the turbulent collision kernel." In: *Atmos. Chem. Phys.* 9, pp. 2335–2353. DOI: 10.5194/acp-9-2335-2009 (cit. on p. 72).

Grabowski WW, Vaillancourt P (1999). "Comments on 'Preferential Concentration of Cloud Droplets by Turbulence: Effects on the Early Evolution of Cumulus

Cloud Droplet Spectra'." In: *J. Atmos. Sci.* 56, pp. 1433–1436. DOI: 10.1175/ 1520-0469(1999)056<1433:COPCOC>2.0.CO;2 (cit. on pp. 22, 64).

Grabowski WW, Wang L-P (2013). "Growth of Cloud Droplets in a Turbulent Environment." In: *Annu. Rev. Fluid Mech.* 45, pp. 293–324. DOI: 10.1146/ annurev-fluid-011212-140750 (cit. on pp. 19, 20, 22). Erratum in: *Annu. Rev. Fluid Mech.* DOI: 10.1146/annurev-fl-45-021013-200001.

Grassberger P, Procaccia I (1983). "Characterization of Strange Attractors." In: *Phys. Rev. Lett.* 50, pp. 346–349. DOI: 10.1103/PhysRevLett.50.346 (cit. on p. 47).

Gustavsson K, Mehlig B (2011a). "Distribution of relative velocities in turbulent aerosols." In: *Phys. Rev. E* 84, p. 045304. DOI: 10.1103/PhysRevE.84.045304 (cit. on pp. 64, 65, 71).

——(2011b). "Ergodic and non-ergodic clustering of inertial particles." In: *EPL* 96, p. 60012. DOI: 10.1209/0295-5075/96/60012 (cit. on p. 26).

——(2013a). "Collisions and recollisions of identical inertial particles in random velocity fields." In: *ArXiv e-prints* (Sept. 2013). DOI: http://arxiv.org/abs/1307. 0462 (cit. on pp. 50, 64).

——(2013b). "Relative velocities of inertial particles in turbulent aerosols." In: *ArXiv e-prints* (July 2013). arXiv: 1307.0462 [physics.flu-dyn] (cit. on pp. 64, 71).

Gustavsson K, Mehlig B, Wilkinson M (2008). "Collisions of particles advected in random flows." In: *New J. Phys.* 10, p. 075014. DOI: 10.1088/1367-2630/10/7/ 075014 (cit. on p. 30).

Gustavsson K, Meneguz E, Reeks M, Mehlig B (2012). "Inertial-particle dynamics in turbulent flows: caustics, concentration fluctuations and random uncorrelated motion." In: *New J. Phys.* 14, p. 115017. DOI: 10.1088/1367-2630/14/11/ 115017 (cit. on p. 30).

Hackl JF, Yeung PK, Sawford BL (2011). "Multi-particle and tetrad statistics in numerical simulations of turbulent relative dispersion." In: *Phys. Fluids* 23, p. 065103. DOI: 10.1063/1.3586803 (cit. on p. 4).

Haynes W, ed. (2012). *CRC Handbook of Chemistry and Physics 2012–2013.* 93rd ed. CRC Handbook of Chemistry and Physics. Boca Raton, FL: CRC Press (cit. on pp. 21, 22).

Heisenberg W (1948). "Zur statistischen Theorie der Turbulenz." In: *Z. Phys.* 124, pp. 628–657. DOI: 10.1007/BF01668899 (cit. on p. 15).

IJzermans RHA, Meneguz E, Reeks MW (2010). "Segregation of particles in incompressible random flows: singularities, intermittency and random uncorrelated motion." In: *J. Fluid Mech.* 653, pp. 99–136. DOI: 10.1017/S0022112010000170 (cit. on p. 30).

Ishihara T, Kaneda Y, Yokokawa M, Itakura K, Uno A (2007). "Small-scale statistics in high-resolution direct numerical simulation of turbulence: Reynolds number dependence of one-point velocity gradient statistics." In: *J. Fluid Mech.* 592, pp. 335–366. DOI: 10.1017/S0022112007008531 (cit. on p. 4).

Johansen A et al. (2007). "Rapid planetesimal formation in turbulent circumstellar disks." In: *Nature* 448, pp. 1022–1025. DOI: 10.1038/nature06086 (cit. on p. 22).

Jonas PR (1996). "Turbulence and cloud microphysics." In: *Atmos. Res.* 40, pp. 283–306. DOI: 10.1016/0169-8095(95)00035-6 (cit. on p. 19).

Jørgensen JB, Mann J, Ott S, Pécseli HL, Trulsen J (2005). "Experimental studies of occupation and transit times in turbulent flows." In: *Phys. Fluids* 17, p. 035111. DOI: 10.1063/1.1863259 (cit. on p. 41).

Jullien M-C, Paret J, Tabeling P (1999). "Richardson Pair Dispersion in Two-Dimensional Turbulence." In: *Phys. Rev. Lett.* 82, pp. 2872–2875. DOI: 10.1103/PhysRevLett.82.2872 (cit. on p. 52).

Kaneda Y, Ishihara T, Yokokawa M, Itakura K, Uno A (2003). "Energy dissipation rate and energy spectrum in high resolution direct numerical simulations of turbulence in a periodic box." In: *Phys. Fluids* 15, pp. L21–L24. DOI: 10.1063/1.1539855 (cit. on p. 4).

Kennel MB (2004). "KDTREE 2: Fortran 95 and C++ software to efficiently search for near neighbors in a multi-dimensional Euclidean space." In: *ArXiv e-prints* (Aug. 2004). arXiv: physics/0408067 [physics.data-an] (cit. on p. 36).

Kepkay P (2000). "Colloids and the Ocean Carbon Cycle." In: *Marine Chemistry*. Ed. by P Wangersky. Vol. 5D. The Handbook of Environmental Chemistry. Springer Berlin Heidelberg, pp. 35–56. DOI: 10.1007/10683826_2 (cit. on p. 5).

Khain A et al. (2007). "Critical comments to results of investigations of drop collisions in turbulent clouds." In: *Atmos. Res.* 86, pp. 1–20. DOI: 10.1016/j.atmosres.2007.05.003 (cit. on p. 22).

Kitchen M, Caughey SJ (1981). "Tethered-balloon observations of the structure of small cumulus clouds." In: *Q. J. R. Meteorol. Soc.* 107, pp. 853–874. DOI: 10.1002/qj.49710745407 (cit. on p. 21).

Kolmogorov AN (1941). "The Local Structure of Turbulence in Incompressible Viscous Fluid for Very Large Reynolds Numbers." In: *Dokl. Akad. Nauk SSSR* 30.4 (cit. on pp. 14, 15). Trans. from the Russian by V Levin. In: *Proc. R. Soc. London Ser. A* 434 (1991), pp. 9–13. DOI: 10.1098/rspa.1991.0075.

Krstulovic G, Cencini M, Bec J (2013). "Effective Rates in Dilute Reaction-Advection Systems for the Annihilation Process $A + A \to \varnothing$." In: *J. Stat. Phys.* 153, pp. 530–550. DOI: 10.1007/s10955-013-0823-8 (cit. on p. 58).

Lamorgese AG, Caughey DA, Pope SB (2005). "Direct numerical simulation of homogeneous turbulence with hyperviscosity." In: *Phys. Fluids* 17, p. 015106. DOI: 10.1063/1.1833415 (cit. on p. 43).

Landau LD, Lifshitz EM (1987). *Fluid Mechanics: Vol 6 (Course of Theoretical Physics)*. 2nd ed. Pergamon Press (cit. on p. 11).

Lesieur M (1997). *Turbulence in Fluids*. 3ed. Kluwer Academic Publishers (cit. on p. 13).

Lewis DM, Pedley TJ (2000). "Planktonic Contact Rates in Homogeneous Isotropic Turbulence: Theoretical Predictions and Kinematic Simulations." In: *J. Theor. Biol.* 205, pp. 377–408. DOI: 10.1006/jtbi.2000.2073 (cit. on p. 5).

Li R, Kahan W (2012). "A family of Anadromic numerical methods for matrix Riccati differential equations." In: *Math. Comp.* 81, pp. 233–265. DOI: 10.1090/S0025-5718-2011-02498-1 (cit. on p. 89).

MacKay DJC (2009). *Sustainable Energy – without the hot air*. 3rd ed. Cambridge: UIT. URL: http://www.withouthotair.com (cit. on p. 3).

Mafra-Neto A, Carde RT (1994). "Fine-scale structure of pheromone plumes modulates upwind orientation of flying moths." In: *Nature* 369, pp. 142–144. DOI: 10.1038/369142a0 (cit. on p. 5).

Malik NA, Vassilicos JC (1999). "A Lagrangian model for turbulent dispersion with turbulent-like flow structure: Comparison with direct numerical simulation for two-particle statistics." In: *Phys. Fluids* 11, pp. 1572–1580. DOI: 10.1063/1.870019 (cit. on p. 74).

Matsumoto M, Nishimura T (1998). "Mersenne twister: a 623-dimensionally equidistributed uniform pseudo-random number generator." In: *ACM Trans. Model. Comput. Simul.* 8, pp. 3–30. DOI: 10.1145/272991.272995 (cit. on p. 74).

Maxey MR (1987). "The gravitational settling of aerosol particles in homogeneous turbulence and random flow fields." In: *J. Fluid Mech.* 174, pp. 441–465. DOI: 10.1017/S0022112087000193 (cit. on pp. 25, 26, 28).

Maxey MR, Riley JJ (1983). "Equation of motion for a small rigid sphere in a nonuniform flow." In: *Phys. Fluids* 26, pp. 883–889. DOI: 10.1063/1.864230 (cit. on p. 16).

McComb WD (1992). *The Physics of Fluid Turbulence (Oxford Engineering Science Series, 25).* Oxford University Press, USA, Mar. 1992 (cit. on p. 12).

McQuarrie D (1976). *Statistical Mechanics.* New York: Harper & Row (cit. on p. 26).

Mehlig B, Uski V, Wilkinson M (2007). "Colliding particles in highly turbulent flows." In: *Phys. Fluids* 19, p. 098107. DOI: 10.1063/1.2768931 (cit. on pp. 25, 66).

Meneguz E, Reeks MW (2011). "Statistical properties of particle segregation in homogeneous isotropic turbulence." In: *J. Fluid Mech.* 686, pp. 338–351. DOI: 10.1017/jfm.2011.333 (cit. on p. 30).

Moffatt HK (1981). "Some developments in the theory of turbulence." In: *J. Fluid Mech.* 106, pp. 27–47. DOI: 10.1017/S002211208100150X (cit. on p. 8).

Moody EG, Collins LR (2003). "Effect of Mixing on the Nucleation and Growth of Titania Particles." In: *Aerosol. Sci. Tech.* 37, pp. 403–424. DOI: 10.1080/02786820300979 (cit. on p. 5).

Moore WJ (1972). *Physical Chemistry.* 4th. Prentice-Hall chemistry series. Prentice-Hall, p. 1458. URL: http://www.archive.org/details/physicalchemistr029701mbp (cit. on p. 23).

Navier CLMH (1823). "Mémoire sur les lois du mouvement des fluides." In: *Mem. Acad. Sci. Inst. Fr.* 6, pp. 389–440. URL: http://gallica.bnf.fr/ark:/12148/bpt6k3221x.image.f577 (cit. on p. 7).

Nicolleau FCGA, ElMaihy A (2004). "Study of the development of three-dimensional sets of fluid particles and iso-concentration fields using kinematic simulation." In: *J. Fluid Mech.* 517, pp. 229–249. DOI: 10.1017/S0022112004000898 (cit. on p. 74).

Obukhov AM (1941). "On the distribution of energy in the spectrum of turbulent flow." In: *Dokl. Akad. Nauk SSSR* 32.1 (cit. on p. 15).

ONERA (2009). *Photograph of a Citroën DS in a wind tunnel.* Retrieved from the internet. URL: http://www.onera.fr/images-science/tunnel-hydrodynamique/images/ds-aerodynamique-ds19.jpg (visited on 04/06/2013) (cit. on p. 3).

Onsager L (1945). "The Distribution of Energy in Turbulence." In: *Phys. Rev.* 68. Abstract, p. 286. DOI: 10.1103/PhysRev.68.281 (cit. on p. 15).

——(1949). "Statistical Hydrodynamics." English. In: *Nuovo Cimento Suppl.* 6, pp. 279–287. DOI: 10.1007/BF02780991 (cit. on p. 15).

Orszag SA (1971). "On the Elimination of Aliasing in Finite-Difference Schemes by Filtering High-Wavenumber Components." In: *J. Atmos. Sci.* 28, pp. 1074–1074. DOI: 10.1175/1520-0469(1971)028<1074:OTEOAI>2.0.CO;2 (cit. on p. 43).

——(1977). "Lectures on the Statistical Theory of Turbulence." In: *Fluid Dynamics 1973.* Les Houches Summer School of Theoretical Physics. Ed. by R Balian, J Peube. New York: Gordon and Breach, pp. 237–374 (cit. on p. 13).

Oseen CW (1927). *Neuere Methoden und Ergebnisse in der Hydrodynamik.* German. Vol. 1. Mathematik und ihre Anwendungen in Monographien und Lehrbüchern. Leipzig: Akademische Verlagsgesellschaft m. b. H. (cit. on p. 16).

Pan L, Padoan P, Scalo J, Kritsuk AG, Norman ML (2011). "Turbulent Clustering of Protoplanetary Dust and Planetesimal Formation." In: *ApJ* 740, p. 6. DOI: 10.1088/0004-637X/740/1/6 (cit. on p. 22).

Pinsky MB, Khain AP (1997). "Turbulence effects on droplet growth and size distribution in clouds–A review." In: *J. Aerosol Sci.* 28, pp. 1177–1214. DOI: 10.1016/S0021-8502(97)00005-0 (cit. on pp. 19, 22).

Pope SB (2000). *Turbulent Flows*. 1st. Cambridge University Press, Jan. 2000 (cit. on pp. 9, 11, 12, 22, 25).

Post SL, Abraham J (2002). "Modeling the outcome of drop-drop collisions in Diesel sprays." In: *Int. J. Multiphase Flow* 28, pp. 997–1019. DOI: 10.1016/S0301-9322(02)00007-1 (cit. on p. 5).

Press WH, Teukolsky SA, Vetterling WT, Flannery BP (2007). *Numerical Recipes: The Art of Scientific Computing*. 3rd ed. Cambridge University Press (cit. on p. 44).

Pruppacher H, Klett J (1997). *Microphysics of Clouds and Precipitation*. Atmospheric and oceanographic sciences library. Kluwer Academic Publishers (cit. on pp. 22, 31).

Rast MP, Pinton J-F (2011). "Pair Dispersion in Turbulence: The Subdominant Role of Scaling." In: *Phys. Rev. Lett.* 107, p. 214501. DOI: 10.1103/PhysRevLett.107.214501 (cit. on p. 52).

Reade WC, Collins LR (2000). "Effect of preferential concentration on turbulent collision rates." In: *Phys. Fluids* 12, pp. 2530–2540. DOI: 10.1063/1.1288515 (cit. on pp. 30, 46).

Reeks MW, Fabbro L, Soldati A (2006). "In search of random uncorrelated particle motion (RUM) in a simple random flow field." In: *Proc. 2006 ASME Joint US European Fluids Engineering Summer Meeting.* (July 17–20, 2006). Miami, FL, pp. 1755–1762 (cit. on pp. 28, 30).

Reynolds O (1883). "An Experimental Investigation of the Circumstances Which Determine Whether the Motion of Water Shall Be Direct or Sinuous, and of the Law of Resistance in Parallel Channels." In: *Phil. Trans. R. Soc.* 174, pp. 935–982. URL: http://www.jstor.org/stable/109431 (cit. on pp. 8, 9).

Richardson LF (1922). *Weather prediction by numerical process.* Cambridge: Cambridge Univ. Press, p. 236. URL: http://archive.org/details/weatherpredictiooorichrich (cit. on p. 9).

Rickels W et al. (2011). *Large-Scale Intentional Interventions into the ClimateSystem? Assessing the Climate Engineering Debate.* Scoping report conducted on behalf of the German Federal Ministry of Education and Research (BMBF). Kiel Earth Institute, Kiel. URL: http://www.kiel-earth-institute.de/scoping-report-climate-engineering.html (cit. on p. 19).

Robertson HP (1940). "The invariant theory of isotropic turbulence." In: *Math. Proc. Cambridge.* 36, pp. 209–223. DOI: 10.1017/S0305004100017199 (cit. on p. 11).

Rosa B, Parishani H, Ayala O, Grabowski WW, Wang L-P (2013). "Kinematic and dynamic collision statistics of cloud droplets from high-resolution simulations." In: *New J. Phys.* 15, p. 045032. DOI: 10.1088/1367-2630/15/4/045032 (cit. on pp. 21, 28, 47, 48, 71, 72).

Rothschild B, Osborn T (1988). "Small-scale turbulence and plankton contact rates." In: *J. Plankton Res.* 10, pp. 465–474. DOI: 10.1093/plankt/10.3.465 (cit. on p. 5).

Sachs L, Hedderich J (2006). *Angewandte Statistik – Methodensammlung mit R.* Zwölfte, vollständig neu bearbeitete Auflage. Springer Berlin Heidelberg, p. 702. DOI: 10.1007/978-3-540-32161-3 (cit. on p. 37).

Saffman PG (1992). *Vortex dynamics*. 1st pbk. ed., with corrections. Cambridge monographs on mechanics and applied mathematics. Cambridge: Cambridge University Press, p. 311. URL: http://www.loc.gov/catdir/toc/cam024/95138986.html (cit. on p. 8).

Saffman PG, Turner JS (1956). "On the collision of drops in turbulent clouds." In: *J. Fluid Mech.* 1, pp. 16–30. DOI: 10.1017/S0022112056000020 (cit. on pp. xix, 23–25, 27–32, 66, 67, 71, 75, 83). Corrigendum in: *J. Fluid Mech.* 196 (1988), pp. 599–599. DOI: 10.1017/S002211208800285X.

Safranov V (1972). *Evolution of the Protoplanetary Cloud and Formation of the Earth and the Planets*. Trans. from the Russian by Israel Program for Scientific Translations. Jerusalem: Keter Press. URL: http://www.archive.org/details/nasa_techdoc_19720019068 (cit. on pp. 5, 22).

Scatamacchia R, Biferale L, Toschi F (2012). "Extreme Events in the Dispersions of Two Neighboring Particles Under the Influence of Fluid Turbulence." In: *Phys. Rev. Lett.* 109, p. 144501. DOI: 10.1103/PhysRevLett.109.144501 (cit. on p. 52).

Schiff J, Shnider S (1999). "A Natural Approach to the Numerical Integration of Riccati Differential Equations." In: *SIAM J. Numer. Anal.* 36, pp. 1392–1413. DOI: 10.1137/S0036142996307946 (cit. on p. 89).

Shariff K (2009). "Fluid Mechanics in Disks Around Young Stars*." In: *Annu. Rev. Fluid Mech.* 41, pp. 283–315. DOI: 10.1146/annurev.fluid.010908.165144 (cit. on p. 22).

Shaw RA (2003). "Particle-Turbulence Interactions in Atmospheric Clouds." In: *Annu. Rev. Fluid Mech.* 35, pp. 183–227. DOI: 10.1146/annurev.fluid.35.101101.161125 (cit. on pp. 5, 19, 20).

Siebert H, Shaw RA, Warhaft Z (2010). "Statistics of Small-Scale Velocity Fluctuations and Internal Intermittency in Marine Stratocumulus Clouds." In: *J. Atmos. Sci.* 67, pp. 262–273. DOI: 10.1175/2009JAS3200.1 (cit. on pp. 4, 22).

Siebert H, Lehmann K, Wendisch M (2006a). "Observations of Small-Scale Turbulence and Energy Dissipation Rates in the Cloudy Boundary Layer." In: *J. Atmos. Sci.* 63, pp. 1451–1466. DOI: 10.1175/JAS3687.1 (cit. on p. 22).

Siebert H et al. (2006b). "Probing Finescale Dynamics and Microphysics of Clouds with Helicopter-Borne Measurements." In: *Bull. Amer. Meteor. Soc.* 87, pp. 1727–1738. DOI: 10.1175/BAMS-87-12-1727 (cit. on p. 21).

Siebesma AP et al. (2009). "Cloud-controlling Factors." In: *Clouds In The Perturbed Climate System. Their Relationship to Energy Balance, Atmospheric Dynamics, and Precipitation*. Ed. by J Heintzenberg, RJ Charlson. MIT Press, pp. 269–290 (cit. on p. 19).

Simonin O, Zaichik LI, Alipchenkov VM, Fevrier P (2006). "Connection between two statistical approaches for the modelling of particle velocity and concentration distributions in turbulent flow: The mesoscopic Eulerian formalism and the two-point probability density function method." In: *Phys. Fluids* 18, p. 125107. DOI: 10.1063/1.2404947 (cit. on pp. 28, 30).

Smith SA, Jonas PR (1995). "Observations of the turbulent fluxes in fields of cumulus clouds." In: *Q. J. R. Meteorol. Soc.* 121, pp. 1185–1208. DOI: 10.1002/qj.49712152602 (cit. on p. 21).

Springel V (2005). "The cosmological simulation code gadget-2." In: *Mon. Not. R. Astron. Soc.* 364, pp. 1105–1134. DOI: 10.1111/j.1365-2966.2005.09655.x (cit. on p. 4).

Springel V et al. (2005). "Simulations of the formation, evolution and clustering of galaxies and quasars." In: *Nature* 435, pp. 629–636. DOI: 10.1038/nature03597 (cit. on p. 4).

Sreenivasan KR (1995). "On the universality of the Kolmogorov constant." In: *Phys. Fluids* 7, pp. 2778–2784. DOI: 10.1063/1.868656 (cit. on pp. 15, 44).

Stokes GG (1843). "On some cases of Fluid Motion." In: *Trans. Cambridge Phil. Soc.* 8, p. 105 (cit. on p. 7). Repr. in *Mathematical and Physical Papers by George Gabriel Stokes*. Vol. I. Cambridge Univ. Press, 1880.

——(1851). "On the Effect of the Internal Friction of Fluids on the Motion of Pendulums." In: *Trans. Cambridge Phil. Soc.* 9, pp. 8–106 (cit. on p. 16). Repr. in *Mathematical and Physical Papers by George Gabriel Stokes*. Vol. III. Cambridge Univ. Press, 1901.

Stumm W, Morgan J (1996). *Aquatic Chemistry: Chemical Equilibria and Rates in Natural Waters*. 3rd. Environmental science and technology. Wiley, p. 1040 (cit. on p. 5).

Sundaram S, Collins LR (1996). "Numerical Considerations in Simulating a Turbulent Suspension of Finite-Volume Particles." In: *J. Comput. Phys.* 124, pp. 337–350. DOI: 10.1006/jcph.1996.0064 (cit. on p. 35).

——(1997). "Collision statistics in an isotropic particle-laden turbulent suspension. Part 1. Direct numerical simulations." In: *J. Fluid Mech.* 335, pp. 75–109. DOI: 10.1017/S0022112096004454 (cit. on pp. xix, 21, 26, 27, 46, 65, 76).

Swope WC, Andersen HC, Berens PH, Wilson KR (1982). "A computer simulation method for the calculation of equilibrium constants for the formation of physical clusters of molecules: Application to small water clusters." In: *J. Chem. Phys.* 76, pp. 637–649. DOI: 10.1063/1.442716 (cit. on p. 44).

Taylor GI (1935). "Statistical Theory of Turbulence." In: *Proc. R. Soc. London Ser. A* 151, pp. 421–444. URL: http://www.jstor.org/stable/96557 (cit. on pp. 10, 11, 24).

Tennekes H, Lumley JL (1972). *A First Course in Turbulence*. The MIT Press, Mar. 1972 (cit. on pp. 9, 13).

Thomson W, 1st Baron Kelvin (1887). "XLV. On the propagation of laminar motion through a turbulently moving inviscid liquid." In: *Phil. Mag.* 24, pp. 342–353. DOI: 10.1080/14786448708628110 (cit. on p. 10).

Tikhomirov V, ed. (1991). *Selected Works of A. N. Kolmogorov. Volume I: Mathematics and Mechanics*. Kluwer Academic Publishers. DOI: 10.1007/978-94-011-3030-1 (cit. on p. 14).

Toschi F, Bodenschatz E (2009). "Lagrangian Properties of Particles in Turbulence." In: *Annu. Rev. Fluid Mech.* 41, pp. 375–404. DOI: 10.1146/annurev.fluid.010908.165210 (cit. on p. 17).

Vaillancourt PA, Yau MK (2000). "Review of Particle–Turbulence Interactions and Consequences for Cloud Physics." In: *Bull. Amer. Meteor. Soc.* 81, pp. 285–298. DOI: 10.1175/1520-0477(2000)081<0285:ROPIAC>2.3.CO;2 (cit. on p. 19).

Völk HJ, Jones FC, Morfill GE, Röser S (1980). "Collisions between grains in a turbulent gas." In: *Astron. Astrophys.* 85, pp. 316–325. URL: http://adsabs.harvard.edu/abs/1980A&A....85..316V (cit. on p. 66).

von Neumann J (1961). "Recent theories of turbulence." In: *J. von Neumann. Collected works*. Ed. by AH Taub. Vol. VI. 32. Report originally written in 1949 for the Office of Naval Research. Oxford: Pergamon Press, pp. 437–472 (cit. on p. 4).

von Weizsäcker CF (1948). "Das Spektrum der Turbulenz bei großen Reynoldsschen Zahlen." In: *Z. Phys.* 124, pp. 614–627. DOI: 10.1007/BF01668898 (cit. on p. 15).

Voßkuhle M (2009). "Statistische Analysen zweidimensionaler Turbulenz." Diplomarbeit. Westfälische Wilhelms-Universität, Aug. 2009 (cit. on p. 7).

Wang L-P, Ayala O, Grabowski WW (2005a). "Improved Formulations of the Superposition Method." In: *J. Atmos. Sci.* 62, pp. 1255–1266. DOI: 10.1175/JAS3397.1 (cit. on p. 64).

Wang L-P, Ayala O, Kasprzak SE, Grabowski WW (2005b). "Theoretical Formulation of Collision Rate and Collision Efficiency of Hydrodynamically Interacting Cloud Droplets in Turbulent Atmosphere." In: *J. Atmos. Sci.* 62, pp. 2433–2450. DOI: 10.1175/JAS3492.1 (cit. on p. 31).

Wang L-P, Wexler AS, Zhou Y (1998a). "On the collision rate of small particles in isotropic turbulence. I. Zero-inertia case." In: *Phys. Fluids* 10, pp. 266–276. DOI: 10.1063/1.869565 (cit. on pp. 50, 59, 84).

——(1998b). "Statistical mechanical descriptions of turbulent coagulation." In: *Phys. Fluids* 10, pp. 2647–2651. DOI: 10.1063/1.869777 (cit. on pp. 31, 32).

——(2000). "Statistical mechanical description and modelling of turbulent collision of inertial particles." In: *J. Fluid Mech.* 415, pp. 117–153. DOI: 10.1017/S0022112000008661 (cit. on pp. 21, 32).

Wells ML, Goldberg ED (1991). "Occurrence of small colloids in sea water." In: *Nature* 353, pp. 342–344. DOI: 10.1038/353342a0 (cit. on p. 5).

Wilkinson M, Mehlig B (2003). "Path coalescence transition and its applications." In: *Phys. Rev. E* 68, p. 040101. DOI: 10.1103/PhysRevE.68.040101 (cit. on p. 29).

——(2005). "Caustics in turbulent aerosols." In: *EPL* 71, p. 186. DOI: 10.1209/epl/i2004-10532-7 (cit. on pp. 29, 65).

Wilkinson M, Mehlig B, Östlund S, Duncan KP (2007). "Unmixing in random flows." In: *Phys. Fluids* 19, p. 113303. DOI: 10.1063/1.2766740 (cit. on p. 26).

Wilkinson M, Mehlig B, Uski V (2008). "Stokes Trapping and Planet Formation." In: *Astrophys. J. Suppl.* 176, p. 484. DOI: 10.1086/533533 (cit. on p. 22).

Wilkinson M, Mehlig B, Bezuglyy V (2006). "Caustic Activation of Rain Showers." In: *Phys. Rev. Lett.* 97, p. 048501. DOI: 10.1103/PhysRevLett.97.048501 (cit. on pp. 28, 29, 50, 65, 71).

Williams JJE, Crane RI (1983). "Particle collision rate in turbulent flow." In: *Int. J. Multiphase Flow* 9, pp. 421–435. DOI: 10.1016/0301-9322(83)90098-8 (cit. on p. 21).

Woittiez EJP, Jonker HJJ, Portela LM (2009). "On the Combined Effects of Turbulence and Gravity on Droplet Collisions in Clouds: A Numerical Study." In: *J. Atmos. Sci.* 66, pp. 1926–1943. DOI: 10.1175/2005JAS2669.1 (cit. on pp. 21, 47, 48, 72).

Zhou Y, Wexler AS, Wang L-P (1998). "On the collision rate of small particles in isotropic turbulence. II. Finite inertia case." In: *Phys. Fluids* 10, pp. 1206–1216. DOI: 10.1063/1.869644 (cit. on pp. 30, 59).

> *The dizzying thought that the sea obeyed no rules at all returned. He dismissed it from his mind quickly. He wanted to understand. He had to solve the mystery of the sea to be able to like it[…]*
>
> — Tove Jansson *Moominpappa at Sea*